Sources and techniques for attosecond science

Habilitation Thesis

Author(s):
Gallmann, Lukas (iD)

Publication date:
2011

SOURCES AND TECHNIQUES FOR ATTOSECOND SCIENCE

Habilitationsschrift

von

LUKAS GALLMANN

Institute of Quantum Electronics

Ultrafast Laser Physics

Physics Department

ETH Zurich

2011

Table of Contents

Chapter 1

Introduction

The new frontier in ultrafast time-resolved studies is in the attosecond domain. The orbital period of the electron on the ground state of Bohr's hydrogen atom is ~150 as (1 as = 10^{-18} s). This simple example already illustrates that attoseconds represent the natural time scale of fast electron dynamics in atoms and molecules. Attosecond time resolution allows one to follow electron rearrangement dynamics in atoms or molecules, e.g. after ionization [1], during reactions or dissociation events [2], to resolve electron cloud oscillations of plasmon resonances of metal nano-particles, photo-emission from solid surfaces [3], or migration of electrons from a substrate to an adsorbate [4], to name just a few examples in various disciplines. How do molecular orbitals evolve to their new configuration after an electron has been removed from the molecule? How does the intra-molecular energy transport in early phases of such important processes as photo-synthesis or vision work?

The field of attosecond science is one with exciting prospects but is still in its infancy. The tools to address some of the above questions have only recently become available and still undergo rapid development. Only relatively few measurements with attosecond time resolution have been demonstrated so far. In the following we give a non-exhaustive overview of some typical experiments: A prototype measurement was the detection of the electric field of a few-cycle pulse with the so-called attosecond streak-camera providing ~200 as temporal resolution [5]. Resolving the dynamics of various ionization processes has drawn particular attention. One of the first experiments was the time-resolved measurement of Auger decay in Kr [6]. More recently infrared induced tunnel ionization of highly excited Ne^+ atoms has been time-resolved with a

resolution of a few hundred attoseconds [7]. Two experiments measuring the timing between the photo-electrons emitted in single-photon ionization from the *2s* and *2p* orbitals in neon yielded contradictory results and show how important subtle effects become on such short time-constants [8, 9]. In a first experiment on a solid-state sample, the time-resolved photoemission from a tungsten surface was studied [3]. Without actually using attosecond pulses, angularly resolved momentum distributions of the fragments of helium field-ionized by circularly polarized few-cycle pulses yielded similar timing accuracy [10]. This data was used to determine an upper bound on the tunneling time of the electron leaving the helium ion with a few 10 as accuracy [11]. Trains of attosecond pulses were used to perform electron wavepacket interferometry and thereby to probe phase information in single-photon ionization of argon [12]. Beyond pure ionization processes, the periodicity of attosecond pulse trains was used to obtain stroboscopic pictures of strong-field driven electron rescattering events [13]. Attosecond resolution of proton motion in molecules has been demonstrated without directly using attosecond pulses in the so-called PACER technique [14]. Using PACER, proton motion in H_2^+ in the few femtoseconds following ionization was tracked with $\approx$100 as resolution.

When looking at the above experiments, one can extract a number of commonalities that characterize the state of attosecond science and the underlying technology. Most experiments are being performed on relatively simple model systems – often rare gases. All of them involve strong laser fields. As a result, the system under investigation is always under the influence of non-perturbative fields. Sometimes this might be desired, sometimes not. Almost all experiments detect charged particles and thus intrinsically require ionization to occur in one form or another. Furthermore, count rates per shot are limited when detecting charged particles in order to prevent space charge effects. This immediately brings up another technological aspect: All of the above experiments use Ti:sapphire amplifiers as the primary laser source. Ti:sapphire systems are limited in repetition rate due to thermal effects. Low repetition rates affect measurement duration and achievable signal-to-noise. Furthermore, they're bulky, inefficient, and expensive.

Overcoming some of the technical limitations and introducing new, more general measurement schemes will ultimately allow the field to move to more complex molecular and solid-state systems. Here, we will present our recent contributions to sources and techniques for attosecond science. This includes the development of a novel pri-

mary laser source for high-field science, the investigation of quantum-path interference in high-order harmonic generation – a basic strong-field phenomenon and the process underlying all current attosecond pulse sources –, and the application of a new all-optical attosecond spectroscopy technique to the detection of electron wavepacket interferences in helium strongly driven by an external laser field.

Femtosecond laser pulses are a success story for applications in many fields of research and engineering. While femtosecond lasers start to make it into industrial or medical applications, such short pulses are still far easier to generate in certain spectral regions than in others, even more so, if high power levels or high intensities are required. One particularly difficult region for the generation of intense femtosecond pulses is the mid-infrared, mainly due to the non-existence of sufficiently broadband gain media and the small selection of suitable optical materials in general. The most successful femtosecond mid-infrared sources so far were all based on optical parametric amplification (OPA). We introduce a new system concept for compact and affordable generation of intense, few-cycle mid-infrared pulses at record-high average powers in Chapter 2. The system uses proven, industrial 1-µm laser technology as the pump and a fiber laser operating at the 1.5 µm telecom wavelength as the seed generator or seed directly. To enable efficient and broadband operation with this particular combination of wavelengths, a new technology for the amplification medium needed to be developed in collaboration with the group of Prof. M. M. Fejer from Stanford University [15-19].

High-order harmonic generation is a prototype strong-field process discovered 25 years ago [20, 21]. It underlies all presently demonstrated schemes for attosecond pulse generation. It's also a key process for measurement schemes that do not aim at high time-resolution (see, e.g., [22]) or it just serves as a table-top source of XUV radiation [23]. High-order harmonic generation can be described as a simple three-step process, in which an atom is field-ionized by a strong laser pulse [24]. The created electron is subsequently accelerated in the oscillating external laser field and – if released at the right instant – may ultimately recombine with its parent ion. Upon recombination it emits its excess kinetic energy as an XUV photon. Even when describing the resulting electron trajectories purely classically, one finds that within each laser cycle, two (or more if one looks beyond a single cycle) trajectories can result in the same emitted photon energy. This finding can also be confirmed in a more rigorous quantum mechanical treatment [25]. As the trajectories originate from the same ground state, end in the same

final state, and are driven in a coherent process, one expects quantum interference to occur. In Chapter 3, we present evidence for the first experimental observation of these interferences. The discussion in Chapter 3 also shows that high-order harmonic generation remains to be a playground for more experimental and theoretical work as it is far from understood in all its subtle aspects.

As a prerequisite for attosecond spectroscopy one needs an experimental setup providing sufficient mechanical stability. For a time-resolution on the order of 100 as a mechanical stability of tens of nanometers between the arms of a pump-probe setup is required. In Chapter 4, we briefly describe the apparatus that was developed for this purpose in our laboratory.

As outlined above, attosecond time-resolved experiments traditionally record photo-electron or photo-ion spectra or momentum distributions. Most of the experiments use the streaking of electrons by a strong infrared laser field and the energy-resolved detection of these particles as the fundamental measurement principle. We also listed some of the associated shortcomings. In Chapter 5, we introduce a very recent all-optical measurement method called attosecond transient absorption [26-28] and apply it to the detection of transiently bound electron wavepackets in helium strongly driven by an external laser field. In this experiment, we were able to observe the fastest dynamics detected by all-optical means thus far and reported the first optical detection of attosecond wavepacket interferences.

We present an overall conclusion and outlook in Chapter 6, readdressing some of the issues raised in this Introduction.

Chapter 2

Mid-infrared optical parametric chirped-pulse amplifier

Femtosecond laser pulses have proven to be a very powerful tool across many disciplines. Fields of application range from physics over physical chemistry to biological imaging, material processing, metrology, and medical applications, to name just the most prominent examples. Two Nobel prizes have been awarded to work directly linked to femtosecond laser sources [29-31]. While femtosecond sources cover a large parameter space of pulse duration, energy, and repetition rate in the near-infrared spectral region, femtosecond technology is found to be more difficult to extend to other spectral regions. This is particularly true for the important mid-infrared wavelength range, where no sufficiently broadband laser gain media exist. Nonlinear optical frequency converters typically driven by near-infrared lasers fill the gap left open by the traditional laser media based on population inversion.

Our own interest in developing an intense source of few-cycle pulses in the mid-infrared lies in the wavelength scaling of high-field processes. For example, in high harmonic generation (HHG) the cut-off energy is proportional to the wavelength squared [32]. As a result, if the intensity of a typical near-infrared source can be maintained in the mid-infrared, it should be possible to extend harmonic photon energies - and thereby attosecond pulses - into the multi-hundred electronvolt to keV range. This photon energy regime is of tremendous interest for x-ray absorption spectroscopy on metal-organic complexes. Even if photon energies are only scaled to a couple of 100 eV, one gains access to the so-called water window, which is of high experimental

significance because in this range (284 eV to 543 eV) absorption by carbon atoms is stronger than that from water – a prerequisite for the investigation of biologically relevant systems. More of these applications are discussed at the end of this Chapter.

Nonlinear frequency conversion processes used for the generation of femtosecond mid-infrared pulses typically are difference frequency generation (DFG) or optical parametric amplification (OPA) – both closely related to each other. The nonlinear converters are most commonly pumped by Ti:sapphire based femtosecond near-infrared laser systems [33-47]. For higher pulse energies, these Ti:sapphire systems are often chirped pulse amplifiers (CPA, [48]) running at relatively modest repetition rates on the order of a kHz or even below. This is the case for the commercial TOPAS system by Light Conversion Ltd. or the more recent results in the wavelength range around 2.1 µm [49, 50] or 3–4 µm [51]. The repetition rates of such systems are limited by thermal load in the Ti:sapphire gain medium. Since Ti:sapphire itself is pumped again by frequency-doubled near-infrared lasers, the overall complexity of such systems is usually high and the overall efficiency low.

Recent developments in the field of diode-pumped solid state and fiber lasers make it possible to advance to applications previously limited to conventional chirped pulse amplification systems, while benefiting from compactness, efficiency, and reliability of this new laser technology. This recent progress also enabled the demonstration of high-repetition rate OPA sources in the visible to near infrared based directly on diode-pumped laser technology [52-54]. A major benefit of parametric amplifiers is the relatively low thermal load in the gain material. This benefit can be exploited with high repetition rate pump sources for relatively easy scaling of average power and repetition rate.

While mid-infrared pulses have been generated in the idler wave of the system reported by Marangoni et al. [54], their main interest was on the near-infrared output and the idler was therefore not further characterized. An early result by Laenen et al. [55] used 0.523 and 1.047 µm pump wavelengths for the generation of femtosecond pulses in the 2.6 to 7 µm wavelength interval, but their pump laser was flashlamp pumped and thus limited to a repetition rate of 50 Hz.

In the context of this work, we demonstrated the first femtosecond optical parametric chirped-pulse amplifier (OPCPA, [56]) operating in the mid-infared [57, 58]

and being pumped by diode-pumped solid-state lasers directly. A similar system operating at slightly shorter wavelengths was developed and demonstrated by Chalus et al. [59]. Our OPCPA is based on a 1064 nm, 10 ps, 100 kHz laser amplifier system as a pump. First incarnations of the system used a 3–4 µm seed source. In this case, the mid-infrared output is obtained through difference frequency generation (DFG) from a 1.5 µm femtosecond Er:fiber amplifier [60, 61]. The choice of pump and seed generation laser is driven by the fact that both are available as commercial products. These compact and diode-pumped lasers are reliable and enable turn-key operation. As we will point out in more detail below, we later developed a booster amplifier for our pump laser and moved to a new seed concept that uses the 1.5 µm fiber laser pulses as a direct input to the OPCPA. The main goal of all this work is to develop a source of intense, carrier-envelope offset phase (CEP) stable few-cycle mid-infrared pulses providing sufficiently high peak intensity to be suitable for studying strong-field interactions in atomic and molecular physics (i.e., $I_{\text{peak}} \approx 10^{14}\,\text{W}/\text{cm}^2$).

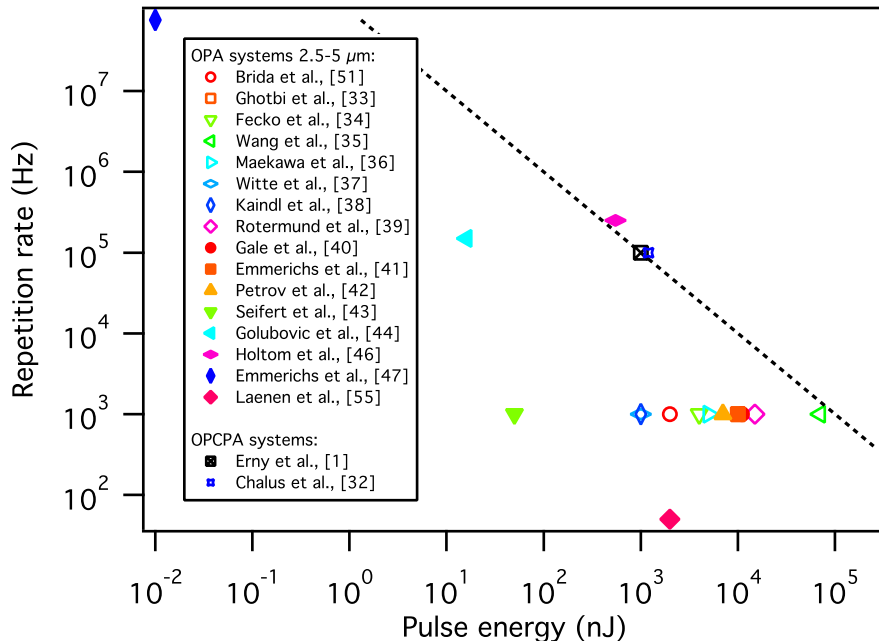
Figure 2.1: Repetition rate and pulse energy of previously demonstrated sources of femtosecond pulses in the 2.5-5 µm wavelength range. The dashed diagonal line marks points corresponding to an average power of 100 mW. The graph clearly shows that many sources are limited to the ~1 kHz repetition rate of their Ti:sapphire pump lasers.

Figure 2.1 gives an overview of previous demonstrations of femtosecond pulses in the wavelength range from 2.5 to 5 µm and also shows the recent results with our mid-infrared OPCPA. This graph clearly demonstrates that the average output power of our system compares very well with the Ti:sapphire based approaches. The higher repetition rate of our system is highly beneficial for many applications. More shots in a given time interval translate to better measurement statistics and signal-to-noise ratio. In experiments detecting charged particles, pulse energies have to be limited to avoid space charge effects. Some experiments thus only become realistically feasible with a laser source providing a sufficiently high pulse repetition rate.

This chapter is structured as follows: In Section 2.1 we discuss a slab amplifier that we developed to boost the output power of our commercial pump laser. This pump laser scaling was a prerequisite for achieving an average output power in the mid-infrared of more than 1 W. The first incarnation of our OPCPA system used commercial periodically poled lithium niobate (PPLN) crystals as the amplification medium and was seeded by an intrinsically CEP stable seed source. Section 2.2 is devoted to the design and modeling of this system. The theoretical considerations motivate certain design choices and show up the limitations of the approach. Results obtained with this OPCPA design are described in Section 2.3. The bandwidth limitation of conventional PPLN amplifier crystals lead us to develop new aperiodically poled lithium niobate (APPLN) structures in collaboration with the group of Prof. M. M. Fejer from Stanford University. The first demonstration of such aperiodical quasi-phase matching structures for OPCPA is reported in Section 2.4. All this work showed some limiting aspects in our initial system concept. These can be overcome by modifying the seed concept. The new concept and initial results are discussed in Section 2.5. Finally, we give an outlook towards future directions and applications with this source in Section 2.6.

Results presented in this Chapter have been reported in scientific journal publications [18, 57, 58, 62].

2.1   Pump laser scaling

2.1.1   Introduction

Modern ultra-broadband optical parametric chirped-pulse amplifiers (OPCPA) [18, 57, 63-67] need reliable picosecond lasers as pump sources with high peak power and at least hundreds of microjoules of pulse energy. Such systems are used to reach ultrahigh peak-powers or to explore high-field phenomena in previously uncovered wavelength regimes [68]. The latter is the main motivation behind our mid-infrared OPCPA work.

A pump pulse duration of on the order of 10 ps turns out to be ideal for our class of OPCPA [69]. The reason for this is the required stretching of the seed pulses that is needed to limit the peak power of the amplified pulses in the gain medium while achieving a significant temporal overlap between seed and pump for efficient energy transfer. Low stretching factors below a few picoseconds would cause unacceptably high peak powers in the gain medium or severely limit the maximum achievable output fluence. On the other hand, stretching few-cycle pulses beyond several picoseconds renders recompression challenging.

To date not many diode-pumped solid-state laser systems have been reported that deliver picosecond pulses with peak powers in the MW-regime. Most of them are limited to repetition rates below 10 kHz [70-73]. For example Yb:YAG thin-disk amplifiers produced pulse energies up to 4.5 mJ at a pulse duration of 4.5 ps. Our system as described here reduces the complexity compared to these implementations. We focus on stability and ease of operation while obtaining as much pulse energy as possible.

2.1.2   Booster amplifier

We adopt the InnoSlab concept [74, 75] for amplifying energetic picosecond pulses at 50-100 kHz repetition rate from a picosecond seed laser. This concept has been proven for the amplification of low peak-power lasers without deteriorating beam quality and noise performance [74]. Up to now slab amplifiers have only been used for picosecond pulses in a side pumped geometry yielding <20 MW peak power [71, 72]. Successful power scaling of a 615-fs system at 20 MHz repetition rate has recently been demonstrated with two Yb:YAG slabs in a 7+1 pass configuration yielding kW-level average output power [76].

Here, we report on a picosecond Nd:YVO$_4$ InnoSlab amplifier with a record high pulse energy of 600 µJ and 12-ps pulse duration. It exhibits excellent noise performance with pulse fluctuations below 0.8% rms over a measurement interval of 30 min.

Our amplifier is built in a 4-pass configuration based on a 0.4% doped Nd:YVO$_4$ crystal with a dimension of 1x10x10 mm^3. The InnoSlab concept consists of a thin crystal that can be conduction-cooled homogeneously and efficiently through the large sides of the slab. This results in a one-dimensional heat flow transversely to the laser beam propagation. The resulting thermal lens is cylindrical with low aberrations and avoids depolarization losses. A hybrid resonator-like multi-pass configuration with one stable and one unstable axis enables high-energy pulses with excellent beam quality [74].

Our seed source is the industrial laser "Duetto" from Time-Bandwidth Products Inc., delivering 12-ps pulses at repetition rates of 30 kHz to 8 MHz and an average output power of up to 12 W. Highest pulse energies are achieved at low repetition rates, therefore we operate the laser at 50 and 100 kHz. Only 1 W of the laser output power is used to seed the slab amplifier while the remaining power pumps the first stage of a mid-IR few-cycle OPCPA [18]. Seeding with less power reduces the output energy stability of the slab amplifier. The output of the slab amplifier described here is then used for pumping an additional high-energy stage of this OPCPA.

Other InnoSlab amplifiers use a confocal, cylindrical cavity in the unstable axis to increase the beam diameter within the amplifier and, therefore, to limit the intensity with increasing power [74]. We however implemented a simpler plane-plane mirror configuration (Figure 2.2), using the adapted inherent divergence of the gaussian seed beam for the same purpose [77]. The beam divergence of the seed beam is adapted to generate a fast and a slow diverging beam with a simple and robust telescope, consisting of only one spherical and one cylindrical lens. The plane mirrors have to be tilted with respect to each other to avoid parasitic oscillations within the multi-pass resonator. These tilt angles together with the slow-axis beam divergence are designed to obtain a large fill-factor inside the gain crystal, a small overlap of the individual beams and low diffraction losses at the gain crystal edges. The seed beam is adjusted such that the divergence is set to about 9.7 mrad in the fast (stable) axis and 5.5 mrad in the slow (unstable) axis, resulting in a beam diameter of 600 µm and 300 µm, respectively, at the

entrance of our hybrid resonator. In the fast axis, the gaussian shaped gain profile of the slab fits to the resonator's TEM_{00} mode and the cylindrical thermal lens reproduces the mode at the cavity mirrors. The thermal lens changes with pump power, it is therefore favorable to operate the amplifier at a fixed working point. We optimized our setup for an absorbed pump power of 180 W (200 W incident pump power). Due to the larger divergence of the seed, a part of the seed clips at the crystal mount for all other pump powers, resulting in a distorted beam profile.
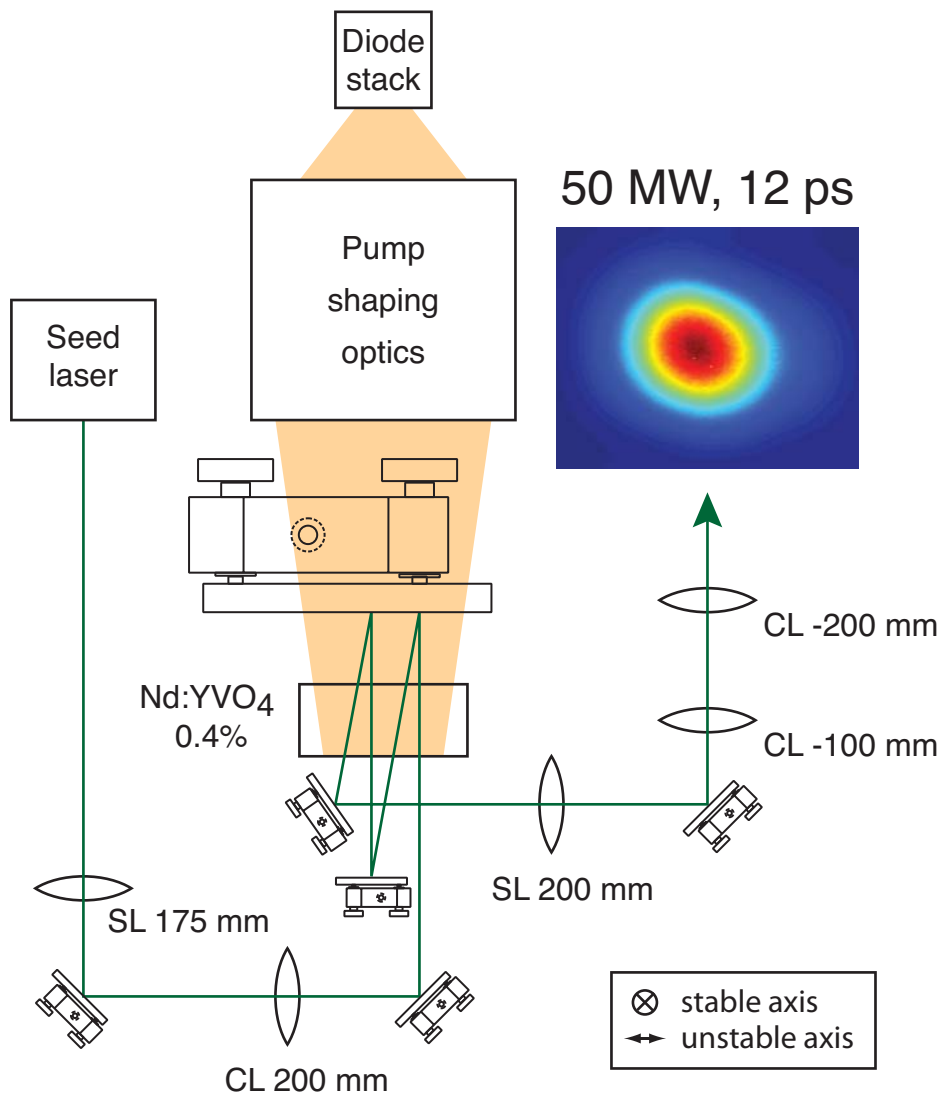
Figure 2.2: Amplifier setup with typical beam profile. A cylindrical lens (CL) and a spheri-cal lens (SL) are used to set the divergence for the hybrid resonator. A telescope of cylin-drical lenses ensures a circular outpur beam profile.
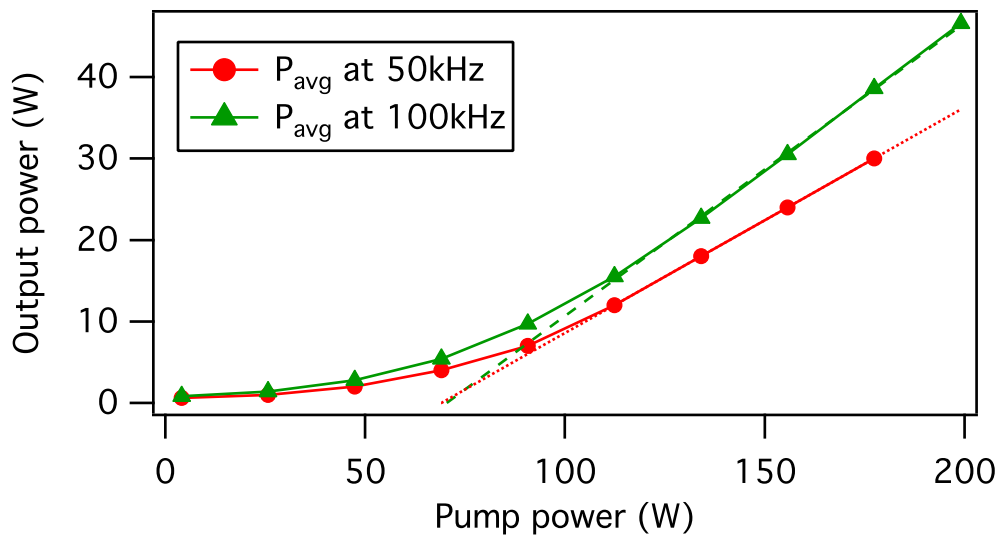
Figure 2.3: Output of the slab amplifier versus pump power. The slope efficiency is 36% at 100 kHz (red circles) and 27% at 50 kHz (green triangles) repetition rate.

The output of the amplifier is transformed back into a round beam profile with a three-lens telescope. We obtained an M^2 of 1.15 in the stable and 1.38 in the unstable direction. A spherical lens is used to set the collimated beam diameter and a cylindrical lens telescope ensures a circular beam shape. A typical reshaped output beam profile at full pump power is shown in Figure 2.2. For all output energies the intensity autocorrelation has been measured, which shows no deviation from the gaussian shaped seed trace.
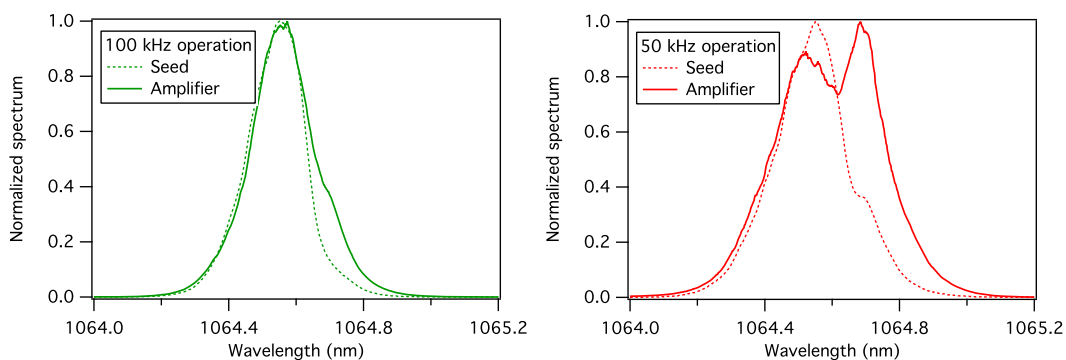
Figure 2.4: Optical spectrum of seed and amplified seed at 50 and 100 kHz, respectively. Only small spectral broadening is observed at 100 kHz, 38 MW (left). Broadening by a factor of two occurs at 50 kHz, 50 MW (right). At 50 kHz repetition rate the pump power is limited to 177 W in order to avoid damage at the Nd:YVO$_4$ crystal.

Our design goal was to generate the largest possible beam diameter for the last pass through the slab amplifier to minimize the optical power density and to maximize the overlap with the pumped gain area. With the relatively short seed pulse duration of 12 ps power scaling is not limited by thermal effects but by the B-integral determined by the peak power of the amplified pulse. To avoid any damage to the vanadate crystal, we limit the output peak-powers to a range where the spectral broadening through self-phase modulation (SPM) does not exceed a factor of two (Figure 2.4). The maximum achievable output energy could be increased by chirped pulse operation, reducing the B-integral, as implemented in [78]. This would, however, come at the expense of a higher complexity of the system, which we wanted to keep low. Simplicity was one of our main design objectives.

We optimized the system for good noise performance. A 1-W seed was used for reducing the gain to below 20 dB, considerably suppressing noise caused by amplified spontaneous emission (ASE). Furthermore, a stable laser-diode driver, isolation from air currents and a small footprint resulted in as little as 0.8% rms pulse energy fluctuations over a measurement interval of 30 min. The rms fluctuations have been quantified with a photodiode (10 ns rise time). We ensure operation of the photodiode in a linear regime ($I < 0.7$ mA) and eliminate sensitivity towards pointing instabilities by recording the stray light of a large area power meter.

The amplifier is used in our lab on a daily basis and realignment was not needed over a period of several months, which further confirms its excellent long-term stability. The system provides a reliable pump for our OPCPA. The peak power of the output pulses is verified with the power scaling of second harmonic generation (SHG) in LBO. A quadratic dependence of the second harmonic with respect to the incident fundamental power validates a vanishing noise background. Our OPCPA experiments represent an independent confirmation of this observation.

2.1.3   Summary

In conclusion, we have demonstrated a high peak and average power slab amplifier at 50-100 kHz pulse repetition rates delivering hundreds of microjoule pulse energy. Our setup maintains the excellent beam profile and low noise of our industry grade seed laser. We chose not to operate the system beyond spectral broadening by a factor of two

compared to the initial seed bandwidth. This is a somewhat arbitrary but conservative choice and limits the maximum peak power in this experiment. The maximum output pulse energy we achieve is 600 µJ (P_{av} = 30 W, P_{peak} = 50 MW) at 50 kHz and 466 µJ (P_{av} = 46 W, P_{peak} = 38 MW) at a repetition rate of 100 kHz (Figure 2.3). The scaling of output power with pump power shows no signs of thermal rollover. This indicates the potential of scaling to higher average powers at higher repetition rates. Our seed source is capable of tuning its repetition rate from 30 kHz to 8 MHz with only minimal output beam parameter changes. Since the target repetition rate for our OPCPA is 100 kHz and below, other regimes were not explored [18]. We observe no indications for being close to the damage threshold when operating the system at its maximum peak power and limiting the SPM-induced spectral broadening.

2.2   Design of a PPLN based OPCPA

Intense femtosecond mid-infrared laser sources in the wavelength range from 3 to 4 µm are of interest for many applications, ranging from traditional ultrafast spectroscopy to high-field laser science. This wavelength range coincides with many important vibrational transitions in molecules [79-81]. In high-field science, mid-infrared laser sources are expected to significantly increase cut-off energies in high-harmonic generation [82].

In this Section, we discuss the design and dimensioning of a femtosecond optical parametric chirped–pulse amplifier (OPCPA, [56]) operating at high-repetition rates in the mid-infrared. Its basic concept was already introduced at the beginning of this Chapter. The OPCPA is based on a 1064 nm, 10 ps commercial pump laser operating at 100 kHz repetition rate. The mid-infrared idler seed is obtained through difference frequency generation (DFG) from a 1.5 µm femtosecond Er:fiber amplifier [60, 61].

No suitable laser gain medium exists for intense femtosecond pulse generation in the mid-infrared. Pulses in this regime are usually generated by nonlinear frequency conversion such as optical parametric generation (OPG) or optical parametric amplification (OPA). Table 2.1 gives an overview of previous demonstrations of femtosecond pulses in the wavelength range from 2.5 to 5 µm. The same data is displayed in Figure 2.1.

Reference	Repetition rate [kHz]	Pulse energy [μJ]	Pulse duration [fs]	Output center wavelength [μm]	Comments
Brida et al., [51]	1	2	~30	3.1-4.7	Pulse duration not measured, transform limit indicated instead
Ghotbi et al., [33]	1	~15	110	3.1	Higher pulse energies below 2.5 μm
Fecko et al., [34]	1	3-4	45	3	Pulse energy before compression
Wang et al., [35]	1	70	~150	2.9-4	
Maekawa et al., [36]	1	0.5-5	55	3-8	Pulse duration measured at 3 μm only
Witte et al., [37]	1	<1	>190	3-10	Maximum energy, shortest pulses at 3 μm
Kaindl et al., [38]	1	<1	50-150	3-20	High energy, short pulses on short wavelength side
Rotermund et al., [39]	1	15	160	3.5	
Gale et al., [40]	1	11-13	200	2.6-3.6	
Emmerichs et al., [41]	1	6-16	150-400	2.8-3.4	
Petrov et al., [42]	1	0.5-7	<200	3-4.4	High energy on long wavelength side
Seifert et al., [43]	1	~0.05	160	3.3-10	Pulse duration measured at 4 μm
Golubovic et al., [44]	100-150	<0.016	<50	2.4-22	Pulse duration estimated from signal-idler crosscorrelation
Gruetzmacher et al., [45]	4	?	<65	2.7-4.7	Pulse energy unknown
Holtom et al., [46]	250	0.55	160	2.5-2.9	Energy and duration for 2.75 μm
Emmerichs et al., [47]	$7.6 \cdot 10^4$	10^{-4}	200-400	2.6-4	
Laenen et al., [55]	0.05	<2	500-2600	2.6-7	Pumped at 0.523 μm and 1.047 μm

Table 2.1: Previous results of femtosecond mid-infared laser sources in the wavelength range from 2.5 to 5 μm.

The high-repetition-rate OPCPA system, which is discussed in this Section, employs a tunable femtosecond mid-infrared source for seed generation [61]. It is based on difference frequency mixing of one output from a two-branch femtosecond Er:fiber amplifier [83] with the spectrally shifted output from the second branch. The spectral shift is generated in a highly nonlinear fiber (HNLF, [60]). The pump source in our experiments and simulations is the Duetto system from Time-Bandwidth-Products, which covers repetition rates in the range from 50 kHz to 8 MHz and pulse energies up to 200 μJ at a central wavelength of 1064 nm. The 10 ps duration of its output pulses fits well to the attainable stretching factors of the seed. With simple and efficient bulk or prism stretchers we can easily stretch the mid-infrared seed to a duration on the order of several ps. For higher repetition rates in the MHz regime, the direct output from modelocked thin-disk oscillators could be used as the pump source. Pulse energies of up to 26 μJ have been reported recently from such lasers [84, 85]. This is sufficient energy to operate the first amplification stage of the OPCPA discussed in this Section.

One of the challenges at mid-infrared wavelengths is posed by the choice of available optical materials for the nonlinear amplification and dispersive stretching of the pulse. Only a few materials are transparent between 3 and 4 μm. Most materials that are successfully used for 800 nm OPCPAs are no longer transparent at wavelengths longer than 2 μm. A prominent example for this is β-barium-borate (BBO). In Subsection 2.2.1, we discuss the selection of nonlinear materials for a mid-infrared OPA to-

gether with their suitability for broadband amplification in this wavelength regime. Materials for quasi phase-matching (QPM) as well as for noncollinear birefringent phase matching are investigated.

We then present the design of a two-stage OPCPA, beginning with the optimization of the pulse duration ratio for pump and seed source. This is essential for a large amplification bandwidth and high conversion efficiency. For the same purpose we have studied the impact of the beam radii and have determined the optimal nonlinear crystal length. We show that for the available seed intensity it is necessary to distribute the amplification into two stages, a pre-amplification and a power-amplification stage, and we analyzed how the available pump power needs to be distributed between these two stages. The numerical results are supported by experimental data.

Numerical simulation makes it possible to look at pulse evolution inside the nonlinear crystal and get a detailed understanding of the optical parametric amplification process. We benefit from this capability when optimizing the crystal length. It turns out that the length of the nonlinear medium has to be chosen carefully. A crystal that is too short leads to spectral narrowing, while in a long medium back conversion from the signal to the pump can take place [86] or background noise from unsuppressed optical parametric generation can be amplified.

Our OPCPA system incorporates two independent modelocked laser oscillators – one seeding the fiber amplifier and one seeding the 1 µm pump laser – that need to be synchronized to each other. In our case, this is done electronically with a phase-locked-loop (PLL) (model CLX-1100 from Time-Bandwidth Products). Due to the instantaneous nature of the optical parametric amplification process, the quality of this lock is crucial for the stability of the OPCPA system. Therefore, we have carefully analyzed the influence of the timing jitter between the two synchronized lasers onto the OPCPA system. These simulation results can be used to determine the tolerable jitter level of the PLL electronics.

In the last part of this Section, possible alternative schemes to increase the conversion efficiency and amplification bandwidth are discussed.

2.2.1   Materials

The nonlinear gain material is one of the key components for each OPA system determining most of its properties. For high conversion efficiency the nonlinear material should ideally have a high damage threshold to apply tight focusing and a high nonlinear coefficient to keep the required crystal length short. A short crystal reduces the impact of the divergence mismatch between the involved beams. The dispersion relations should permit broadband phase-matching and the material should, of course, be transparent at all involved wavelengths. A list of suitable materials together with some of their basic optical properties can be found in Table 2.2.

Material	Transparency range (nm)	Nonlinear coupling constant $\kappa^2 \propto \dfrac{d_{\mathit{eff}}^2}{n_1 n_2 n_3 \lambda_1 \lambda_2 \lambda_3}$ $((pm/V)^2/\mu m^2)$	Phase matching bandwidth for 1 mm crystal at 3.5 µm (nm)	Damage threshold (taken from [87])
Periodically poled materials:				
$LiTaO_3$	250-5500	2.49	292	>40 GW/cm^2 (30 ps @ 1064 nm [49])
$MgO:LiNbO_3$	330-5500	4.70	323	10 GW/cm^2 (6 ps @ 1064 nm)
Bulk materials:				
$MgO:LiNbO_3$	330-5500	0.27	881	10 GW/cm^2 (6 ps @ 1064 nm)
$LiIO_3$	300-6000	0.06	1677	19 GW/cm^2 (6 ps @ 1064 nm)
$KNbO_3$*	400-4500	0.59	1035	100 GW/cm^2 (100 ps @ 1064 nm)
$KNbO_3$**	400-4500	0.19	939	100 GW/cm^2 (100 ps @ 1064 nm)

Table 2.2: Nonlinear media for a 1064 nm-pumped 3.5 µm OPCPA and their optical properties. * Phase-matching in XZ plane, ** Phase-matching in XY plane

The table is divided into two sections. The first section shows two materials that allow for quasi phase-matching (QPM): stoichiometric lithium tantalate ($LiTaO_3$) and magnesium doped lithium niobate ($MgO:LiNbO_3$). Lithium niobate can also be used for birefringent phase-matching together with lithium iodate ($LiIO_3$) and potassium niobate ($KNbO_3$) as listed in the second section of Table 2.2. The lithium based materials are all transparent up to at least 4.8 µm with a gradual onset of absorption above 4 µm [88]. This is sufficient for covering the tuning range of our DFG seed source, which is tunable between 3.2 µm and 4.8 µm [61]. $KNbO_3$ shows a more pronounced reduction in transparency above 4 µm.

A major benefit of quasi phase-matching is the ability of designing the nonlinear medium such that the largest nonlinear coefficient can be exploited for the nonlinear interaction, only reduced by the QPM-specific factor of $\pi/2$. This leads to an effective nonlinear coefficient that is significantly larger than attainable with birefringent phase-matching. The coupling coefficient $\kappa^2 = d_{eff}/n_1 n_2 n_3 \lambda_1 \lambda_2 \lambda_3$ for the three-wave optical parametric mixing process scales accordingly [89].

Table 2.2 also reveals that the coupling coefficient for QPM LiNbO$_3$ is more than an order of magnitude higher than for bulk LiIO$_3$. A LiIO$_3$ crystal would thus have to be more than an order of magnitude longer than the periodically poled LiNbO$_3$ crystal to achieve the same optical gain. However, noncollinear phase matching, typically required for broadband amplification in birefringently phase-matched media, and Poynting vector walk-off limit the interaction length in the OPA crystal. In contrast, the QPM crystals can be operated in a collinear configuration, which results in a relatively high gain in a simple beam geometry and with short crystals.
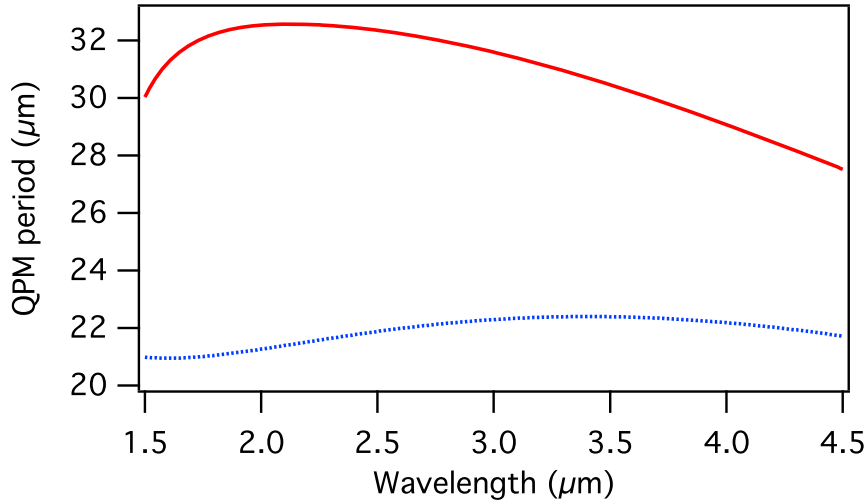
Figure 2.5: Wavelength dispersion of the quasi phase-matching period for congruent periodically poled LiNbO$_3$ with the pump at 1064 nm (solid red line) and 800 nm (dashed blue line), respectively.

For the two QPM materials, the coupling coefficient of LiNbO$_3$ is a factor 2 larger than for LiTaO$_3$, but the damage threshold of lithium tantalate is higher than for lithium niobate because of reduced photorefractive damage caused by green-induced infrared absorption [90, 91]. The gain bandwidth for the two materials is similar but

limited. Larger gain bandwidth could be achieved by pumping the OPA at 800 nm (see Figure 2.5) with a Ti:sapphire pump laser for example. However, this would come with all the drawbacks of Ti:sapphire laser systems such as lower repetition rate and efficiency while being larger in size and higher in cost and complexity. With a pump wavelength of 1 µm, the degeneracy of PPLN, which would allow for broadband amplification, is located at 2 µm [92]. The downside of such a degenerate configuration is that it cannot be operated in a collinear geometry since the signal and idler are at the same wavelength.

The phase matching bandwidth for an OPA is in first order inversely proportional to the group velocity mismatch $GVM = 1/v_{signal} - 1/v_{idler}$. Broadband amplification can therefore be achieved when the group velocity of the signal and idler are identical. This condition can be reached by a noncollinear beam geometry [93]. Under this configuration, an amplification bandwidth of up to 1.6 µm is feasible with $LiIO_3$ at 3.5 µm center wavelength and assuming a 1 mm thick crystal (Table 2.2). This configuration comes, however, with the lowest available nonlinear coupling constant. The second largest amplification bandwidth is obtained with $KNbO_3$ but compared to QPM $LiNbO_3$, the coupling constant is still a factor 8 smaller.

Not only the effective nonlinearity but also the choice of interacting wavelengths plays an important role for a large nonlinear coupling coefficient. This is illustrated by comparing the values calculated for our mid-infrared OPA with those of a visible OPA based on BBO. While the effective nonlinear coefficient of BBO is low compared to most materials presented in Table 2.2, the shorter interacting wavelengths, with the pump at 400 nm, the seed at 630 nm, and the idler at 1100 nm, lead to a coupling constant that is comparable to the one of $MgO:LiNbO_3$ for a 3.5 µm OPA. Therefore both the visible and the mid-infrared OPA show similar optical gain for comparable crystal lengths.

Many other nonlinear materials exist that are commonly used for mid-infrared nonlinear frequency mixing but are not listed in Table 2.2. Examples are mercury-thiogallate ($HgGa_2S_4$), $d_{eff} = 30.6 \, \text{pm/V}$, or silver-thiogallate ($AgGaS_2$), $d_{eff} = 12.3 \, \text{pm/V}$ that both provide a high nonlinear coefficient and have recently become commercially available [87]. But compared to the materials mentioned above, they are either not completely transparent in the respective wavelength range, or more important, they cannot provide broadband phase-matching.

Another promising material is GaAs that shows a high nonlinear coefficient of 95 pm/V [94] in the case of quasi phase-matching. However this material cannot be fabricated in the dimensions required by our OPCPA.

From the above discussion, we find that periodically poled $MgO:LiNbO_3$ is the most promising material for an OPA operated with our pump and seed sources. It allows for a high gain at relatively short crystal lengths. This is necessary to permit tight focusing to achieve the required high intensities.

2.2.2   Numerical model

All simulations in the following have been performed with a nonlinear propagation code written by G. Arisholm [95]. The same code has been used successfully to model an OPCPA laser system operating at 800 nm [64, 96]. The program numerically solves the equations for second-order nonlinear frequency mixing for a full three-dimensional beam in an arbitrary birefringent crystal and takes into account the effects of depletion, diffraction, and walk-off. The software offers two numerical solvers: a Fourier-space method and a split-step method. For our simulations, we used the Fourier-space solver.
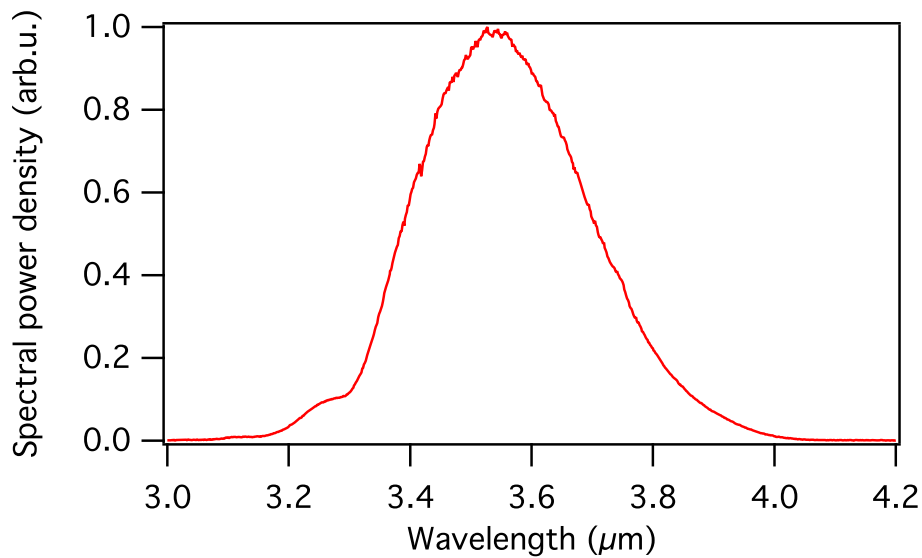

Figure 2.6: Measured seed spectrum from our DFG setup. This spectrum is used as the input for the OPCPA simulations.

Where not stated differently, the following numerical values were used in our simulations. For the first amplification stage model we have assumed a 3.9 µJ, 1064 nm, transform limited Gaussian pulse of 10 ps duration as the pump pulse. The seed energy is 6.5 pJ, which corresponds to 0.5 mW of average mid-IR power at the 82 MHz repetition rate of our seed source. The pump and the seed beams are focused to 49 µm and 42 µm, respectively, corresponding to our experimental conditions. To get an estimate for the temporal input pulse shape we used the measured seed spectrum from our previous DFG experiment [61], centered at 3.6 µm and with a full-width-at-half-maximum (FWHM) bandwidth of 326 nm (). The temporal pulse profile was calculated from this spectrum assuming a constant spectral phase, and resulted in a pulse duration of 55 fs. From earlier simulations of our DFG seed source we know that the DFG output can safely be assumed to be close to transform limit. The two beams were overlapped temporally at the input of the crystal with the focus placed in the center of the crystal. The first amplification stage consists of a 3 mm long PPLN with an effective nonlinear coefficient of $d_{eff} = 20 \text{ pm/V}$. We have treated the nonlinear frequency mixing in the bulk approximation.

2.2.3   Stretcher design

One of the key components of an OPCPA laser system is the stretching of the seed pulse. The most gain can be expected when the pulse duration of the pump pulse and the seed pulse match. We show in this section that the ratio between the seed and the signal pulse has to be selected carefully to optimize the gain bandwidth. The low seed power of <1 mW of our DFG based seed approach [61] together with the general experimental challenge to detect signals in this spectral range make prism or grating sequences difficult to align. We therefore limit our simulation to the case of stretching by bulk material.

There is only a small selection of sufficiently transparent dispersive materials available in the mid-infrared spectral region. The pulse-stretching factor was optimized with simulations for bulk sapphire (Al$_2$O$_3$, polarization along ordinary axis), silicon (Si), or germanium (Ge) with a variable length between 1 mm and 140 mm. While sapphire exhibits a negative group velocity dispersion (GVD) of -966 fs^2/mm at 3.5 µm, the semiconductor materials provide positive GVD of 420 fs^2/mm and 1727 fs^2/mm for Si and Ge, respectively. This corresponds to stretched seed pulse durations of up to 8 ps

for the maximum material length considered. Sapphire and one of the semiconductors could be combined as a bulk stretcher/compressor pair as they have opposite sign in GVD. However, their third-order dispersion (TOD) has the same sign and would therefore remain uncompensated, rendering this approach unsuitable for broadband pulse compression.

In our simulations, the seed and pump beams were temporarily overlapped at the end of the crystal, such that the pump depletion is only taking place in the central, most intense part of the pump pulse. The assumed pump intensity amounts to $7\,\text{GW/cm}^2$, and the seed intensity ranges from $2\,\text{kW/cm}^2$ to $2\,\text{MW/cm}^2$ depending on the stretching factor. The pump intensity is set to our experimentally determined damage threshold for the nonlinear medium.
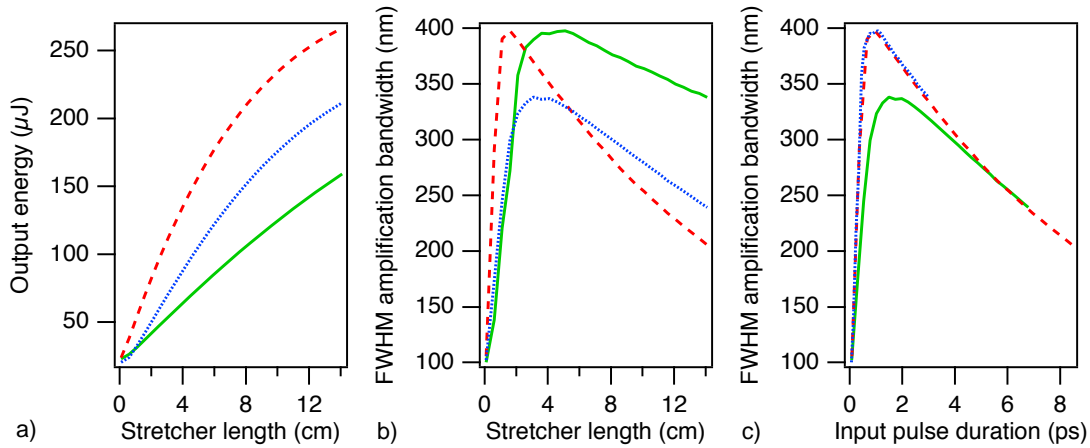
Figure 2.7: Simulations of the first OPCPA stage consisting of a 3 mm PPLN crystal for various amounts of stretcher material (sapphire, blue dotted line; germanium, red dashed line; silicon, solid green line). a) Achievable output power as a function of stretcher material length. b) Full width at half maximum (FWHM) output bandwidth obtained for varying lengths of the three stretcher materials. c) Gain bandwidth versus seed pulse duration.

The amplified output power shows the same qualitative behavior for all three materials (Figure 2.7a). With increasing stretcher material length and seed pulse duration the output energy rises linearly and then starts to saturate. For short input pulses, the rising slopes of the three curves are correlated to the GDD of the applied materials.

The gain bandwidth shows a strong dependency on the ratio between pump and seed pulse duration (Figure 2.7b and c). For short pulses below 0.5 ps and 1.5 ps for the

semiconductors and sapphire, respectively, the OPA shows a strong spectral gain narrowing, which is reduced as the input pulse becomes longer. The bandwidth reaches a maximum of 390 nm for a 1-ps pulse stretched by germanium or silicon. The maximum bandwidth of 338 nm is obtained when stretching the pulse to a duration of 1.5 ps with sapphire. Further stretching leads to more output power but a reduced gain bandwidth. The observed behavior is a result of the interaction between the chirp of the seed pulses and gain saturation.

Our observations can be explained as follows. Three regimes exist for the ratio of the seed and the pump pulse durations. In the first regime, the seed pulse is close to its transform limit and therefore much shorter than the pump pulse. The seed experiences nearly constant pump amplitude over its entire duration such that even if gain saturation is taken into account for a nearly transform limited seed pulse, all spectral components are exposed to the same pump intensity. The gain bandwidth is therefore only limited by the phase-matching bandwidth of the nonlinear crystal. For a 3 mm long PPLN this is approximately 100 nm.

In the second regime, the stretched seed pulse is still considered short compared to the pump pulse, but cannot be treated transform limited anymore. For such a stretched seed pulse, the spectral wings map to its temporal wings. When the OPA is operated with strong pump saturation, the more intense spectral components of the seed can deplete the pump pulse earlier than the weaker components located in the spectral wings. By burning a temporal hole into the pump pulse, the central spectral components effectively reduce the available pump energy. The spectral wings do not temporally overlap with this hole and therefore have their own pump energy reservoir. The unsaturated pump thus further amplifies them. This leads to a reduced spectral narrowing.

In the third regime, the stretched seed pulse becomes comparable to the pump pulse duration. The temporal pump pulse profile now needs to be taken into account. The central part of the seed pulse still overlaps with the same part of the pump pulse as in the previous regime and therefore experiences similar gain. The temporal and thus also spectral wings of the seed pulse now overlap with the lower intensity temporal wings of the pump pulse. As a consequence the wings of the seed become less amplified than the central part. This obviously results in significant gain narrowing.

We aim to generate the shortest possible pulses. Therefore we want to operate the OPCPA with a stretching factor yielding maximum amplification bandwidth corresponding to the second regime discussed above. From the simulation results depicted in Figure 2.7 we can extract the optimum amount of stretcher material. Due to its relatively high group delay dispersion (GDD) per unit material length only 16 mm of germanium is required, which results in a bandwidth of 397 nm and an output pulse energy of 69 nJ. A silicon material length of 51 mm yields the same bandwidth at a pulse energy of 75.8 nJ. Stretching with negative GDD from 36 mm of sapphire leads to a bandwidth of 338 nm and an output energy of 80 nJ. By slightly increasing the amount of sapphire to 51 mm, it is possible to increase the pulse energy to 107 nJ with an acceptable reduction in bandwidth to 329 nm. Significantly more silicon would be required for similar performance: 91 mm of silicon yields 116 nJ with a 370-nm bandwidth.

These results demonstrate that the positive GDD from the semiconductor materials is capable of providing a slightly higher gain bandwidth than the negative GDD from sapphire. The main advantage of sapphire lies in the lower sensitivity of the OPA bandwidth to the stretcher length. Even a sapphire crystal that was chosen too long by 50% does not significantly reduce the gain bandwidth.

Germanium and silicon show nearly the same performance when comparing bandwidth and output power. The main difference between the two is the required stretcher length. The ratio of GDD to TOD is different for the two semiconductor materials, which gives a clear indication that GDD plays a more important role in the OPA process than the TOD. From a practical point of view, silicon has the advantage that it is transparent from the mid-infrared to a wavelength of 1100 nm. It is therefore possible to use the signal output from our collinear DFG seed source located at 1500 nm as an alignment beam for the OPA.

Our optimization leads us to select the 51 mm sapphire as the optimal stretcher. As will be shown below, this choice is confirmed by our experiments.

2.2.4   First amplification stage

In the previous section, we based our simulations on a 3 mm long PPLN crystal and beam radii of 49 µm for the pump and 42 µm for the seed, corresponding to the values

from our experiment. In this section, we discuss the optimization of the nonlinear medium length and the beam radii with the help of our simulation tool. Important for this optimization is the capability of our simulation code to give insight into the evolution of the amplification process along the crystal. Our results show that the previously selected values are close to the optimum.

The most important parameters of the first amplification stage are gain, conversion efficiency, and amplification bandwidth. Gain should be high such that the number of amplification stages can be kept small. The conversion efficiency should be maximized to make best use of the available pump power. A fundamental upper limit to conversion efficiency comes from the mismatch of the seed and pump pulse durations, which is necessary for maximum amplification bandwidth as shown in the previous section.

The simulation of the first OPA stage was done for a range of $1/e^2$ beam radii between 20 µm and 180 µm. We were assuming identical beam sizes for pump and seed. For each individual beam radius we have performed an intensity scan by varying the pump energy until we reach the damage threshold of the OPA crystal. To obtain insight into the evolution of the amplification along the nonlinear medium, the crystal was divided into thin slices with the calculated data recorded for each of these slices. This enables us to determine the optimum crystal length and is ultimately used to decide on the number of amplification stages needed for our OPCPA system.

The results of our simulations are shown in Figure 2.8. Figure 2.8a) shows the OPA mid-infrared output power as a function of pump power for different choices of the beam radii. An increase in pump beam radius needs to be compensated for by an increase in pump power to maintain the same pump intensity. Since our seed source, on the other hand, only provides a fixed output power, seed intensity drops with increasing seed beam radius. This affects the coupling strength between the pump and the seed field. Therefore the maximum possible conversion efficiency reached at the damage threshold of the nonlinear medium decreases with increasing beam radii whereas the achievable output energy rises (Figure 2.8b). For each beam radius the highest energy was always reached at the end of the 3 mm PPLN. The conversion efficiency shows a maximum of 2.7% at a beam radius of 30 µm and drops to 2.4% at 20 µm and to 1.24% at 180 µm. The decrease in coupling strength can be compensated for by increasing pump intensity, which is however limited by the damage threshold, or by choosing a

longer crystal. The output energy at damage threshold amounts to 19 nJ for a 20 µm beam radius when pumped with 700 nJ and rises up to 0.82 µJ for a radius of 180 µm with a corresponding pump energy of 50 µJ. The spectral bandwidth of the amplified pulse shows a maximum of 330 nm between 30 and 60 µm radius and drops significantly towards smaller and larger radii (Figure 2.8c). We therefore can conclude that our femtosecond OPA should be operated with a beam radius between 30 µm and 60 µm for maximum bandwidth and reasonable efficiency. We have selected a radius of 50 µm as a compromise between efficiency and output energy and predict an output energy of 115 nJ, a FWHM bandwidth of 331 nm, and a conversion efficiency of 2.25%. The corresponding spectrum supports 80 fs pulses.
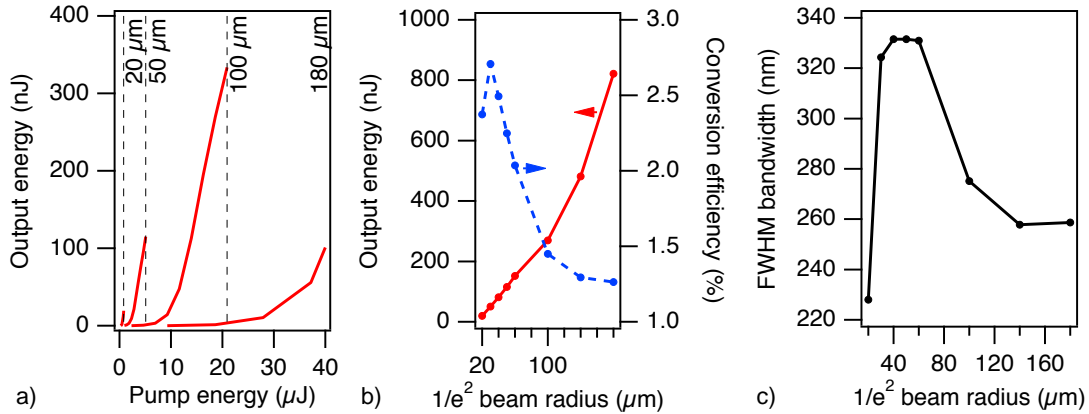
Figure 2.8: Simulation results for the first OPA stage. a) OPA output power versus pump power for different beam radii (20 µm, 50 µm, 100 µm, and 180 µm). The vertical lines mark the damage threshold for the different beam radii with the left-most line corresponding to the smallest radius and the right-most to the 100 µm radius. The damage threshold at 180 µm is at 65 µJ. b) Maximum output energy achievable when reaching the damage threshold (red solid line) and the corresponding conversion efficiency (blue dashed line). c) Full width at half maximum (FWHM) amplification bandwidth as a function of beam radius.

Through the calculation of the nonlinear interaction on a fine grid along the propagation axis, we are able to gain insight into the broadband, short pulse amplification process in a regime of high pump depletion. As expected, the energy of the mid-infrared pulses first increases exponentially, while saturation starts to become significant towards the end of the crystal (Figure 2.9a). The bandwidth of the amplified signal exhibits a strong gain narrowing on propagation through the first half of the crystal. This can already be predicted within the undepleted plain-wave approximation. The

bandwidth reaches a minimum of below 200 nm at 2.1 mm but starts to recover afterwards. An analogous behavior can be observed for the pulse duration of the stretched seed pulse. To understand the dynamics of this process, we have plotted the temporal intensity profiles of the seed and pump pulse at six positions inside the crystal (Figure 2.10). On the first 1.2 mm of the nonlinear interaction, a significant shortening of the seed pulse takes place, while the gain factor amounts to only 41 and no depletion of the pump pulse can be recognized. The depletion of the pump pulse starts to manifest itself after 1.8 mm, where a gain of 785 is reached. This is the position where the pulse duration of the seed as well as its spectral bandwidth reaches the minimum (Figure 2.9b). The slightly modulated pump pulse profile enhances the wings of the mid-infrared pulse compared to its central part. This effect becomes more pronounced the longer the two pulses interact (see Figure 2.10 at 2.4 mm and 3.0 mm). Towards 3.0 mm, a strong temporal broadening can be observed. For the strongly linearly chirped mid-infrared pulse this is equivalent to a strong spectral broadening (Figure 2.9b). Therefore pump depletion can support both a high gain of 17'000 and a broader spectral bandwidth. At the end of the crystal the spectral bandwidth has recovered from its minimum of below 200 nm back to 330 nm. This is 90% of the initial input bandwidth of 360 nm.
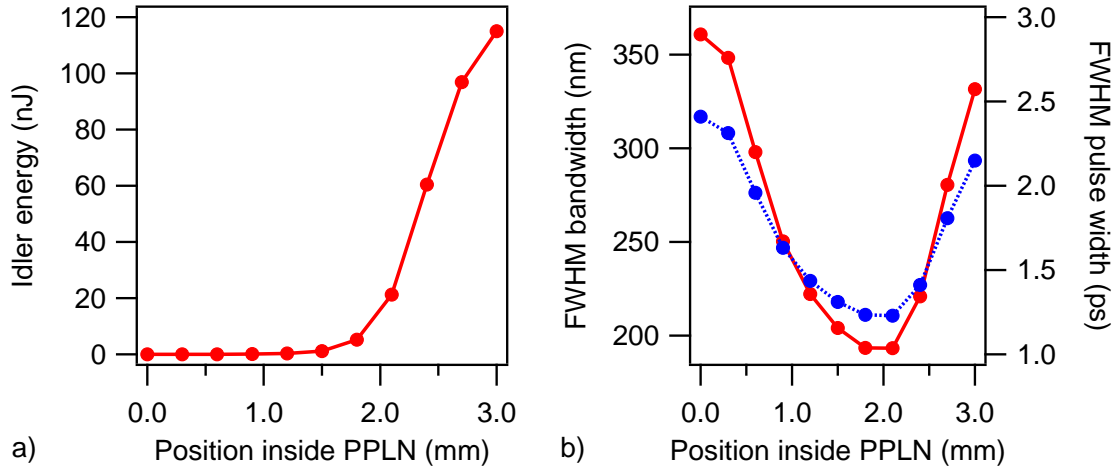
Figure 2.9: Evolution of pulse energy, bandwidth and pulse duration along the 3 mm PPLN crystal of the first OPA stage. a) Energy in the mid-infrared beam at different positions inside the crystal. b) Mid-infrared full width at half maximum (FWHM) bandwidth (solid red line) and pulse duration (dashed blue line) along propagation axis. A minimum is reached around 2 mm and the output values recover to close to the initial values.
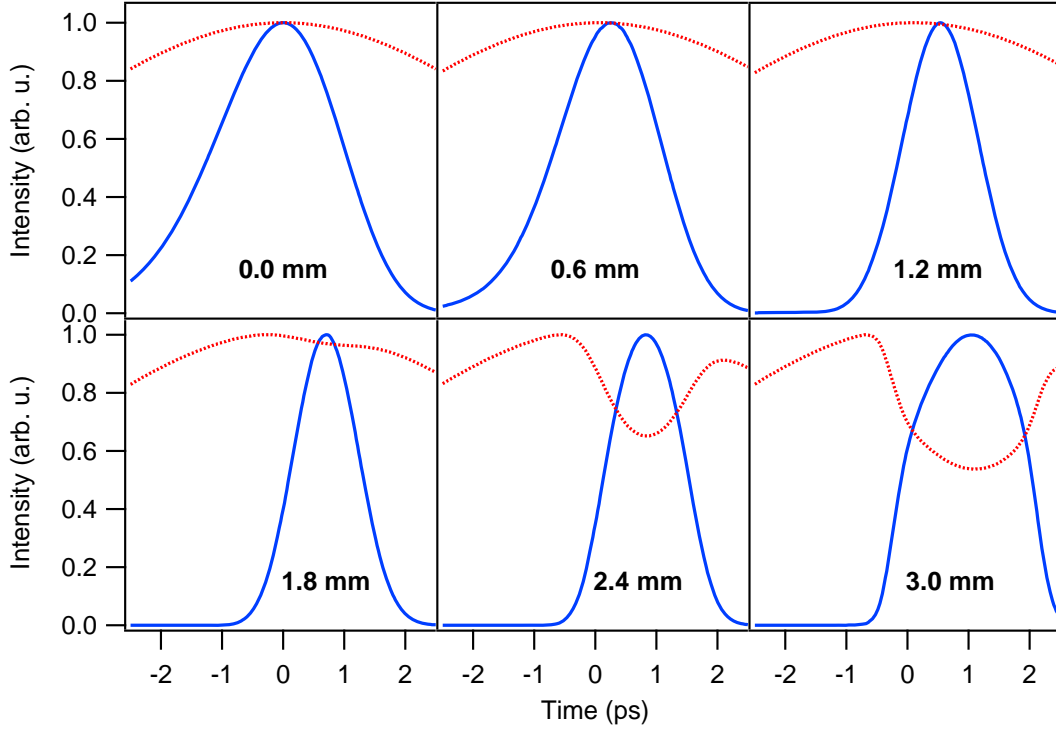
Figure 2.10: Temporal profile of the pump pulse (red dotted line) and the signal pulse (blue solid line) at various positions along the crystal. No saturation effect is visible for a propagation length of up to 1.8 mm. Between 1.8 mm and the end of our 3 mm long crystal, the pump pulse becomes strongly depleted. Pump depletion leads to a temporal and spectral broadening of the seed. The pump energy is 4.3 µJ and the beam radii are 50 µm.

From our simulations we find that a shorter crystal would only reduce the conversion efficiency and lead to a smaller gain bandwidth. An even longer crystal has the benefit of even higher gain, but crystal length is limited by the onset of significant optical parametric generation (OPG). OPG does not require a seed but starts directly from quantum fluctuations. Even though it can be expected that the OPG beam is initially much weaker than the amplified seed, the two processes will compete for gain. The OPG radiation has the competitive advantage compared to the desired seed amplification that it is always perfectly temporally and spatially overlapped with the pump. The amplification of the OPG signal may thus saturate later than the desired seed amplification process. Significant OPG contributions increase the noise level in the output beam. We simulate the OPG process by including quantum noise modeled by numerical white noise into our calculations. The simulated noise starts to build up and destabilizes our

simulations if the nonlinear propagation is extended well beyond the 3 mm crystal length.

Our simulations for the first amplification stage lead us to the following design: a 3 mm long MgO:PPLN with beam radii of around 50 µm for the pump and the seed pulse. The pump pulse energy is set to 3.9 µJ

2.2.5   Second amplification stage

We have demonstrated in the previous section that a single OPA stage is not sufficient to fully benefit from the available 10-W average pump power while maintaining efficient and broadband amplification. Therefore, we have repeated the same types of simulations performed for the first OPA stage in the context of a subsequent second OPA.
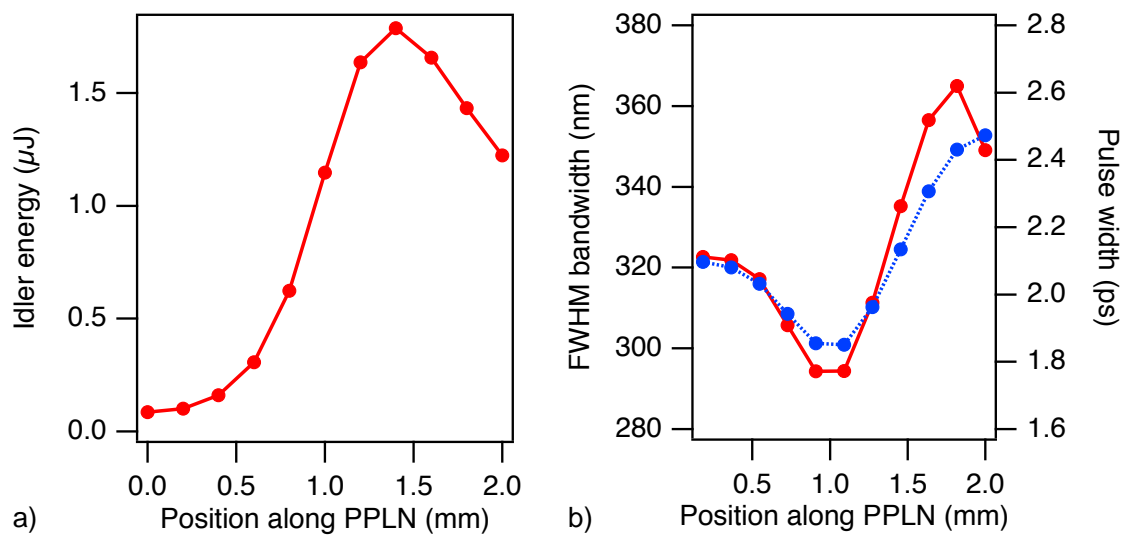
Figure 2.11: Evolution of amplified mid-infrared power, bandwidth and pulse duration along the 2nd OPA crystal. The OPA was pumped at 50 µJ, with a seed pulse energy of 84 nJ and beam radii of 180 µm. a) The amplified energy shows a maximum at 1.4 mm crystal length. Afterwards back conversion from the mid-infrared to the 1.5 µm signal and 1 µm pump starts to become significant. b) Spectral bandwidth (red solid line) and pulse duration along the crystal length (blue dotted line).

The simulated mid-infrared output from the first optimized amplification stage was used as the input for the second amplification stage. Taking into account the Fresnel losses at the uncoated surface of the PPLN, we chose an effective input energy

of 84 nJ in the mid-IR. We first performed simulations at various positions along a 2 mm long PPLN crystal assuming beam radii of 180 µm and a pump energy of 50 µJ, close to the damage threshold of the crystal. With the much higher seed intensity compared to the first OPA, the pump pulse is depleted much earlier inside the crystal (Figure 2.11a). The strong pump depletion may cause some back conversion for which sum-frequency generation is dominating the nonlinear interaction instead of OPA. As a consequence the energy flows back from the signal and the idler wave to the 1-µm pump. This can significantly lower the achievable output power. As can be seen in Figure 2.11a), 1.2 µJ of output energy is generated after 2 mm of PPLN whereas a maximum of 1.79 µJ is reached at 1.4 mm inside the material. The conversion efficiency is nearly 50% higher for the optimized length of PPLN. The spectral bandwidth and pulse duration show the same behavior as was seen with the first OPA (Figure 2.11b). Spectral broadening due to pump depletion follows an initial spectral narrowing. The effect is much less pronounced than in the first OPA stage. Our simulation results clearly show that it is crucial to choose the crystal length sufficiently short to optimize the output power and conversion efficiency.
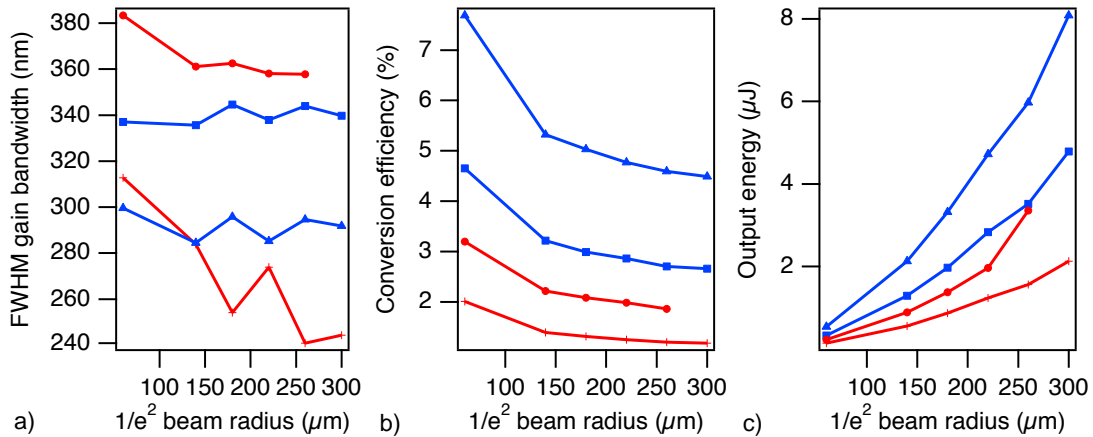
Figure 2.12: Optimization of beam radii and stretching factor for the second OPA stage. The stretcher consisted of 100 mm (triangles) and 50 mm (squares) of Al_2O_3 and 50 mm (circles) and 25 mm (crosses) of Si. a) Gain bandwidth for different pump intensities and stretchers. The highest bandwidth is obtained with 50 mm Si, followed by 50 mm Al_2O_3. b) The highest conversion efficiency P_{out}/P_{Pump} is achieved when stretching the pulses with 100 mm Al_2O_3, followed by 50 mm Al_2O_3. c) Output energy obtained when pumping at the damage threshold.

We ran an additional simulation with the goal of determining the optimum beam radii for the mid-infrared seed and the pump. The simulated radii covered the range from 60 µm to 300 µm. The seed intensity therefore ranges from 10 to 300 MW/cm^2. The pump energy was set to operate close to the damage threshold of the PPLN crystal. Pump energies of up to 100 µJ were used, corresponding to the maximum available energy from our 10-W, 100-kHz Duetto pump laser. To additionally investigate the influence of the stretcher material on the performance of the two-stage OPA we have repeated the same calculations for pulse stretchers made up from 50 mm and 100 mm of Al_2O_3 or 25 mm and 50 mm of Si. The results shown in Figure 2.12 are read out after the OPA crystal length yielding the highest conversion efficiency. The detailed numerical results of our simulations can be found in Table 2.3. The comparison of the four possible pulse stretchers clearly shows that 50 mm of Al_2O_3 provides the best performance for our broadband OPCPA. It results in the highest available gain bandwidth at high conversion efficiency.

Stretcher material	1st OPA output energy (nJ)	1st OPA FWHM gain bandwidth (nm)	2nd OPA output energy (µJ)	2nd OPA FWHM gain bandwidth (nm)
50 mm Al_2O_3	115	332	1.79	335
100 mm Al_2O_3	160	260	3	280
25 mm Si	43	354	0.77	250
50 mm Si	68	360	1.25	357

Table 2.3: Influence of the stretcher material choice on the output performance of the two OPA stages. The first OPA is pumped at 3.9 µJ, whereas second OPA is pumped at 50 µJ.

In contrast to the first OPA stage we did not observe a clear limit for power scaling. In the second OPA stage the seed intensity is sufficiently high to obtain power scaling over a wide range. A practical scaling limit of the second OPA is set by the available crystal sizes. The 180 µm beam radius that we determined to be the optimum for our available pump energy is already large compared to the typical 1 mm clear apertures of commercial PPLNs. Larger clear apertures are, however, becoming commercially available. With larger apertures, bigger beam radii and higher pump energies could be used. Alternatively, one could exchange the PPLN by PPLT, which offers a higher damage threshold (>40 GW/cm^2, for 30 ps pulses at 1064 nm [49]). The higher damage threshold allows increasing the pump energy to 330 µJ at the beam radius of 180 µm. With these parameters, the input beam is amplified to 11 µJ and the generated

pulses possess a bandwidth of 390 nm. This result corresponds to a conversion efficiency of 2.7%.

We implemented the optimized OPCPA design in our laboratory [57]. These results are discussed in detail in Section 2.3. Here, we only briefly compare them with our simulations. Because we did not use fully optimized optics, the effective pump energy available in the second OPA was only 40 μJ instead of the 50 μJ used in the simulations. All other experimental parameters closely match the simulations. When we take the lower second stage pump energy into account in our model, we find very good agreement between theory and experiment. We have measured a pulse energy of 100 nJ after the first amplification stage and 1 μJ after the second amplification stage corresponding to an average power of 100 mW at 100 kHz repetition rate. Simulations predict a somewhat higher pulse energy of 1.37 μJ. When operating the OPCPA at a center wavelength of 3.6 μm, we measured for the output pulses a FWHM bandwidth of 332 nm after the first OPA and 311 nm after the second OPA, which are close to our simulations predicting a bandwidth of 323 nm for the first and 313 nm for the second amplification stage. We characterized the compressed output pulses of the OPCPA using frequency-resolved optical gating and obtained a pulse duration of the recompressed OPCPA output of 95 fs. This corresponds to an 8-9-cycle pulse at this particular wavelength. We have not measured significant power from OPG.

2.2.6   Timing jitter considerations

One of the major practical issues of an OPCPA system based on two independent short pulse laser systems is the repetition rate locking of the two lasers with respect to each other. This is typically done by an electronic phase locked loop (PLL) [97]. The stabilization works well as long as the individual lasers exhibit no significant noise in average output power and pulse repetition rates. Therefore a solid mechanical design and a good isolation from environmental influences are a prerequisite to minimize the residual timing jitter between the two lasers. We have simulated the influence of a residual timing jitter on the performance of our two-stage OPCPA design. The two-stage amplification system has been modeled in two steps. The seed was identical to the previous simulation runs, stretched by 50 mm Al_2O_3. Pump and seed were focused down to 49 μm and 42 μm, respectively, inside the 3 mm long PPLN of the first OPA. The output pulse of the first stage was then calculated for different time delays between seed and pump. For

each of these time delays, the temporal profile of the output pulse is obtained by a weighted average across the transverse beam profile. The output from the first stage was then launched into the second OPA consisting of a 1.4 mm long PPLN crystal. The second stage was pumped with 43 µJ and with beam waists corresponding to our experimental values of 186 µm for the pump and 199 µm for the seed. Through the calculation with a longer than optimum PPLN crystal, it is possible to determine the point inside the crystal where the maximum amplified seed energy is reached. The time delay between the seed and the pump is the same in the second stage as at the input to the first stage. For the simulations, we neglect additional timing jitter due to mechanical instabilities introduced after the splitting of the pump pulse for the two stages.
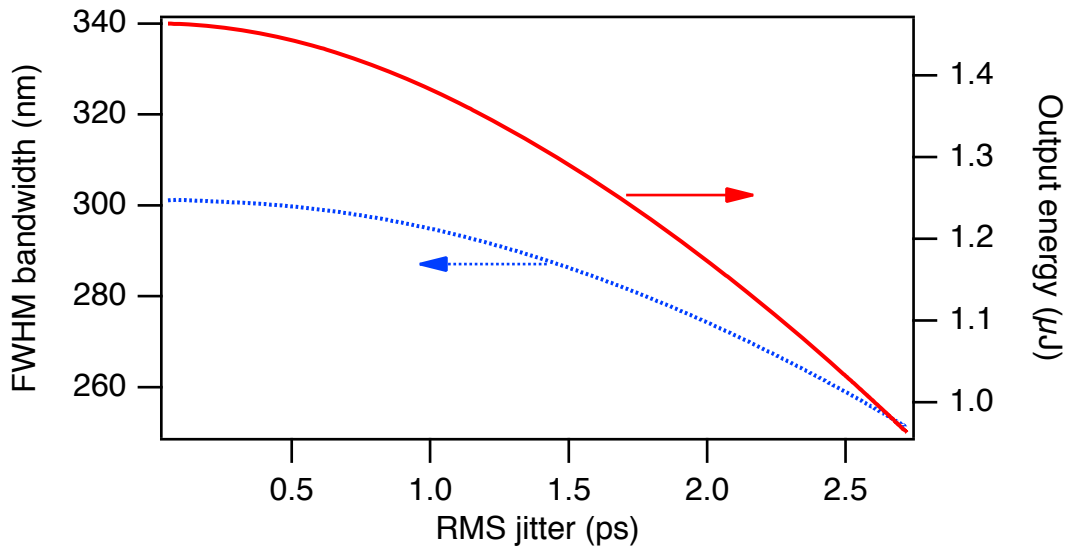
Figure 2.13: Dependence of the output power from the two-stage OPCPA on timing jitter. The power is plotted for the optimum PPLN length of 1.4 mm in the second OPA.

A normal distribution is assumed for the time delays introduced in our model and weighted averages of bandwidth and output energy are calculated for the different rms (root mean square) jitter values. Calculations have been performed with a resolution of 100 fs and a temporal span of the delay ranging from -5 ps to 5 ps. Figure 2.13 depicts the results from our model. A timing jitter of 1 ps reduces the output energy by 5% whereas the bandwidth is only reduced by 2%. Bandwidth is less affected than output energy. From the jitter simulations we can conclude that a timing jitter of less than 1 ps rms should only have a minor impact on the performance of our OPCPA system. The PLL electronics of our experimental setup (model CLX-1100 from Time-

Bandwidth Products) measured an in-loop timing jitter of below 200 fs. With recent improvements on the detection system, this was further reduced to well below 150 fs. This demonstrates that the repetition rate stabilization by our electronics is sufficient for our application and no direct optical stabilization of the fiber and pump lasers are needed [98]. The latter would be difficult to implement with the combination of laser sources used in our setup.

2.2.7   Alternative schemes

The previous Subsections have clearly shown that the combination of a modelocked picosecond solid-state and a femtosecond fiber laser amplifier system is a useful in the context of efficient generation of broadband mid-IR pulses at high repetition rates, avoiding many of the drawbacks of the more conventional Ti:sapphire based technology.

However, our simulations also show the bandwidth limitations of such an OPCPA system. At our operating wavelengths, the performance is limited by the phase matching bandwidth of PPLN. Noncollinear phase-matching cannot solve this problem because of the low power level. Overall conversion efficiency has to be traded against bandwidth since the temporal profile of the pump implies weak stretching of the seed for broadband amplification. The resulting small temporal overlap with the pump pulse makes only limited use of the available pump energy. The best achievable conversion efficiency is 5% of the input power. This value is obtained by stretching the seed with 100 mm of sapphire and pumping the two stages at 3.9 µJ and 50 µJ, respectively. This corresponds to a photon conversion efficiency of 19%.

One option to increase the efficiency is to use a flat top spatial beam profile instead of a Gaussian beam profile. To simulate the flat top beam we used a super-Gaussian of order 26 to pump the second OPA, while the first OPA was still pumped by a Gaussian beam profile. 50 mm of sapphire were used to stretch the seed. The flat beam profile increases the pulse energy after the second stage from 1.79 µJ to 2.36 µJ with a pump energy of 50 µJ. Bandwidth slightly decreases from 335 nm to 320 nm. A flat top temporal profile of the pump pulse would allow for longer stretching factors of the seed and thus for an improved temporal overlap with the pump.

In Section 2.4 we will discuss an alternative approach that overcomes many of the shortcomings of the PPLN based OPCPA modeled here. It replaces the PPLN crystals with aperiodically poled gain structures [18]. This novel gain medium offers large bandwidth and better pump/seed overlap at the same time.

2.2.8   Conclusion

We have shown the possibility to implement a femtosecond, high-repetition-rate, and high-power mid-IR OPCPA laser system starting from a commercially available diode-pumped solid-state pump laser and fiber seed laser. Our numerical model predicts optimized OPCPA performance using two amplification stages. From the currently available mid-infrared gain materials we concluded that MgO:PPLN was the most suitable choice with our concept. Best performance of the system is obtained when stretching the seed pulses through 50 mm of sapphire material. Optimization of the two OPA stages made us choose 4 µJ of pump energy and a 3 mm long PPLN crystal for the first OPA. The remaining part of the pump is sent into the 1.4 mm long PPLN crystal of the second stage. Numerical simulations were used to determine the optimum beam sizes in both OPAs. The numerical model gave us detailed insight into the gain process and let us identify a mode of operation where some of the bandwidth limitations through gain narrowing could be overcome by operating the OPAs in strong saturation. Our two-stage OPCPA design amplifies the seed obtained through DFG with an energy of below 10 pJ to the µJ-level. This corresponds to a gain of about 50 dB in a total of 4.4 mm PPLN material length. The OPCPA configuration optimized through simulations was built in our laboratory and the experimental results are consistent with the theoretical model (see Section 2.3 and [57]). This experiment was the first demonstration of an OPCPA system at such long wavelengths.

The proposed dual-stage OPCPA design with all its limitations holds a lot of promise for many femtosecond mid-infrared physics and chemistry experiments. Such experiments greatly benefit from the high repetition rate of this system, leading to shorter measurement times and/or improved signal to noise ratios. The average power is significantly higher than for most Ti:sapphire based optical parametric systems in this wavelength regime. As we will show in this Chapter, further scaling of repetition rate and average power is feasible.

2.3   OPCPA results with conventional PPLN

In this Section, we present experimental results from our new approach for a femtosec-ond mid-infrared laser source. Its main feature is that it delivers potentially carrier-envelope offset phase (CEP, [99]) stable pulses at high repetition rates. As outlined in the previous Section, it is based on optical parametric chirped-pulse amplification (OPCPA) [56, 100] and uses a commercially available diode-pumped solid-state laser as its pump and a commercial fiber laser amplifier for the CEP-stable seed generation. The pump laser is a Duetto from Time-Bandwidth-Products, whereas the mid-infrared seed is generated through difference frequency mixing of the two-branch output from an Er:fiber laser amplifier (FFS from Toptica) [61, 83]. The difference frequeny mixing signal is intrinsically CEP-stable [101, 102] and is expected to remain so even after am-plification in an OPA pumped by an unstabilized laser [96]. As we will show, this con-figuration of our OPCPA system produces sub-100-fs pulses with a pulse energy of up to ~1 µJ at a repetition rate of 100 kHz. To our knowledge this is the highest repetition rate from a mid-infrared OPCPA laser system. The generated pulses have an optical bandwidth of >300 nm and the central wavelength can be selected between 3.5 µm and 3.7 µm.
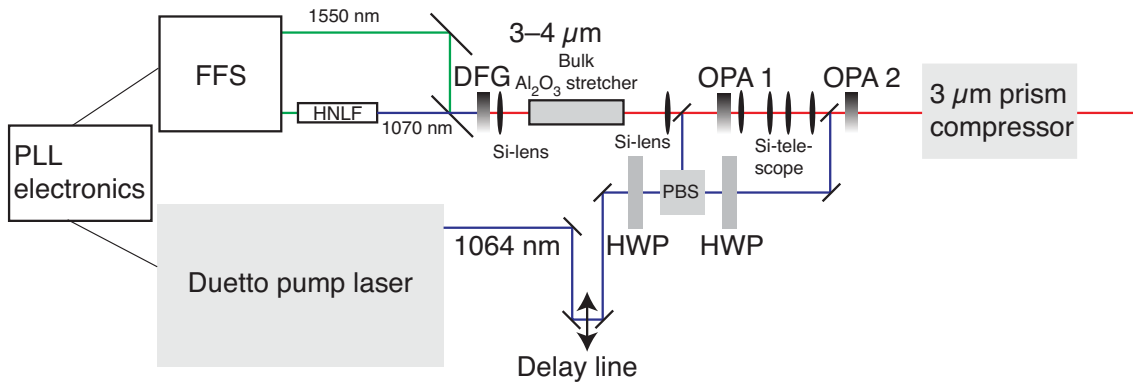
2.3.1   OPCPA design and results

Figure 2.14: Schematic setup of our OPCPA system. The three nonlinear optical stages DFG, OPA 1, and OPA 2 are based on MgO:PPLN crystals with lengths of 2 mm, 3 mm, and 1.4 mm, respectively. Lenses in the pump beam are not shown. (HWP, half-wave plate; PBS, polarizing beam splitter cube; HNLF, highly nonlinear fiber; FFS, fiber amplifier sys-tem).

A schematic setup of our OPCPA system is shown in Figure 2.14. The system configuration takes the form of a two-stage amplifier optimized for broadband output between 3 and 4 µm. The OPCPA seed is generated through difference frequency generation (DFG) from the two outputs of a commercially available two-branch Er:fiber laser/amplifier system and has been discussed in detail elsewhere [61]. In summary, one output of the 1.5 µm fiber laser is spectrally shifted in a highly nonlinear fiber to 1070 nm [60] and collinearly overlapped with the beam from the other branch in a 2 mm long MgO:PPLN crystal. In this DFG stage, up to 1 mW of mid-infrared radiation is generated at the full 82 MHz repetition rate of the fiber laser. This corresponds to a pulse energy of 12 pJ. The full-width-at-half-maximum (FWHM) spectral bandwidth reaches up to 360 nm. Using a MgO:PPLN device with a fan-out design permits us to tune the generated mid-infrared radiation between 3.4 and 4.8 µm. Simulations show that the pulses can be assumed to be close to their transform limit with a duration between 55 fs and 60 fs. This corresponds to about 5 optical cycles at 3.5 µm.

The Duetto pump laser in Figure 2.14 is a Nd:YVO$_4$ based amplifier system operating at 1064 nm. Its repetition rate is tunable between 50 kHz and 8 MHz and it provides 10 ps pulses with a pulse energy of 100 µJ at the 100 kHz repetition rate of our OPCPA system. Due to unoptimized beam routing and lossy optics, only 55 µJ of the total pump energy are used in our experiments. The pulse trains from the seed and the pump laser are locked to each other electronically with a commercial phase locked loop (PLL) detector (CLX-1100 from Time-Bandwidth-Products) [97]. We have employed the fiber laser as the master oscillator and are controlling the output of the oscillator of the Duetto. The residual in-loop timing jitter amounts to 170 fs rms. Although direct optical stabilization schemes could potentially provide better stability [98], these are difficult to implement for our system. The measured timing jitter is sufficiently low for our OPCPA design as demonstrated with the simulations in Subsection 2.2.6.

The mid-infrared seed is first collimated by an anti-reflection (AR) coated Si-lens with 30 mm focal length. The seed is then separated from the other two waves at 1.1 µm and 1.6 µm that are also present in the DFG stage by passing the beam through a germanium wafer under Brewster's angle. The seed pulses are temporally stretched in 50 mm of bulk sapphire (Al$_2$O$_3$) providing total group delay dispersion (GDD) of about -50'000 fs^2 and third order dispersion (TOD) of 330'000 fs^3 at 3.5 µm. This stretches the input pulse to a duration of 2.4 ps. While one would expect to achieve the best con-

version efficiency with a seed pulse duration approximately matching to the pump pulse duration, we optimized our system for maximum amplification bandwidth. The underlying design considerations have been discussed in detail in Subsection 2.2.3. These simulations revealed that the highest amplification bandwidth for our OPCPA design could be achieved with a seed pulse duration in the range of 1 to 3 ps. Furthermore, simulations also show that we obtain larger output bandwidth by operating the first OPA stage in strong gain saturation. In this regime, the pump pulse is saturated first around the peak of the seed pulse. The temporal wings of the strongly linearly chirped input pulse saturate their gain later and may thus experience a larger overall amplification factor for a sufficiently long nonlinear medium. This leads to a spectral broadening due to the frequency-to-time mapping resulting from the strong chirp. A seed pulse that is too long, on the other hand, experiences time-dependent gain leading to gain narrowing.
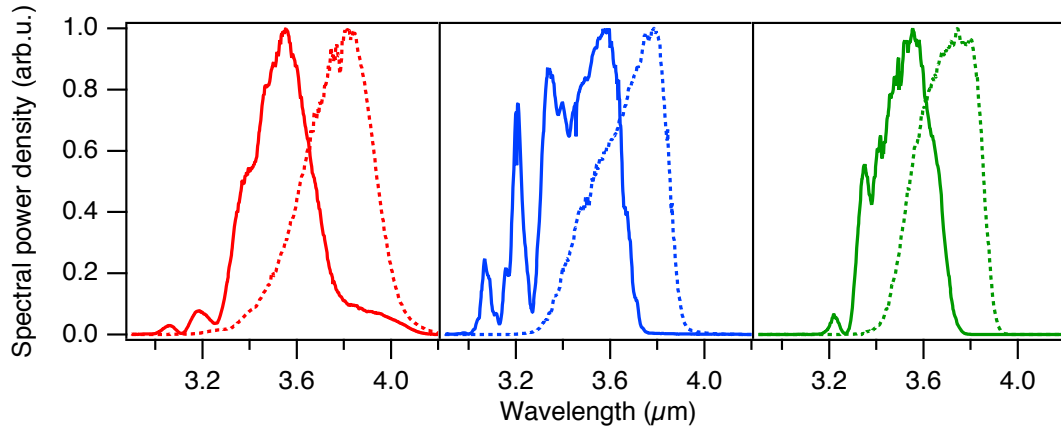
Figure 2.15: Measured and normalized mid-infrared spectra directly after the DFG seed source (left), after the first amplification stage (middle) and after the second amplification stage (right). All spectra were recorded with a scanning monochromator equipped with a HgCdTe (MCT) photodiode connected to a lock-in amplifier. The solid lines correspond to the OPCPA operating at a center wavelength of 3.5 µm, whereas the dashed lines show operation at 3.7 µm.

The stretched 3.5 µm seed beam with 0.8 mW of average power and 9.8 pJ pulse energy is refocused by a Si-lens with 75 mm focal length into the first OPA stage. The resulting $1/e^2$ beam radius is 42 µm. The measured seed spectrum is shown in the left-most part of Figure 2.15. The first OPA consists of a 3 mm long, uncoated MgO:PPLN crystal with 7 different quasi-phase matching (QPM) grating periods (28.76, 29.30, 29.86, 30.46, 31.10, and 31.78 µm). The selected gratings allow phase-

matching a 1.064 µm pumped OPA between 2.5 µm and 4.0 µm. This covers the main operation range of our DFG seed source. For our experiments, we fully characterized the system with phase-matched center wavelengths of 3.5 µm and 3.7 µm. The results at 3.7 µm are discussed in more detail below.

The time delay between the pump and seed pulses is fine-tuned with an optical delay line. A coarse tuning of the delay is achieved with the electrical signal cable length between the two PLL detector photodiodes near the two oscillators and the PLL electronics. After the delay line, the pump beam is split into a small part used to pump the first OPA (4.7 µJ) and the rest pumping the second OPA stage (47 µJ). The pump beam for the first OPA is focused by a lens with 250 mm focal length and overlapped collinearly with the seed beam on a dichroic mirror. The resulting pump beam radius reaches a $1/e^2$ value of 49 µm inside the PPLN. The effective pump energy is 3.9 µJ after accounting for the reflection losses on the uncoated nonlinear crystal. This is sufficient to amplify the seed to 9.7 mW average power or 97 nJ pulse energy at a central wavelength of 3.5 µm and the 100 kHz repetition rate of the pump. The amplified idler is then separated from the signal wave located at 1.58 µm and the pump at 1.064 µm by transmission through a germanium wafer under Brewster's angle. The idler beam is subsequently recollimated by an AR coated Si-lens with 75 mm focal length. The measured FWHM bandwidth of the amplified spectrum after the first OPA stage is 340 nm (see Figure 2.15, middle).

A telescope consisting of two Si lenses with 200 mm and -100 mm focal length then reduces the size of the output beam from the first OPA. This beam is refocused by another Si-lens with 150 mm focal length. The remaining pump beam passes through another optical delay line for fine tuning of the delay inside the second OPA and is then focused by a 250 mm focusing lens. Again, the pump and the signal beam are overlapped collinearly on a dichroic mirror. The measured focal beam radii amount to 180 µm for both beams.

The second OPA stage consists of an uncoated, 1.4 mm long MgO:PPLN crystal. By pumping the second OPA with an effective 39 µJ, the idler is amplified to 0.95 µJ, corresponding to an average power of 95 mW. The measured spectral FWHM spans 332 nm at 3.5 µm, supporting 79 fs pulses (see Figure 2.15, right). This corresponds to 6 to 7 optical cycles at this wavelength.

We have measured a parametric superfluorescence background of 0.4 mW after the first amplifier and 5 mW after the second amplification stage when blocking the seed beam. This may serve only as a worst-case estimate for the actual superfluorescence background as the superfluorescence background competes for gain with the amplified seed under normal operating conditions.

The mid-infrared idler is separated from the pump by a dichroic mirror. This is to prevent an unnecessary thermal load in the collimating Si-lens through the unused pump light. Without this dichroic mirror, we observed damage to the mid-infrared AR coating of the lens and distortions of the transmitted beam. The signal beam is only partially removed by the dichroic mirror. A small fraction of the reflected signal is sent onto a photodiode and used as part of a slow feedback loop stabilizing the pump-seed delay. This ensures long-term stability even in the presence of room temperature and air pressure fluctuations. A lens with 100 mm focal length recollimates the final output beam after the second OPA.

When the OPCPA is operated at 3.7 µm (dashed lines in Figure 2.15), 0.5 mW of DFG seed power are amplified to 9.6 mW in the first OPA. The output power after the second OPA amounts to 88 mW. The bandwidth was measured to 326 nm FWHM after the DFG, which is subsequently broadened to 331 nm in the first OPA. The output bandwidth after the second amplification stage was 313 nm and supports 87 fs pulses.

2.3.2   Pulse compression and characterization

We have compressed the output of the OPCPA system with a 4–prism compressor, where the beam passes the four uncoated silicon prisms under Brewster's angle (Figure 2.16, [103, 104]). Simpler compressors such as bulk silicon, which provides the opposite sign of GDD compared to sapphire and $LiNbO_3$, or a classical two–prism compressor [105] can also introduce the desired amount of GDD. However, these simpler approaches possess the same sign of third order dispersion (TOD) compared to sapphire and $LiNbO_3$. In contrast to the 4-prism compressor, they are therefore not suitable for TOD compensation. The relatively high refractive index of silicon yields a Brewster's angle of 73.7°. This results in the beam geometry shown in Figure 2.16, where the total beam deflection angle over one prism pair is larger than 180°. As a consequence, the different beams cross in the middle of the two prism pairs depending on the required

prism apex distance. The amount of prism bulk material along the beam path can be increased by moving the two prism pairs towards the center of the compressor, unlike the behavior of more conventional prism compressors. So far, the throughput of our prism sequence is limited to 41%. This corresponds to a transmission of ~90% per prism. The main contribution to the losses is likely due the large Brewster's angle on the prism: small deviations from the ideal angle lead to significant losses as the reflectivity steeply rises within the few remaining degrees towards grazing incidence. A total of 16 silicon-air interfaces are passed through the entire compression path.
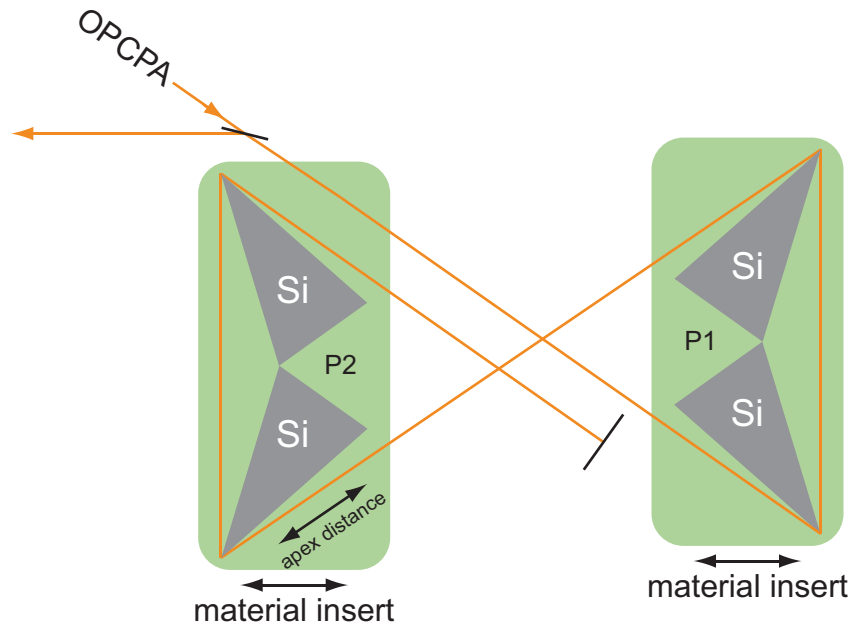
Figure 2.16: 4-prism compressor setup based on two pairs of silicon prisms (P1 and P2).

With this setup we were able to compress the pulses to 92 fs. Pulse characterization was performed with second-harmonic generation frequency-resolved optical gating (SHG FROG, [106]). Our SHG FROG setup employed a 250 µm thick silver gallium selenide (AgGaSe$_2$) crystal to generate the second harmonic signal. The generated spectra ranging from 1.5 µm to 2 µm have been measured with a scanning monochromator equipped with an extended InGaAs photodiode connected to a lock-in amplifier. The FROG trace was recorded on a (128x128) grid. The acquisition of a complete FROG trace in Figure 2.17 took more than one hour because we had to scan both the monochromator grating and the pulse delay in the FROG setup. Thus, this measurement also serves as a demonstration of the stability of our OPCPA system.
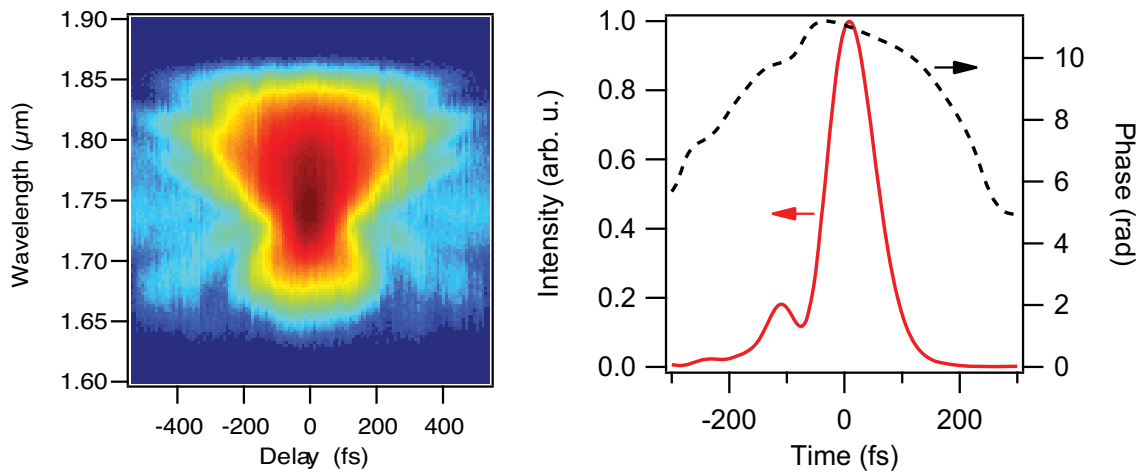
Figure 2.17: Measured FROG trace (left) with retrieved pulse shape and phase (right)

2.3.3 Conclusion

We have demonstrated a femtosecond mid-infrared OPCPA laser system based on reliable, compact and commercially available solid-state and fiber laser technology. Our system operates at a high repetition rate of 100 kHz and delivers output pulses at center wavelengths of 3.5 µm and 3.7 µm with a pulse energy of ~1 µJ. We have compressed the pulses to a duration of 92 fs. To our knowledge this is the highest repetition-rate OPCPA system in the mid-infared demonstrated so far. However, our work on OPCPA using conventional PPLN as the gain medium also revealed several shortcomings of this concept. The most serious limitation with respect to our goal of generating intense, CEP-stable few-cycle pulses is the insufficient amplification bandwidth provided by the PPLN crystal. We solved this problem by switching the OPA stages to aperiodic quasi-phase matching as discussed below.

2.4 OPCPA with aperiodically poled gain structures

The generation of few-cycle pulses in the mid-infrared region is a challenging task because known laser crystals do not supply optical transitions with sufficient amplification bandwidth. Nonlinear optical frequency mixing is a common approach for generating short pulses at wavelengths where suitable laser crystals are not available [89]. In the mid-infrared, this approach relies – with a few exceptions – heavily on Ti:sapphire

technology with its associated cost, average power limitation, and limited wall-plug efficiency.

Our work using conventional PPLN as the amplifcation medium has demonstrated before that optical parametric chirped-pulse amplification (OPCPA) directly pumped by diode-pumped solid-state lasers operating around 1-µm wavelength is a powerful method for amplifying sub-100 fs pulses in the mid-infrared at high repetition rates [57, 59]. Our numerical simulations, however, have shown that the achievable bandwidth while maintaining efficient amplification is limited with this gain medium (see Section 2.2 and [58]). For the specific pump and seed wavelengths and parameters of our system, maximum bandwidth was found to be on the order of 300 nm at 3.6-µm center wavelength. To overcome this constraint while keeping the benefit of the high nonlinearity of PPLN, we use chirped quasi-phasematching (QPM) for femtosecond optical parametric amplification. The concept of chirped or aperiodic QPM for increased acceptance bandwidth and even pulse shaping has previously been successfully applied to other nonlinear optical interactions.

While the first proposal of chirped QPM was limited to the idea of extending the acceptance bandwidth for cw second harmonic generation (SHG) [107], it was soon realized that chirped QPM also has interesting properties for the broadband conversion of ultrashort optical pulses [108]. The first application was to exploit the localized conversion of different frequency components in aperiodically quasi-phase-matched SHG for phase shaping and compression of the output pulses [108] and was soon extended to more general pulse shaping [109]. The phase shaping and very large bandwidth of these devices was exploited for the production of sub-6-fs pulses by second harmonic generation from Ti:sapphire few-cycle pulses [110, 111]. The idea of aperiodic QPM was also transferred to other applications of second order nonlinearities such as optical parametric amplifiers (OPA) [112] and optical parametric oscillators (OPO) [113]. However, to our knowledge, there exists no prior experimental demonstration of femtosecond OPA or OPCPA using aperiodic QPM. It turns out that the extension of the approach to this particular application is non-trivial. Several critical aspects of aperiodical QPM OPAs have been addressed in References [15-17].

In this new amplification medium, near-arbitrary bandwidths are possible because the grating provides the range of k-vectors to phasematch all frequencies of interest. The spectral gain of such a device is inversely proportional to its chirp-rate (k-

vector change per unit length) [15]. For a given chirp-rate and gain, the available band-width is proportional to the length of the device and, thus, only extrinsically limited by the transparency range of the material, and practically available crystal sizes. The grating can be engineered to overcome spectral gain narrowing, tailor the group delay spectra, and improve efficiency by reducing back-conversion [15, 19]. These capabilities enable pulse durations beyond what was possible by conventional means with the given input parameters.

2.4.1   Design and results
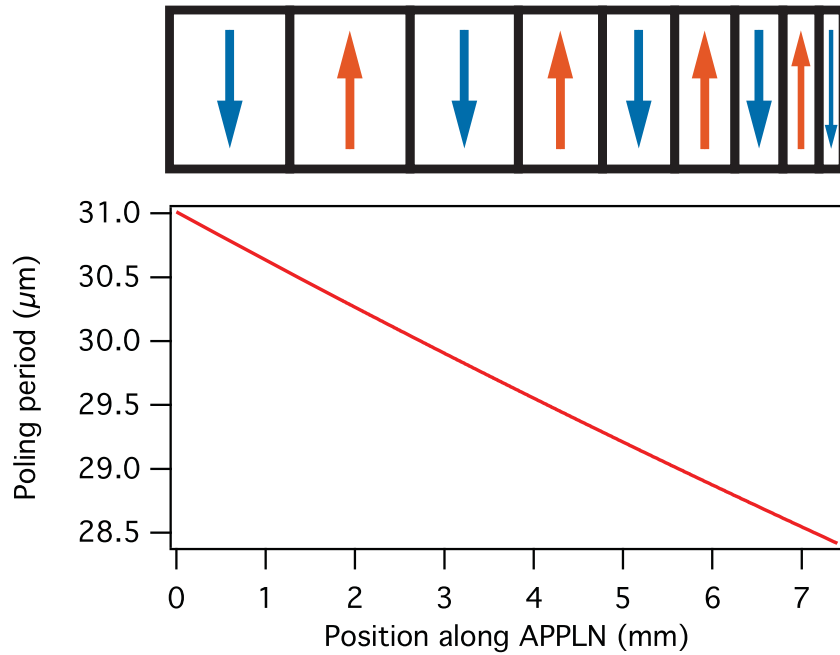
Figure 2.18: The grating used has a length of 7.4 mm and a negative chirp rate of $\kappa' =$ -250 cm^{-2}. It has perfect phase matching points for wavelengths in the range from 3 to 4 µm.

For our first demonstration, the local QPM period is varied smoothly across the range of phasematching k-vectors for the idler bandwidth. The grating k-vector is varied linearly (Figure 2.18), which in the near-field limit and small bandwidth leads to a flat amplification spectrum with low-order polynomial phase suitable for subsequent compression. Amplification occurs for each spectral component around its phasematched point until the local phase mismatch becomes too large, or until the pump is significantly depleted. In contrast to periodically poled gratings where pump depletion is followed by complete

back-conversion in a sufficiently long grating, in aperiodically poled lithium niobate (APPLN) pump depletion increases monotonically with pump and seed intensity, except for ripples associated with abrupt on and offset of phasematching at the edges of the grating [19]. These ripples can be suppressed by apodization techniques, which reduce the local coupling strength by adiabatically increasing the phase mismatch (increasing or decreasing the QPM period) or by reducing the effective coupling coefficient, for example by reducing the QPM duty cycle [15]. Misalignment of pump and seed can occur when optimizing the amplifier gain in the laboratory, leading to a self-apodization effect where the beam interaction is gradually turned on as the beams walk across each other through the crystal.

We use two optical parametric amplifier stages designed to operate in the mid-IR around 3-4 µm wavelength. The system is seeded by the intrinsically carrier-envelope offset phase (CEP) stable difference frequency generation (DFG) setup already discussed in the previous Sections of this Chapter. It delivers pulses from 50-100 fs in the spectral region from 3.2 µm to 4.8 µm [61]. This seed source is expected to enable CEP-stable output pulses from our amplifier. Both OPA stages are pumped at a wavelength of 1.064 µm with a slightly upgraded version of the same commercial solid state laser used for the PPLN based experiments. It delivers 11 ps pulses at energies of up to 120 µJ and a repetition rate of 100 kHz (Time-Bandwidth Products AG, Duetto). By using a 1-µm pump laser technology, power scaling should be easy to achieve. As before, the pulse train of this laser is stabilized to the pulse train of the seed laser with a phase locked loop (PLL) yielding a timing jitter of less than 150 fs rms [97].

The pulses of our mid-infrared seed source are stretched to approximately 2.5 ps by propagation through 50 mm bulk Al_2O_3. The two OPA crystals are 7.4-mm long uncoated MgO:APPLN with a poling structure illustrated in Figure 2.18. With a chirp rate of $\kappa' = -250$ cm^{-2} (defined as the slope of the spatial frequencies of the grating) we could achieve an amplification bandwidth of more than 800 nm (Figure 2.19). In the first stage the obtained gain is 40 dB and the second stage adds another 14 dB resulting in pulse energies of up to 1.5 µJ at a repetition rate of 100 kHz, which corresponds to 150 mW of uncompressed average output power. Due to pump depletion the spectrum is broadened after the second stage, supporting 54-fs transform-limited pulses. This occurs because the central spectral components are saturated before the wings. Ripples on the spectra (Figure 2.20) and the corresponding pre-pulses on the com-

pressed pulse originate primarily from the abrupt onset of nonlinear coupling at the ends of the grating, and can be suppressed by apodization of the QPM grating as discussed above [15].
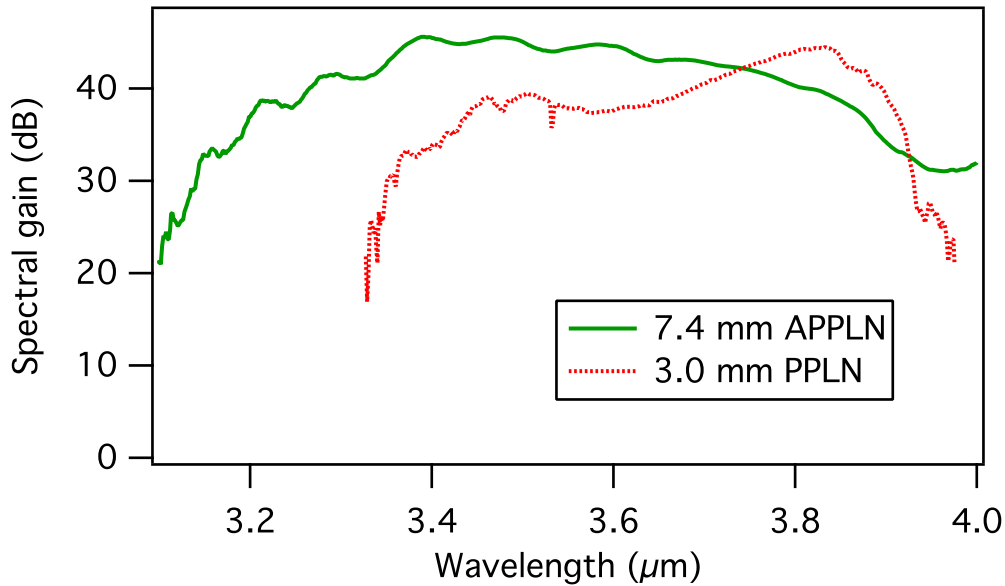
Figure 2.19: Gain spectrum of the first OPA stage (green solid line), showing more than 800 nm amplification bandwidth when pumped at 1.9 GW/cm^2. The measurement is limited only by the available seed bandwidth, giving rise to noise in the spectral wings. The red dotted curve is the measured gain spectrum of a 3 mm long conventional PPLN device as used for OPA 1 in our previous experiments.

After compensation of second and third order dispersion with the same 4-prism silicon compressor setup introduced in Subsection 2.3.2 [103], we reached a nearly transform limited pulse of 75 fs (Figure 2.21). The transmission of the compressor amounted to only 30% due to an increased sensitivity to misalignment and the effect of surface roughness at the near-grazing-incidence on the silicon Brewster prisms at our operation center wavelength of 3.4 µm.

APPLN OPAs are sensitive to optical parametric generation (OPG, or parametric superfluorescence) because quantum noise can be amplified throughout the whole grating [17]. In contrast, the seeded collinear amplification process occurs only over a relatively small region for each spectral component. This results in an unwanted OPG background, which can be suppressed by using two short amplification crystals, pushing the required gain below the OPG threshold.
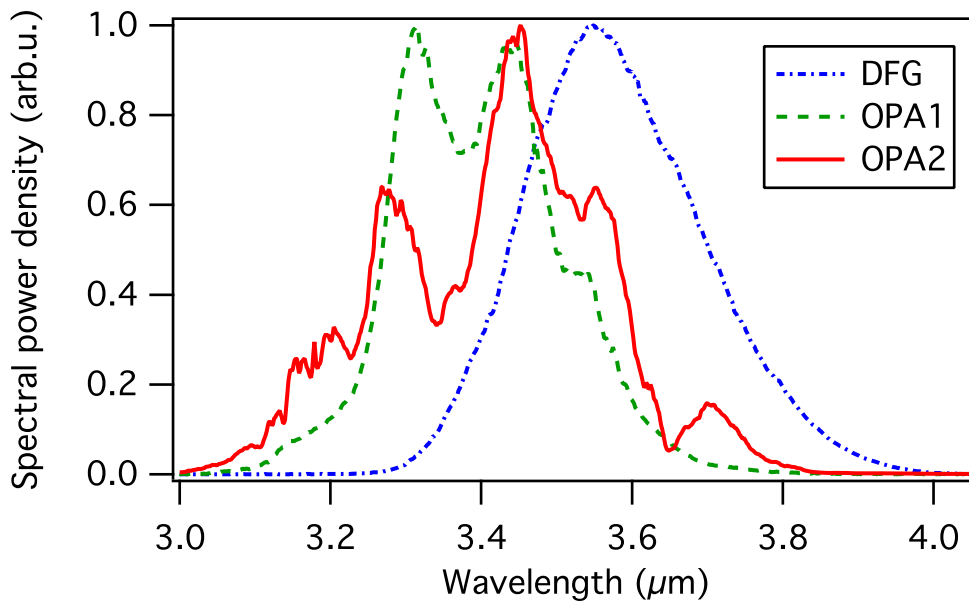
Figure 2.20: The power spectrum of the seed (blue, dash-dotted) supports 71-fs transform limited pulses. After the first amplifier (green, dashed) the spectrum is broadened, supporting 65-fs pulses, and further broadened after the second amplifier (red, solid) providing bandwidth for 54-fs pulses.
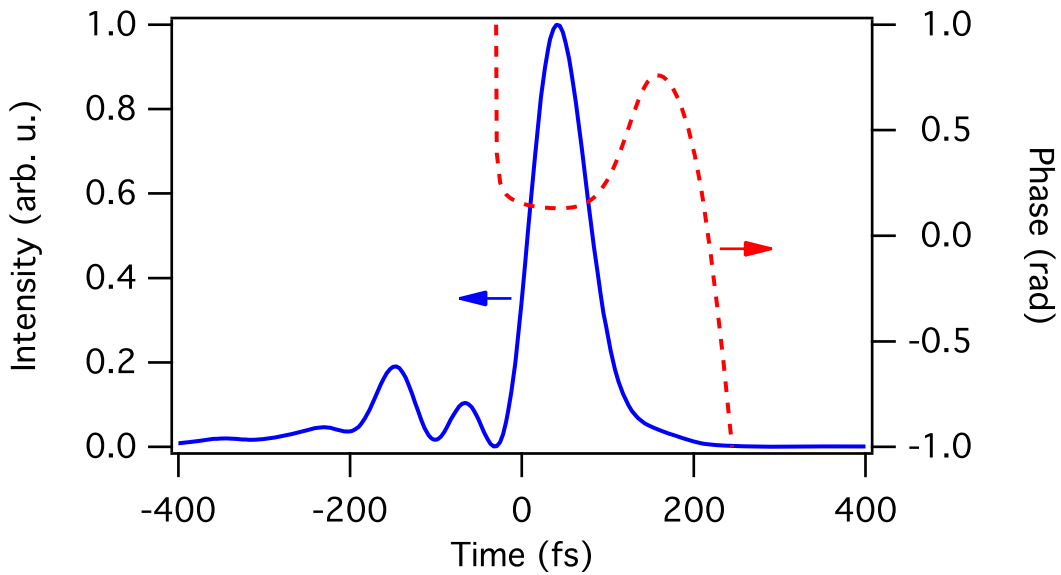
Figure 2.21: After compensation of GDD and TOD the pulses are compressed to 75-fs FWHM.
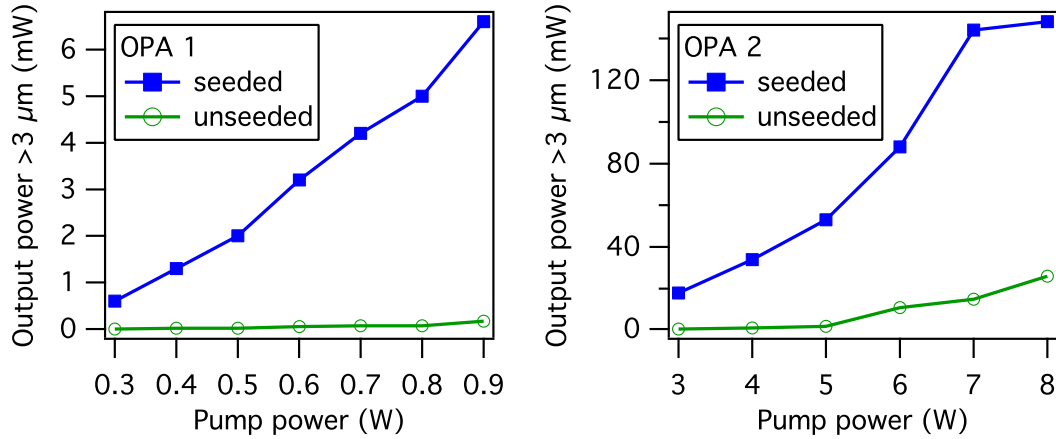
Figure 2.22: The left graph shows the power scaling of OPA 1. There is only negligible OPG output. In the right graph one can clearly see the amplification of the remaining OPG of OPA 1. This can be suppressed by the use of a steeper long-pass filter between the two OPA stages. A completely unseeded OPA 2 generates less than 2 mW OPG.

Nevertheless, some OPG remains. For our QPM grating design this occurs primarily below 3 µm and can be spectrally filtered with a long-pass filter. To estimate an upper limit for the remaining OPG power we did a conservative analysis by measuring the unseeded output power of both OPAs. After the first OPA stage there is nearly no measurable radiation above 3 µm (Figure 2.22). When the input to the second OPA is blocked, the OPG is below 2 mW of the amplified seed power, which confirms that the amount of spontaneous radiation after the second stage is still small. If one directs the small remaining OPG output (mostly leakage of our long-pass filter) of the first OPA into the second stage the output power is 25 mW (Figure 2.22). This means that an appropriate filter with higher suppression of the radiation below 3 µm from the first OPA could suppress the overall OPG contribution to less than 1.5%.

2.4.2   Summary and conclusion

With APPLN one can overcome the bandwidth limitations of conventional PPLN in a collinear OPCPA. We have demonstrated this new amplification concept with a femtosecond mid-infrared OPCPA based on aperiodically poled $MgO:LiNbO_3$ crystals. In this first implementation we used linearly chirped gratings and were able to achieve 75 fs output pulses characterized by SHG-FROG [106], maintaining the 72 fs transform limit of the seed. With the DFG seed source, we do not fully exploit the amplification

bandwidth of our APPLN devices. The spectral ripples and temporal pre-pulses that we observe are understood and can be suppressed with apodization.

Other issues associated with conventional OPCPAs can be overcome with APPLN. QPM engineering can be used to achieve a flat gain profile even with a non-flat-top temporal pump profile. This allows for a better pump-seed temporal overlap without experiencing the significant gain narrowing that would occur with traditional gain media (e.g., see Subsection 2.2.4). With tandem amplifier designs [114] the group delay of the pulses can be engineered to achieve transform limited output pulses over the large bandwidth offered by these devices. Furthermore, with APPLN the intrinsic damage threshold of the material is no limitation to the bandwidth anymore as was the case with our previous PPLN based implementation. Finally, back-conversion limiting efficiency and spectral broadening in conventional PPLN devices is significantly reduced in APPLN [19].

This first generation APPLN design clearly shows the potential of the technique and holds promise for significant further improvements of pulse duration and system efficiency. With an upgraded seed source bandwidth and improved QPM designs, the output of our system can be expected to reach into the few-cycle regime (one cycle at $3.4\,\mu m$ is $11.3\,fs$). Some of the more recent results with the aperiodic quasi-phase matching approach and the corresponding improvements of the performance of our system are discussed below.

2.5 New seed concept and power scaling

While the APPLN devices allowed us to overcome the bandwidth limitation of the amplification sections in our OPCPA system, additional bottlenecks or conceptual issues could be identified during this work. Namely, the problematic areas in our system are the following:

- Compressor throughput. Our current implementation using a 4-prism compressor (Figure 2.16) suffers from an extremely low throughput of only 30 to 40%. This is thus not better than a comparable grating compressor and wastes a lot of the expensive mid-infrared photons.

- Compressor bandwidth. Prism and grating compressors introduce significant higher order dispersion. Furthermore, bandwidth is also constrained by geometry in these types of compressors (angularly dispersed beams not fitting on the finite apertures of the optics). It is therefore not clear how our prism compressor concept could be scaled to the large bandwidths of true few-cycle pulses.

- Low seed pulse energy. Our available seed energy is only on the order of 10 pJ. This increases our susceptibility to parametric superfluorescence (high gain in first OPA stage). Furthermore, the low seed power in conjunction with its difficult-to-handle wavelength renders alignment of the system a tedious task.

- Low seed bandwidth. Our seed bandwidth is not sufficient for reaching true few-cycle operation of our OPCPA. In fact, our APPLN based results are entirely seed limited with respect to the achieved bandwidth. Due to the low seed energy, additional nonlinear spectral broadening of the seed is not an option.

The combination of these issues is serious enough to prevent us from reaching our original goal of generating intense, CEP-stable few-cycle pulses in the mid-infrared. A modification of our concept therefore needed to be found to overcome these limitations. It was found that a change of the seed source solves all of the above problems.

2.5.1 New seed source

The new seed approach is depicted in Figure 2.23. Rather than converting the output from our femtosecond fiber laser system into the mid-IR to obtain a suitable idler seed, we use it to seed the first OPA stage at the signal wavelength directly. This step yields immediately two orders of magnitude higher seed pulse energy (1.8 nJ). Furthermore, alignment is simplified because of the higher power and a center wavelength that is easier to handle as we can rely on proven 1.5-µm technology. The easier alignment enables us to use a more complex stretcher setup. We use a combination of a transmission grating stretcher and a two-prism stretcher. The latter uses the same silicon Brewster prisms that were previously used in our compressor. The grating stretcher is set up in a near-zero dispersion 4-f configuration. This will later on allow us to add a liquid crystal

pulse-shaping device to the setup for ultrabroadband fine dispersion control [115]. Spatial light modulators operating at 1.5 µm are available commercially.
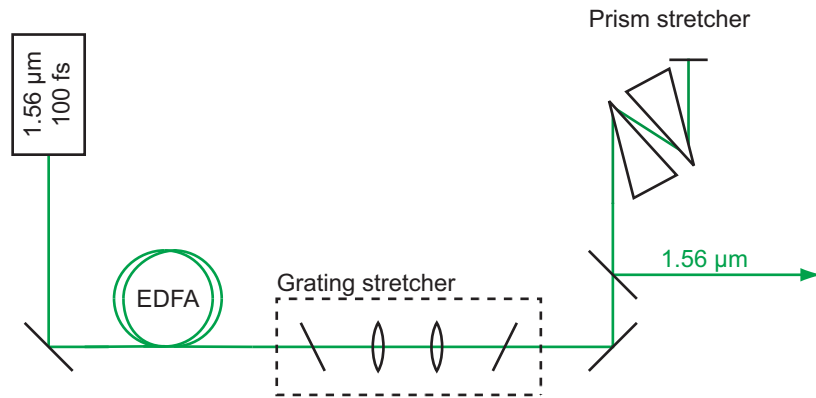
Figure 2.23: The new seed setup. The output of our femtosecond Er:fiber laser is directly used as the seed of the first OPA stage of the OPCPA. Its amplified (EDFA, erbium doped fiber amplifier) output pulses pass through a 4-f (near-zero dispersion) grating stretcher and a prism stretcher.

In addition, the higher pulse energy and the associated high peak power of our 1.56-µm seed allow us to implement nonlinear optical spectral broadening schemes. The bandwidth directly available from the fiber laser corresponds to a transform limited pulse duration of 55 fs. For further pulse shortening, nonlinear pulse compression schemes are required. We plan to exploit continuum generation in PPLN waveguides for this purpose [116].
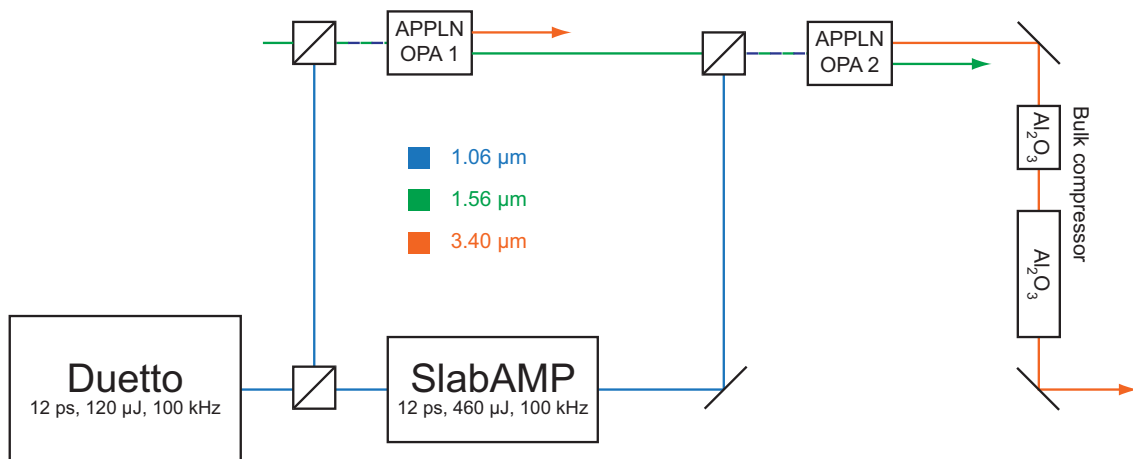
Figure 2.24: New OPCPA concept. We discard the mid-infrared idler beam after OPA 1 and rather use the amplified 1.56 µm signal beam as the input to OPA 2. We only keep the mid-infrared idler after the last amplification stage. Compression occurs in bulk sapphire.

The new seed source affects our OPCPA setup as shown in Figure 2.24. The 1.56-µm seed beam is amplified in OPA 1. We now discard the mid-infrared idler beam after OPA 1 and use the 1.56 µm signal beam as the input to OPA 2. This is made possible by the collinear geometry of our amplifiers. Both OPA stages still use the same APPLN devices reported in Section 2.4. The idler output of OPA 2 centered at 3.4 µm is then compressed in a bulk sapphire (Al_2O_3) compressor. The new bulk compressor eliminates the bandwidth and throughput limitations of our previous prism compressor. This setup now also uses the upgraded pump source discussed in Section 2.1.

The price one has to pay for the change in seed source is the loss of the passive CEP-stability that our DFG-based seed offered [61, 101]. While the active (electronic) locking of two independent oscillators as required in our case is not trivial, it is a solved problem [117]. An alternative scheme for optical locking of the seed and pump lasers cannot be easily transferred to our specific primary laser sources but might be an attractive solution for future implementations of similar OPCPA concepts [49, 98]. The electronic locking of seed and pump oscillator brings the benefit of direct and rapid control of the CEP through electronic means.

2.5.2   Initial results

In the following, we present initial experimental results that were obtained with the new seed concept and the upgraded pump laser. For these first measurements, we did not yet use a pulse-shaping device in the seed beam path and no external spectral broadening of the seed was performed. Already these first data sets, however, reveal the large potential of the new approach.

Our amplifier is again a two-stage optical parametric chirped-pulse amplifier (OPCPA) based on APPLN with the same gain crystals previously used for the results presented in Section 2.4. A mode-locked femtosecond fiber laser operating at λ = 1.56 µm is used to seed the OPCPA with 1.8 nJ of energy. Its spectral bandwidth supports 55-fs transform limited pulses. The pump source is an industrial laser (Time-Bandwidth Products Inc., Duetto), delivering 12-ps pulses at a repetition rate of 100 kHz and average output power of up to 11 W. About 10% of the output from the Duetto is further amplified in the $Nd:YVO_4$ slab amplifier described in detail in Section 2.1.

The seed pulses are stretched with a silicon prism stretcher to about 6 ps pulse duration to ensure good temporal overlap with the pump pulse. The two beams are over-lapped in the first and second OPA stage at pump intensities of 6.8 GW/cm^2 and 9.4 GW/cm^2, respectively. In both stages we use a 10-mm-long, 1-mm-wide APPLN chip. A chirp-rate of $\kappa = -250$ cm^{-1} is used to achieve a broad phase-matching spectral window ranging from 2.71 to 4.24 µm. The negative chirp rate is chosen to better sup-press the effective lens effects of the pump due to the parametric frequency conversion [118]. This focusing can lead to deterioration of the beam quality
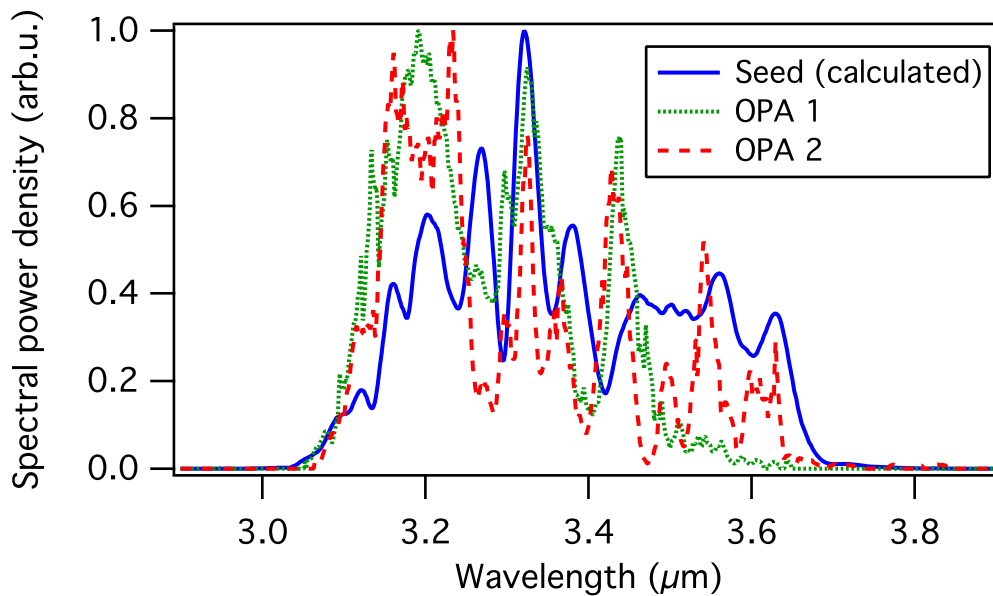
Figure 2.25: Idler spectra at different positions along OPCPA system. The seed spectrum (blue solid curve) was calculated from the input spectrum measured in the 1.5 µm signal spectral region. The small loss of bandwidth at long wavelengths after OPA 1 (green dotted curve) can be attributed to missing poling domains in the used APPLN crystal. This band-width is recovered in OPA 2 (red dashed curve).

The first stage generates an idler output spectrally centered around 3.3 µm with an output power of 75 mW (8 W pump) and a transform-limited pulse duration of 69 fs (Figure 2.25). The idler is amplified up to 1.4 W (30 W pump) after the second stage and spectrally broadened to support a bandwidth for 56-fs pulses, which corresponds to 5 optical cycles (Figure 2.25). We loose some spectral power on the long wavelength side of the spectrum in OPA 1. This is due to missing poling domains at the end of the crystal (Figure 2.26). As there are still photons present, this bandwidth is recovered in OPA 2. Our measurements show that the APPLN crystals are capable of amplifying the

full bandwidth of our current seed source. The spatial beam profile is well-behaved and allows focusing into a small area for reaching high intensities (Figure 2.27a). The power scaling of both stages as well as the estimated optical parametric generation (OPG) background are illustrated in Figure 2.27b) and c).
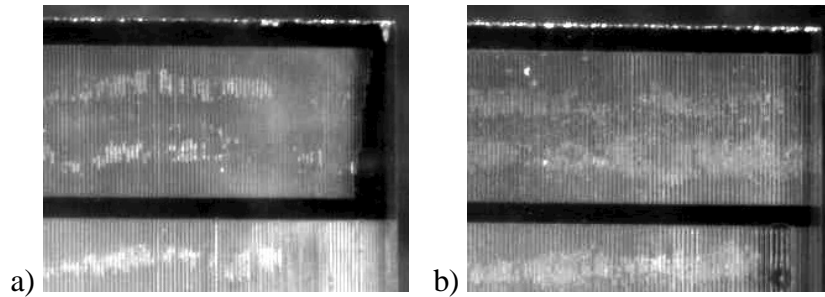
Figure 2.26: Microscope images of the APPLN chips of OPA 1 and OPA 2. a) QPM grating used in OPA 1. It can be clearly seen that some domains are missing towards the right hand side. b) QPM grating used in OPA 2.
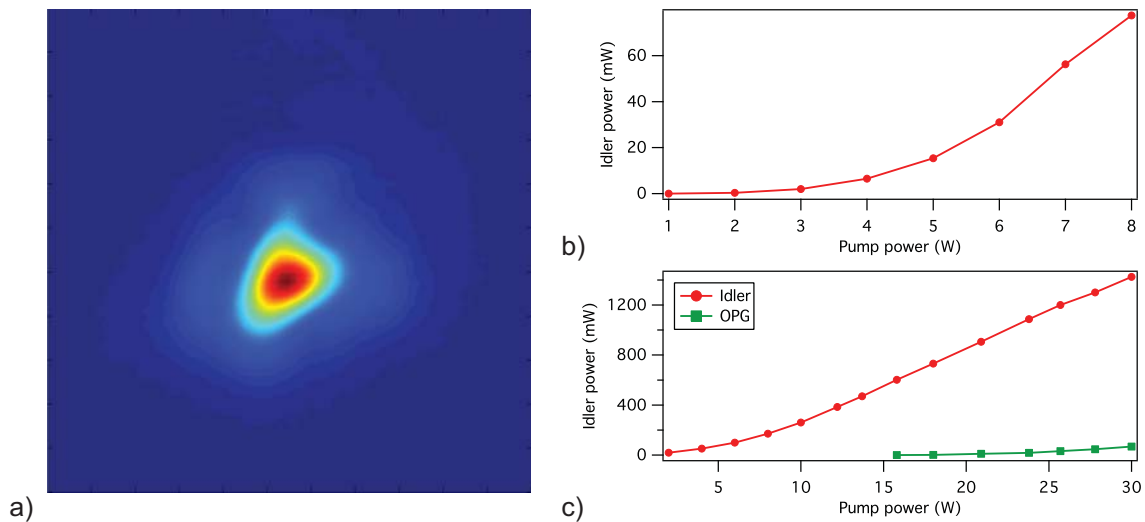
Figure 2.27: Output beam profile and power scaling. a) Spatial beam profile at 1.4 W of idler output power (linear color scale). b) Power scaling of OPA 1. c) Power scaling of OPA 2. The OPG level is below measurement threshold (10 µW) while blocking the seed for OPA 1. The output of OPA 2 shows OPG background below 5% at maximum output power and 0.2% at half output power.

As pointed out above, care needs to be taken in APPLN OPAs to avoid optical parametric generation (OPG). Quantum noise can be amplified throughout the entire grating via non-collinear phasematching [17]. This is in contrast to the seeded collinear amplification process, which occurs for each spectral component over only a relatively small region. This increased noise gain leads to an unwanted OPG background, which we suppress using two amplification stages (reducing the gain required in the first stage) and sufficiently large beam diameters to prevent non-collinear gain guided modes [17]. As an overestimate of the OPG in the saturated-amplifier regime, the idler average power was measured while blocking the seed of the first stage and feeding its output into the second stage. This resulted in 0.2% OPG at 700 mW and 5% at 1.4 W output power.
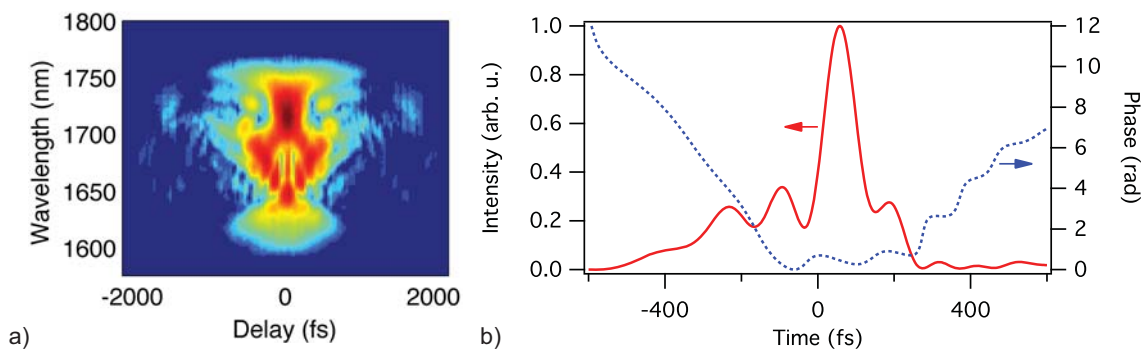
Figure 2.28: FROG data from initial compression attempt. a) FROG trace. b) Reconstructed pulse shape and temporal phase. In this first compression result with the new concept still a lot of higher order phase is not compensated, resulting in significant pedestals on both sides of the pulse.

We did a first compression attempt with the new OPCPA concept. For this purpose we used a total of 150 mm of bulk sapphire in the output beam. The bulk compressor consists of two uncoated rods of 100 mm and 50 mm length, respectively. Despite the still missing antireflection coating, we now obtain a compressor throughput of 76%. During our compression experiments, the OPCPA system was running at somewhat reduced performance compared to the 1.4 W of uncompressed output power observed earlier. Nevertheless, we end up with 8 µJ pulses after compression with a FWHM duration of 100 fs (Figure 2.28). The corresponding average output power is 0.8 W. This is the highest average power reported to date for a femtosecond source in the wavelength range from 2.5 to 5 µm.

2.5.3 Conclusion

With APPLN one can overcome the bandwidth limitations of conventional non-degenerate collinear OPCPA, enabling ultrashort laser pulses in the mid-infrared region. We have successfully demonstrated the possibility to operate an APPLN OPCPA with low noise and high average power. Unlike a PPLN OPA, which would limit the bandwidth, or a noncollinear OPA, which would yield an angularly dispersed idler, our APPLN OPCPA system is able to transfer seed pulses from the well-developed 1.5 µm spectral region to the mid-infrared, while maintaining bandwidth and good spatial beam quality. With a 10-mm-long APPLN chip, we are able to achieve 1.4 W uncompressed idler output power with low OPG background. In a first rough compression experiment, we also managed to obtain 0.8 W of average power with 100 fs output pulses. OPG was suppressed by using a wide pump beam and relatively low-gain amplification stages. We do not yet use the full power of our pump source because of the small pump spot required with our 1-mm clear aperture APPLN crystals. Further power scaling will be possible with wider-aperture devices.

2.6 Outlook: Towards high-field physics in the mid-IR

Future work on the OPCPA system itself will focus on fully exploiting the advantages of our new seed concept introduced in Section 2.5. First, the APPLN devices in the amplification stages will be replaced by more optimized designs. So far, we used the gratings that were originally designed for the old seed concept and do not take into account the slightly different wavelengths interacting in the new approach (3.4 µm output center wavelength instead of 3.6 µm). We will also experiment with lithium tantalate ($LiTaO_3$) instead of lithium niobate as the nonlinear gain material. Lithium tantalate offers higher damage thresholds with the downside of providing lower nonlinearity. It needs to be tested experimentally whether this new material allows efficient operation with lower susceptibility towards photorefractive and thermal effects.

Furthermore, we will work on spectral broadening of the 1.5 µm seed pulses. For this purpose, we will explore continuum generation in reverse-proton-exchanged PPLN waveguides. These devices were shown to be capable of providing octave spanning spectra with nJ input pulses [116]. Alternatively, we will look into traditional con-

tinuum generation in highly nonlinear fibers. Only with a spectrally broadened seed source we will be able to fully exploit the large amplification bandwidths offered by aperiodic quasi-phase-matching.

More work is also needed on the dispersion compensation side of our system. While an improved coarse dispersion management can be achieved by better optimizing our combination of stretcher and compressor, near-perfect compression is expected after the addition of a spatial light modulator for fine dispersion control in the seed path. Our current grating stretcher is already designed to accommodate the liquid crystal mask.

With all these improvements and making full use of our available pump power, we expect to realistically generate 25-to-30-fs pulses (two-cycle pulses) with around 10 to 20 µJ of pulse energy in the mid-infrared. With these parameters we can reach sufficient intensity for most high-field physics applications (of course, still tighter focusing is required than with the more energetic pulses from traditional Ti:sapphire amplifier systems operating at 800 nm wavelength and similar pulse durations).

Another focus of our work will be to actually use this unique source of intense ultrashort pulses for applications. We're exploring its use for multi-dimensional spectroscopy (see e.g., [119] and other work in this special issue). Due to its spectral location, our OPCPA system offers itself for spectroscopy on water. While the high repetition rate would benefit the signal-to-noise ratio, it needs to be seen whether the high average power could be detrimental for some molecular spectroscopy applications [120]. For spectroscopy on water this would not be an issue.

As our own motivation for developing the OPCPA system is in the field of high-field physics, we plan to perform the first experiments in this area. Already with its current performance (8 µJ, 100 fs), high-harmonic generation and strong-field ionization are in reach of the system. More specifically, we plan to investigate strong-field ionization of xenon with a velocity-map imaging spectrometer [121] (Figure 2.29). By strongly focusing our current pulses with short-focal-length aspheric optics we expect to reach $1/e^2$ beam radii of about 7 µm. This will enable peak intensities on the order of 10^{14} W/cm^2. The first goal is to observe strong-field ionization. This will be an immediate proof that our system reaches the required intensities. We will then investigate the structure of the electron spectra at higher energies. There's an ongoing debate whether the otherwise extremely successful tunneling picture of strong-field ionization breaks

down when the ionizing laser field is scaled to long wavelengths (see, e.g., [122-124]). While the tunneling theories predict a single-peaked electron energy distribution, an alternative theoretical approach based on velocity-gauge strong-field approximation predicts a double-humped structure with a pronounced local minimum between the two peaks [124]. This significant qualitative difference between the two predictions should be easy to verify. It is thus well suited as a first experiment with our OPCPA system.
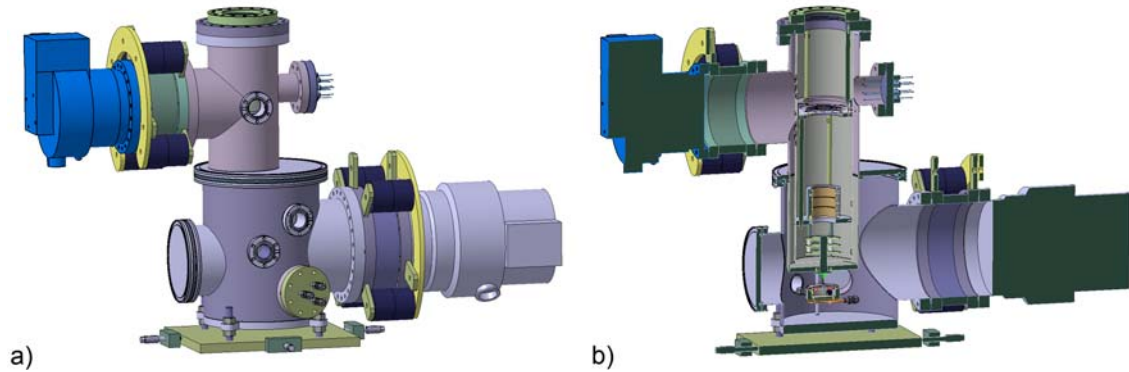
Figure 2.29: Velocity-map imaging spectrometer in our laboratory. a) Outside view. b) Inside view. An electron lens system images the photo-electrons (or –ions) created in the interaction zone onto a micro-channel plate followed by a phosphor screen. The resulting image is recorded by a CCD camera (not shown). The radial impact points of the charged particles can be related to their energy. This spectrometer thus allows recording angularly resolved electron (and ion) spectra.

Chapter 3

Quantum path interferences in high-order harmonic generation

High-order harmonic generation (HHG, [21]) is together with strong-field ionization one of the most fundamental strong-field processes. HHG also forms the basis for current schemes of attosecond pulse generation [125-130]. With amplified femtosecond laser pulses, the electrical field-strength in the beam can easily reach and surpass inner-atomic field strengths. In this regime, the interaction of the light field with the atoms cannot be considered a simple perturbation anymore. HHG is one of the most prominent processes occurring in this non-perturbative regime. The process of HHG can be described semi-classically with the so-called three-step model [24]. It is usually sufficient for a qualitative understanding of many aspects of HHG. The concept behind the three-step model is schematically depicted in Figure 3.1. The strong electric field of the driving laser significantly deforms the Coulomb potential of the atom. In step 1, around a maximum of the laser field, an electron may leave the atom through tunnel ionization. The evolution of the electron after ionization is then treated purely classically with the driving laser field accelerating the electron. Through this acceleration, the electron gains kinetic energy. As the oscillating electric field of the laser changes its sign a quarter period after the maximum, the electron is slowed down and is eventually driven towards its parent ion. With a certain probability, the electron then recombines with the ion in the third step of the process. Upon recombination, the electron releases the excess energy corresponding to the gained kinetic energy plus the ionization energy of the atom in the form of a photon. This photon can be much more energetic than the driving laser photon energy.

| Step 1 | Step 2 | Step 3 |

| tunnel ionization | acceleration in laser field | recombination |
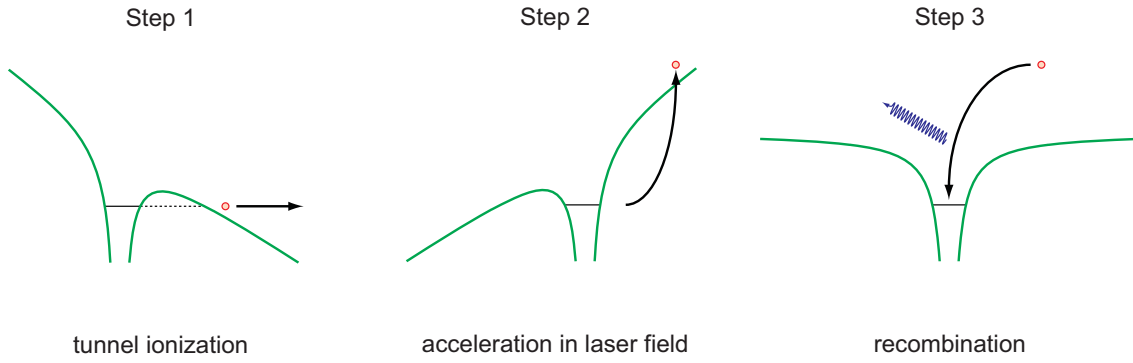
Figure 3.1: Three-step model of HHG. In step 1, the electron is field-ionized from the atom. The electric field of the driving laser pulse accelerates the electron in step 2. Finally, the electron may return to its parent ion and recombines with a certain probability in step 3.

Due to the symmetry of the system, the three-step process described above repeats on every half-cycle of the driving laser field. From this periodicity in the emission of the energetic photons, it directly follows that the spectrum of the generated radiation consists of discrete peaks located at odd integer multiples of the laser photon energy. It lies in the non-perturbative nature of HHG that those peaks may extend to very high integer multiples. The peak photon yield of the perturbative harmonics known from classical nonlinear optics (third harmonic, fifth harmonic, and maybe even seventh harmonic) drops exponentially with increasing harmonic order. It is typical for HHG that around the seventh to ninth harmonic a transition to a plateau of almost constant photon yield takes place. This plateau region can extend over many (even hundreds) harmonic orders before it reaches the cut-off where conversion efficiency drops exponentially towards zero. The location of the cut-off can be estimated using the cut-off law

$$\hbar\omega_{\text{cut-off}} = 3.17 U_p + I_p, \tag{3.1}$$

with $\omega_{\text{cut-off}}$ denoting the cut-off angular frequency, I_p the ionization potential of the HHG medium, and U_p the ponderomotive energy [24, 32]. The ponderomotive energy is given by

$$U_p = e^2 E_0^2 / (4 m_e \omega^2). \tag{3.2}$$

Here, e is the electron charge, E_0 the laser electric field amplitude, and m_e the electron mass. One can see that the higher the laser intensity, the higher the cut-off. The maximum useful intensity is however limited to well below the intensity at which the

tunneling barrier is completely suppressed. This is not the only limiting effect. How-ever, a detailed discussion of limiting effects to HHG yield is beyond the scope of this Chapter. It can also be seen from the above equation that at constant intensity, a longer driving laser wavelength can further extend the cut-off.
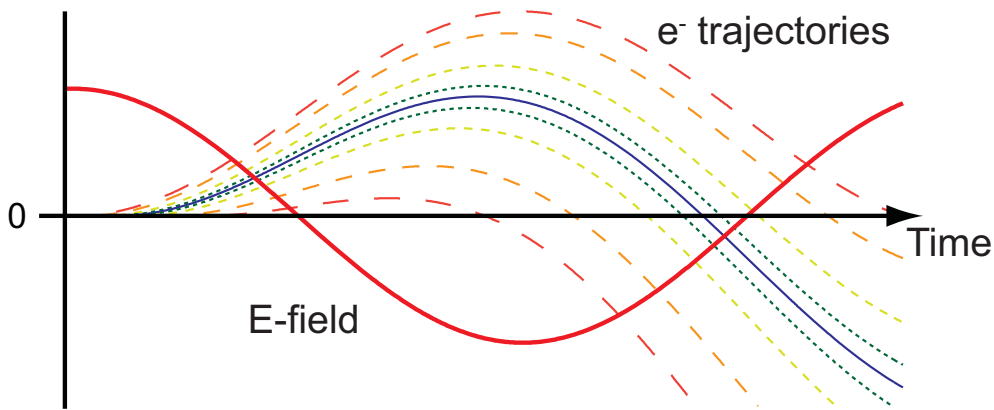
Figure 3.2: Classical trajectories of electrons (thin lines) released from the atom and accel-erated in the electric field of the driving pulse (thick solid red line). The trajectory an elec-tron takes depends on the electron release time with respect to the electric field. Recombi-nation with the parent ion can take place at zero-crossings. The kinetic energy at recombi-nation is highest for the cut-off trajectory (blue solid line). The length and color of the dashes visualizes the recombination energy of the other trajectories: longer dashes, redder color represent lower energy. Electrons released during the first half of the half-cycle (not shown) cannot return to the parent ion and thus do not contribute to HHG.

When looking at the classical trajectories of the electrons in the external elec-tric field of the driving laser pulse, one finds that electrons released between the zero-crossing and maximum amplitude of the field never return to the parent ion. Those elec-trons do not contribute to HHG. Electrons freed between the field maximum and its next zero-crossing, however, return to the parent ion and may recombine. Examples for such classical trajectories are shown in Figure 3.2. The actual trajectory and the energy gained by the electron depend on its release time. For each energy value below the cut-off two corresponding trajectories are found: a long trajectory for which the electron was freed close to the field maximum and a short trajectory with a later electron release time. This can be easily understood in the simple picture of the three-step model: The long trajectory electrons are those that already passed their point of maximum kinetic energy but now have to travel "uphill" against the combined laser and atomic potential before they may recombine. The short trajectory electrons, on the other hand, are still in

their "downhill" acceleration phase when they recombine. Through both pathways, the same final energies can be reached.

Figure 3.2 also clearly illustrates that the total harmonic emission from the short family of trajectories possesses an up-chirp in time, while the emission from the long trajectories is down-chirped. These findings obtained from the purely classical picture are in excellent qualitative agreement with quantum mechanical models. It should also be noted that there exist also higher-order trajectories that take more time to recombine than a single laser oscillation cycle (i.e., they pass the ion core at least once without recombining). The recombination probability for these higher-order trajectories is very low due to electron wavepacket diffusion. Therefore they usually do not play an important role in practice.

Most commonly, HHG is performed in a gas jet. The three-step model and the rest of the above discussion only take into account how a single atom responds to the strong laser field. In a gas jet, however, the beam interacts with an ensemble of atoms. The high-order harmonic light observed after the generation medium is thus a coherent superposition of the microscopic response of the individual atoms. A significant amount of harmonic light can be observed macroscopically only if the contributions from the individual microscopic emitters add up constructively. For efficient HHG, one therefore needs to ensure phase-matching. A review of macroscopic aspects of HHG is given by Gaarde et al. [131]. Phase-matching is strongly trajectory dependent [132-134]. This allows phase-matching of only the short trajectory by placing the focus of the driving laser beam in front of the gas jet used for HHG.

The long and short trajectories leading to the same final harmonic photon energy start from the same initial state and end in the same final state. Furthermore, the entire process is coherently driven by the incident infrared laser. As a result, one expects interference to occur between the long and the short trajectory emission. It is, however, not obvious how and whether such interference manifests itself in the macroscopic high-order harmonic beam. Can experimental conditions be found that both trajectories contribute with comparable strength to the macroscopic signal?

In the following we present theoretical and experimental evidence for what we think is the first observation of quantum-path interference (QPI) between long and short trajectory contributions in HHG. In Section 3.1, we report the first experimental manifestation of this interference structure and discuss the experimental conditions that

festation of this interference structure and discuss the experimental conditions that were necessary to succeed. We will show in Section 3.2 that these conditions are universal and can be transferred to other gas species. We will then generalize the experimental configuration, which enabled us to record interferences in spatio-spectral domain (Section 3.3). With Section 3.4 we end this Chapter by critically assessing all the evidence and potential alternative explanations for the observed structures.

Results presented in this Chapter have appeared in scientific journal publications [135-138].

3.1   First observation of quantum path interferences in HHG

High-order harmonic generation (HHG), leading to the production of extreme ultraviolet (XUV) emission by interaction of an intense laser field with an atomic or molecular target, has become intensely studied [139], in particular for the generation of isolated [126-130] as well as trains [125, 140] of attosecond pulses.

The underlying physics is well described by the semi-classical three-step model introduced above [24, 141]. In this model, an electron initially in the ground state is freed into the continuum by tunnel ionization, accelerated and ultimately driven back to the core by the oscillating linearly polarized laser field. At the core it may recombine and emit a high-energy harmonic photon.

A quantum-mechanical theory has been developed within the strong-field approximation (SFA) [142]. Similar to the Feynman's path integral approach, the harmonic dipole moment can be written as the sum over different quantum path contributions to the XUV emission [25]. These quantum paths are a generalization of the classical electron trajectories described above.

3.1.1   Conditions for the observation of interferences

The phase $\phi_q^{(j)}$ associated to each quantum path (j) of harmonic order q is given by the classical action along the corresponding trajectory, and can be approximated by the product of the ponderomotive energy U_p with the electron excursion time $\tau_q^{(j)}$:

$$\phi_q^{(j)} \approx -U_p \tau_q^{(j)} \approx -\alpha_q^{(j)} I \,, \qquad\qquad (3.3)$$

where I is the laser pulse intensity and $\alpha_q^{(j)}$ is roughly proportional to $\tau_q^{(j)}$. An introduction of the concept of the "alpha-values" or reciprocal intensities $\alpha_q^{(j)}$ can be found in Ref. [134]. The longer the trajectory, the longer the excursion time, the larger the corresponding alpha value and, thus, the stronger the intensity dependence of the associated dipole phase. The relative phase between the different trajectories leads to interference in the total single-atom dipole moment. This generic behavior is illustrated in Figure 3.3 for harmonic 15 generated in argon (solid black curve). The calculated dipole strength exhibits fast oscillations with increasing intensity when the harmonic is in the plateau region, where many quantum paths contribute to the emission. At low intensity when the harmonic enters the cutoff, the interferences disappear due to only a single quantum path contributing.

When the harmonic dipole is restricted to the two main quantum paths, i.e. the two shortest orbits, referred to as the short ($\tau_q^{(1)} < 0.65 \cdot T$, $\alpha_q^{(1)} \approx 1 - 5 \cdot 10^{-14}$ rad·cm^2/W with T denoting the laser oscillation period) and long ($0.65 \cdot T < \tau_q^{(2)} < T$, $\alpha_q^{(2)} \approx 20 - 25 \cdot 10^{-14}$ rad·cm^2/W) trajectories [143], regular oscillations are observed (red curve in Figure 3.3) with an average period of 0.3×10^{14} W/cm^2 close to the expected $2\pi / \Delta\alpha$ interference period of the two first quantum paths (first order QPI – as opposed to higher-order QPI, which is interference involving at least one higher order trajectory).

These fast oscillations are smoothed out if integrated over laser intensities varying by only a small amount on the order of $2\pi / \Delta\alpha$. In the experimental conditions of a gas jet positioned in the focus of an ultrashort laser beam, the averaging over the spatial and temporal intensity profile will smear out these oscillations in the macroscopic response (dotted curve in Figure 3.3). Indeed only monotonic, unmodulated distributions have been measured up to now despite extensive measurements in different experimental conditions [144] [145]. While the contributions from the two main quan-

tum paths have been independently characterized experimentally (see, e.g., [146-149]), their relative phase is still unknown since no direct observation of their interference has been reported so far.
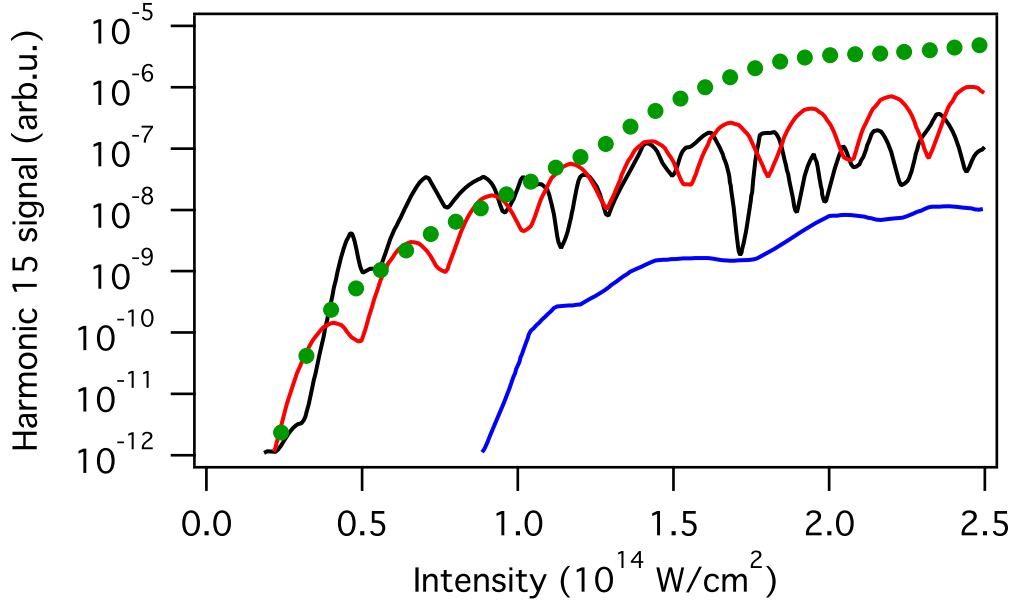
Figure 3.3: Calculated signal of the 15th harmonic in argon. The single-atom dipole strength including all quantum paths (black solid curve) is compared to the same quantity in the case when only the two shortest trajectories are considered (red solid curve). The green dots represent the macroscopic response with no spatial filtering, whereas the blue solid line is the macroscopic harmonic signal with off-axis spatial filtering between 14 and 20 mrad in the far-field. (Simulations by T. Auguste)

In the following, we will show that we can theoretically define, and experimentally find, conditions where the QPI are directly observable. In order to avoid temporal averaging, we perform spectral filtering, whilst spatial averaging is partly avoided through far-field spatial filtering. The latter also allows one to balance the weight of the two quantum-path contributions to increase the interference contrast. The measured contrast is high enough to resolve the QPI over all the generated plateau harmonics. This gives access to the relative phase of the quantum paths that is needed to reconstruct the single atom dipole moment and get insight into the ultrafast electronic dynamics in the emission process. Moreover, by slightly changing the laser intensity, we demonstrate control of these paths on an attosecond timescale. Indeed, only tiny changes (of a few 10 as) of the electron trajectories are enough to shift their relative phase by π.

Let us first consider temporal averaging effects due to the pulse envelope. We can get around them by using the temporal variation of the dipole phase that induces a chirp of the harmonic emission through a phase modulation process [132, 150-152]:

$$\Delta\omega(t) = \frac{\partial\phi_q^{(j)}(t)}{\partial t} = \alpha_q^{(j)} \times \frac{\partial I(t)}{\partial t}.$$

(3.4)

This chirp, and thus the harmonic spectral bandwidth, increases with laser intensity. However, if one considers the signal precisely at the harmonic central frequency, it always corresponds *in time* to the maximum of the laser temporal envelope, while the emission from the envelope edges is shifted to different side frequencies (i.e., the harmonic chirp effectively maps time to frequency $\Delta\omega = \omega - \omega_q$).
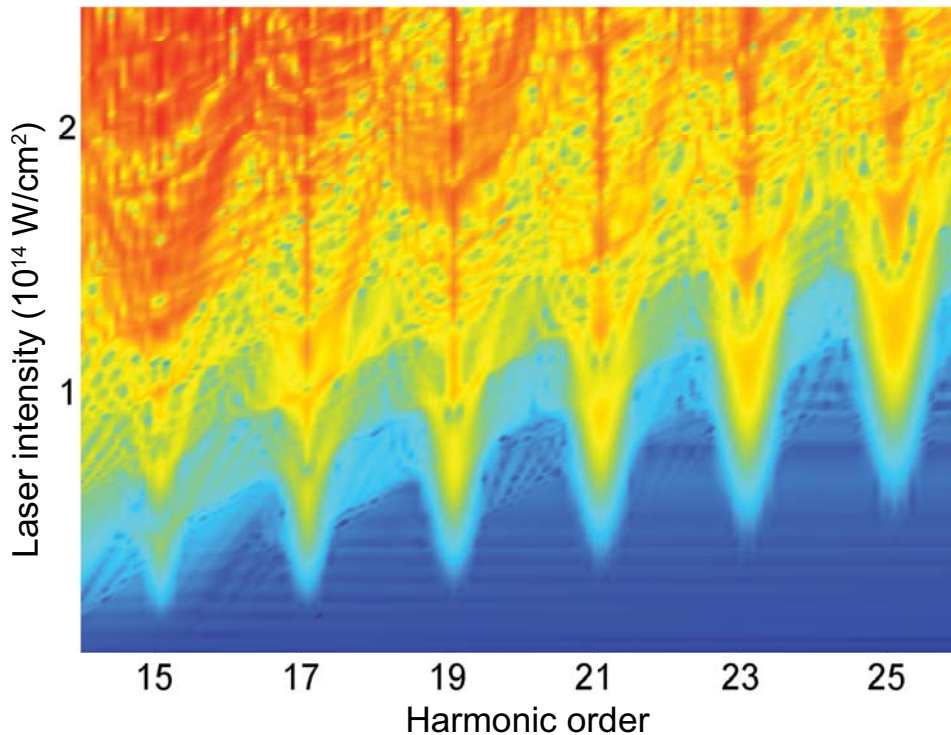
Figure 3.4: Harmonic spectra as a function of peak lasers intensity for a single argon atom and 30 fs input pulse duration. (Simulations by A. Zaïr)

By spectrally resolving the harmonic, we thus get rid of the temporal averaging. Even if the chirp is larger for the long trajectory contribution than for the short one,

the spectral bandwidth where the two contributions overlap is generally large enough to allow detection of harmonic yield modulations. This is illustrated in Figure 3.4, which shows the single-atom harmonic spectrum for argon as a function of peak laser intensity. These simulations were performed in the strong-field approximation (SFA, [142]) for a 30 fs (FWHM) Gaussian laser pulse at 800 nm center wavelength. At each harmonic central frequency, the photon yield is modulated as a function of the peak laser intensity due to first order QPI and the harmonic spectral width increases as expected. On either side of the central harmonic frequency, a parabolic shape of the harmonic spectral distribution is visible. The long trajectory typically dominates the HHG process in this region but also a few percent of the short trajectory still contribute and may induce a fringe pattern with a low contrast. Some additional fine structure is also visible in this region, especially for low order harmonics; this is attributed to higher-order QPI and phase modulation effects.

We also performed simulations based on the solution of the time dependent Schrödinger equation (TDSE) in the single active electron approximation, using a model atomic potential [153]. The results confirm our observations and highlight the robustness of the interference effects.

Let us now consider the spatial averaging effects. The averaging effect along the laser propagation direction can be reduced by using a generating medium shorter than the laser confocal parameter. As for the transverse averaging, we may use the spatial analog of the temporal/spectral filtering. The intensity dependence of the dipole phase leads via the Gaussian transverse profile of the laser beam to a curvature of the harmonic phase front (equivalent to a spatial chirp) [132, 151, 152, 154]: the (near-field) distribution at the exit of the medium is "projected" into the far field so that a far-field spatial selection can prevent transverse spatial averaging. Note that the long trajectory contribution has a larger beam divergence than the short one.

However, an additional difficulty arises here due to different phase-matching of the two quantum paths [133]. We obviously need generating conditions where both paths give significant contributions to the macroscopic response. This implies focusing the laser after the generating medium. In this situation, the short path is phase-matched on-axis, and the long path off-axis. This results in a concentration of the short (long) path contribution at the center (outskirts) of the far-field profile. The relative contribution of the two trajectories thus varies radially. There is an optimum position off-axis

where the QPI fringe contrast will be maximum. A far-field spatial filter positioned at this optimum divergence angle will select this region and in addition limit the spatial averaging.

The importance of this spatial selection for the QPI observation is demonstrated by simulations of the full macroscopic response using the SFA dipole and a three-dimensional propagation code that solves the propagation equations for the laser and harmonic fields in the paraxial and adiabatic approximations. The generating conditions are the following: a 30-fs laser pulse is focused 3 mm after a 1-mm long argon gas jet. Its pressure amounts to 10 Torr. The confocal parameter of input beam is $b = 12$ mm. The harmonic spectrum was calculated after propagation of the generated harmonic electric field to the far field region where we applied spatial filtering along one dimension: a 6 mrad wide integration window centered at a divergence of 17 mrad off axis.
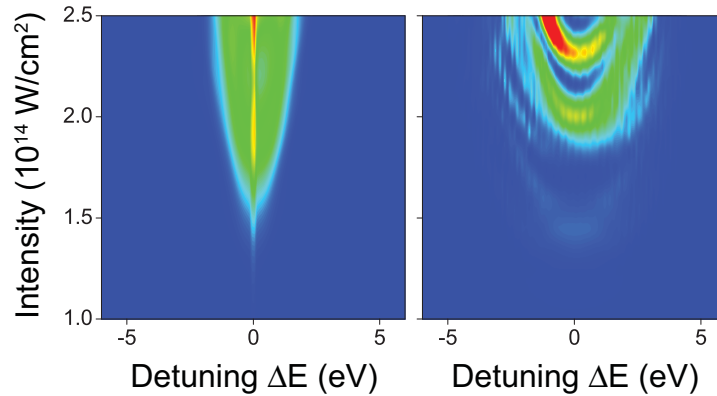
Figure 3.5: Calculated macroscopic spectra of the 15th harmonic argon as a function of peak laser intensity without (left) and with (right) a far-field off-axis window of 6 mrad width. The harmonic signal is plotted with a linear color scale defined as blue at zero strength to red at maximum strength (10^{10} without window and $4.5 \cdot 10^7$ with window). (Simulations by T. Auguste)

Figure 3.5 shows the simulation results for harmonic 15 as a function of the peak laser intensity with and without the spatial selection. In the latter case (left curve), the integration is performed over the total spatial profile, but the main contribution comes from the 6-mrad central part, mostly because of the strong short-trajectory contributions in this area. The spatial averaging results in blurring of the QPI and therefore the harmonic amplitude is not modulated, but the spectral width still increases with the

peak laser intensity as expected. In contrast, when the far-field filtering is performed (right curve), the harmonic spectrum reveals a clear parabolic shape similar to those observed in the single-atom response in Figure 3.4. The contrast of the fringes is maximum at the harmonic central frequency ($\Delta E = \hbar \Delta \omega = 0$), as expected for the first-order QPI. The fringes are shifted to higher peak laser intensity when $|\Delta E|$ increases because these frequencies are generated on the edges of the temporal envelope of the input laser pulse and thus correspond to a smaller effective intensity. This could explain the parabolic shape of the QPI. We have observed a similar behavior for all plateau harmonics. The fine structures visible in the SFA single-atom response corresponding to high-order QPI and phase modulation are here smoothed out by the macroscopic response. Note finally that the harmonic signal is reduced by one to two orders of magnitude when the spatial selection is performed, which makes the experimental observation of QPI challenging.

3.1.2   Experiments

In the experiments, we used a Ti:sapphire laser system delivering 30-fs, 800-nm pulses at a repetition rate of 1 kHz with a maximum pulse energy of 1.5 mJ. The laser beam is focused by a spherical mirror with 50 cm radius of curvature (ROC) into a pulsed argon jet. A half-wave plate and a polarizer are placed in the IR beam to precisely and continuously control the peak intensity in the jet from $0.5 \cdot 10^{14}$ W/cm^2 to $4.5 \cdot 10^{14}$ W/cm^2. The high-harmonic emission is reflected by a spherical gold mirror (ROC=30 m) under grazing incidence at the entrance of a spectrometer composed of a platinum grating and a backside-illuminated CCD. The gold mirror can be transversally moved to spatially select a part of the beam, acting as a spatial window with an acceptance angle of 6 mrad that can be moved from perfect on-axis alignment to an off-axis position. The gas jet is positioned 3 mm before the laser focus to phase-match both quantum paths. The acquisition of each harmonic spectrum is performed over 5000 laser shots. High pulse energy stability of the laser is thus required to ensure that QPI is not smeared out due to intensity fluctuations.
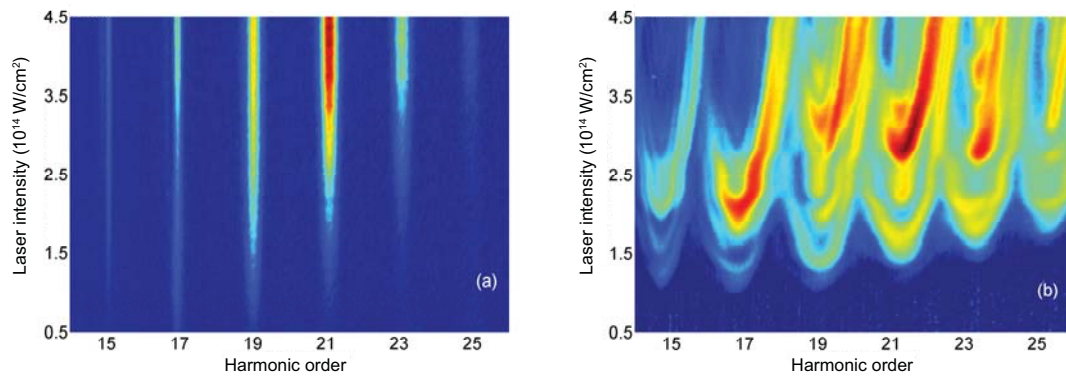
Figure 3.6: Measured harmonic spectra as a function of laser peak intensity with far-field 6-mrad spatial filtering. a) filter positioned on-axis; b) filter positioned off-axis.

Figure 3.6 shows the harmonic spectra acquired as a function of laser peak intensity. In Figure 3.6a), on-axis spatial selection is performed, such that the short trajectory contribution dominates. As expected, the harmonics are spectrally narrow and their amplitudes saturate monotonically with laser intensity. Very similar spectra are obtained when the jet is positioned 3 mm after the focus, in a condition where only the short quantum path is phase-matched. In Figure 3.6b), an off-axis section of the harmonic beam is selected. Due to the filtering, the harmonic signal is reduced by one order of magnitude. A clear broadening of the plateau harmonics (from order 13 to 25) is visible, consistent with the long trajectory contribution as observed in [148]. At a sufficiently high intensity, neighboring harmonics start to overlap. If the laser carrier-envelope offset phase (CEP, [99, 155, 156]) would be stabilized, one would observe interferences between overlapping long-path contributions from both harmonic orders generated at different instants within the laser envelope [147]. In our experiments, the CEP was random so that these interferences were blurred out and did not perturb the observation of the first order "intra-harmonic" QPI. The latter does not depend on the laser CEP since it occurs on a subcycle, attosecond time scale.

The amplitudes of the plateau-harmonics are clearly modulated as a function of laser peak intensity. The parabolic structures observed in the calculation are clearly visible in the experimental data and the fringe periodicity ($\sim 0.3 \cdot 10^{14}\,\mathrm{W/cm^2}$ at the harmonic central frequency) coincides with the calculated value for the first order QPI. Other possible sources of spectral distortions cannot explain the observed behavior. Ionization starts to play a role around $2.5 \cdot 10^{14}\,\mathrm{W/cm^2}$ (argon saturation intensity) and

induces an asymmetry in the calculated and measured spectra at high intensity. Changes in phase-matching may also occur with increased intensity, but they are not expected at lower intensities where the parabolic shapes first appear. Finally, the strong phase modulation of the long trajectory may alone produce spectral interferences due to the emission of the same frequency at two different instants of the laser temporal intensity profile (in close analogy to self-phase modulation known from traditional nonlinear optics). However, in this case, the spectrally integrated harmonic signal (integrated over a single harmonic) would not show any modulation upon varying the laser peak intensity because phase modulation only spectrally redistributes the energy. This is in contrast to our measured and simulated spectra, as is shown in Figure 3.3 where the spectrally-integrated but spatially-filtered signal of harmonic 15 still exhibits modulations (blue curve), though with a reduced contrast due to the remaining temporal averaging (averaging over the pulse envelope). The spectral interference structures induced by phase modulation do not occur at the exact harmonic frequency since emission at this frequency happens at a single instant in time – the peak of the temporal pulse profile. Phase modulation can therefore be ruled out completely as a possible explanation of the modulations observed at the center harmonic frequencies.

3.1.3   Conclusion

In conclusion, the above experimental data represents the first observation of the interference between the two shortest quantum paths contributing to the high-order harmonic emission. Spectral and far-field spatial filtering allow us to minimize the temporal and spatial averaging that otherwise blurs out the interference in the macroscopic response. This interference is not CEP sensitive since it occurs on the subcycle timescale of the quantum paths. By varying the laser intensity, we change their relative phase and thus demonstrate a control of the paths on an attosecond time scale. Indeed, at $1.5 \cdot 10^{14} \, \text{W/cm}^2$, a 10% variation of the intensity shifts the QPI from constructive to destructive interference for harmonic 15. Saddle-point calculations show that the corresponding variations in excursion times are extremely small for both quantum paths: $\Delta \tau_{15}^{(1)} = -22 \, \text{as}$ and $\Delta \tau_{15}^{(2)} = +13 \, \text{as}$. The resulting attosecond emission is shifted in time by similar amounts, demonstrating the possibility for unprecedented accuracy in the control of attosecond pulses.

Our experiment is also a first step towards the direct measurement of the full single-atom dipole. Longer quantum paths are predicted by the SFA and TDSE calculations and their interferences appear as fine structure in the single-atom harmonic spectra. These higher order QPIs may become observable in the macroscopic response by means of our detection technique, in particular in Neon or Helium, when several higher-order trajectories could contribute significantly to the HHG process [157] while ionization effects will be limited. Finally, the high sensitivity of our interferometric technique will be particularly useful for the investigation of trajectory behavior in HHG taking place in more complex systems such as molecules or clusters.

3.2   Signatures of ionization effects in quantum-path interferences

In the following, we show that quantum path interferences (QPI) are indeed an intrinsic phenomenon of HHG and can be observed for various generation media. We compare results obtained in xenon, argon, and neon and investigate how the different ionization potentials of these gases affect the appearance of QPI, both experimentally and theoretically. This comparison also demonstrates that the conditions defined for the observation of QPI (see Subsection 3.1.1) are indeed universal and can be transferred to different gas species. In the experiments reported here, we put the main emphasis on investigating how QPI scale to different generation media and what role ionization effects play for the observed interference structures. Ionization effects affect the single-atom response of the medium via ground-state depletion and the macroscopic harmonic emission via free electron dispersion and phase matching.

3.2.1   Impact of different ionization potentials on QPI

In the following, we present both experimental and theoretical results obtained in different rare gases. The generation conditions are the same as those described in Subsection 3.1.2 and only briefly summarize them here. Laser pulses with a center wavelength of 800 nm and a duration of 30 fs are sent through an iris aperture and focused by a spherical mirror into a pulsed gas jet. The radius of curvature (ROC) of the focusing mirror was 50 cm for the case of argon and xenon, and 25 cm for the case of neon. A

half-wave plate and a polarizer control finely the energy of the laser pulses. The jet is movable along the propagation direction to control phase matching conditions. The emitted harmonic radiation is refocused by a spherical gold mirror (ROC = 30 m) in grazing incidence. This mirror is movable perpendicular to the propagation direction for lateral windowing (i.e., spatial filtering) of the beam. The refocused harmonics pass an aluminum filter (150 nm thickness) and hit the entrance slit of an XUV spectrometer consisting of a reflective grating and a XUV CCD.

For the theoretical results presented, we simulate the full macroscopic response as measured in the experiments using the strong-field approximation (SFA) dipole and a three-dimensional propagation code that solves the propagation equations for the laser and harmonic fields in the paraxial and adiabatic approximations.

A generic behavior with respect to the phase matching conditions, independent of the ionization potential of the generating medium, is observed. When selecting the short trajectory (jet after the laser focus), we observe spectrally narrow harmonics as a result of the small frequency chirp of the short trajectory. Their amplitude increases monotonically with the laser intensity since in this case only one trajectory is detected. With the experimental setup described above, we can filter out transverse sections of the emitted beam in its far field distribution. Changing the far field spatial selection from on-axis to off-axis with phase matching optimized for the short trajectory only affects the overall detected harmonic yield, reducing it by roughly one order of magnitude.

In contrast to the previous situation, both trajectories are phase-matched for a jet placed before the laser focus. For an on-axis spatial selection in the far field, the harmonic signal is still spectrally narrow because stronger on-axis emission from the short trajectory with its lower divergence is detected. When selecting the off-axis portions of the beam, a clear broadening of the plateau harmonic spectral width with increasing laser intensity is observed. This is the typical signature of the long trajectory resulting from its larger intrinsic chirp. When properly balancing the relative contributions from the short and the long trajectories by adjusting the position of the far-field spatial filter, interference contrast is maximized and a clear modulation of the harmonic yield with laser intensity occurs. This interpretation is further supported by the fact that in the cutoff region we neither observe significant broadening nor any modulations since only one quantum path exists.
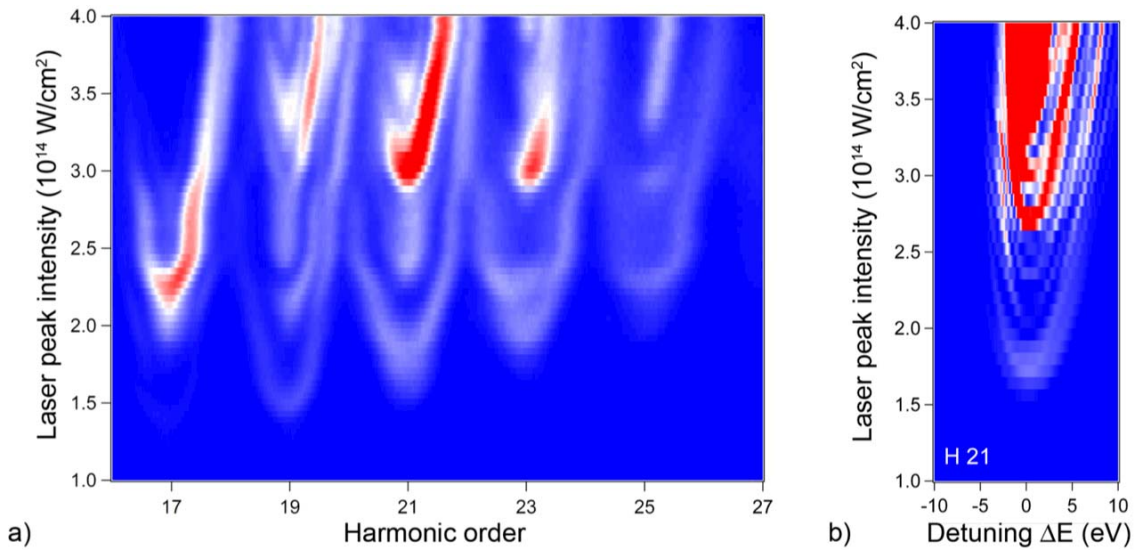
Figure 3.7: Harmonic spectra generated in argon versus laser peak intensity with short and long trajectory phase-matched and off-axis spatial selection: a) measured spectra, b) simulated spectra around harmonic 21. (Simulations by T. Auguste)

The harmonic spectra measured in argon in the optimized conditions for QPI observation are shown in Figure 3.7. The intensity for barrier suppression in argon (ionization potential 15.8 eV) is $2.5 \cdot 10^{14}$ W/cm^2. Below this intensity, we observe several modulation periods attributable to QPI. For higher intensities, the onset of ionization effects results in both an asymmetric shape of the different harmonic orders and a much weaker modulation of the on-axis harmonic signal. These trends are reproduced in our simulations, in particular for harmonic 21 shown in Figure 3.7b). For the calculations, a 6 mrad wide far-field integration window centered 17 mrad off-axis was used. The experimentally measured average modulation periodicity of $\sim 3 \cdot 10^{13}$ W/cm^2 is consistent with our simulations indicating that the modulations are caused by first order QPI (see also Section 3.1, [135]).

Different particle densities in the interaction region do not affect the described spectral behavior significantly in our measurements as well as in our simulations. Especially the modulation periodicity remains unchanged, indicating that dispersion does not play a dominant role for the harmonic yield modulations. However, closer inspection reveals subtle changes in the fine structure of the fringes when the pressure is increased. This is illustrated in Figure 3.8 showing simulations for harmonic 15 of argon for gas pressures of 1 and 10 Torr. While the modulations at the harmonic central frequency are

rather robust, the fine details within the fringe structure are pressure dependent in particular on the blue side and at high intensities. An apparent splitting of the fringes can be observed at 10 Torr for intensities between $2.5 \cdot 10^{14}$ W/cm^2 and $3 \cdot 10^{14}$ W/cm^2. Since this splitting appears only for the high-pressure scenario and above the barrier suppression intensity, it can clearly be attributed to macroscopic nonlinear optical effects.
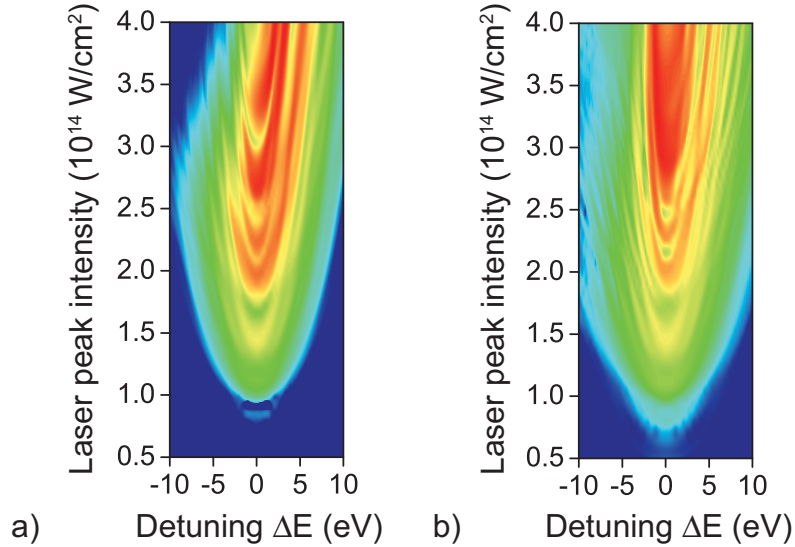
Figure 3.8: QPI dependence on pressure calculated for H15. a) P = 1 Torr. b) P = 10 Torr. The harmonic intensity is plotted on a logarithmic scale normalized for each plot to the maximum signal. (Simulations by T. Auguste)

We further analyzed the origin of the different fringe structures with detailed simulations. Figure 3.9 shows the result of the full model compared to simulations with either all ionization effects switched off or only the single-atom level ionization effects included. The latter case thus includes the medium depletion but does not take into account the macroscopic effects of free-electron dispersion. The simulations show that the asymmetry of the harmonic spectrum at high intensity results from ground state depletion, which is a single atom effect. The harmonic signal on the red side of the spectrum is reduced because on the trailing edge of the generating laser pulse the medium is already depleted. The asymmetry of the harmonic spectrum is thus a direct result of the time-to-frequency mapping caused by the harmonic chirp. The simulated data in Figure 3.9 also reveal that the apparent fringe splitting on the blue side of the harmonic line and other distortions of the fringe structure are a direct consequence of free-electron

dispersion. These free electrons are created on the leading edge of the pulse for intensities beyond barrier suppression. Since the free electrons are concentrated on the beam axis, it is expected that they affect the emission from the short trajectory more strongly than from the long trajectory due to their different phase-matching properties [25, 131, 151]. Interference in the far field between contributions from the short and long trajectory originating from different transverse locations in the medium explains the observed distortions in their relative phase.
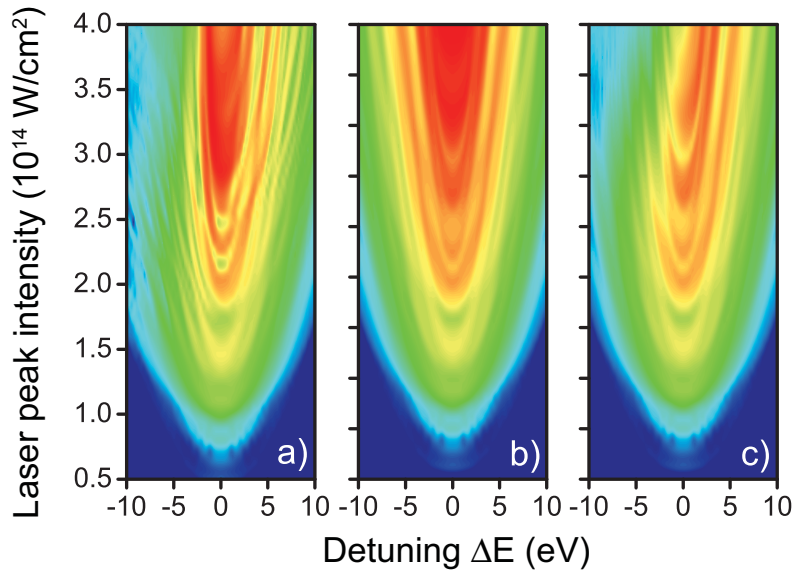
Figure 3.9: Simulated QPI for H15 in argon at a pressure of 10 Torr. a) full simulation, b) ionization switched off, c) with depletion, but free electron dispersion switched off. (Simulations by T. Auguste)

Xenon with its lower ionization potential of 12.1 eV shows saturation effects at lower intensities than in argon. The intensity for barrier suppression is $8.7 \cdot 10^{13}\,\text{W/cm}^2$. Above this intensity, the harmonic yield saturates and the effective driver pulse duration contributing to the harmonic emission gets shorter with increasing laser intensity due to the fast medium ionization. Only the leading part of the pulse generates harmonics, resulting in a strong asymmetry of the harmonic spectra. Meanwhile, the harmonic chirp increases further, which leads to asymmetric broadening on the blue side only (Figure 3.10).
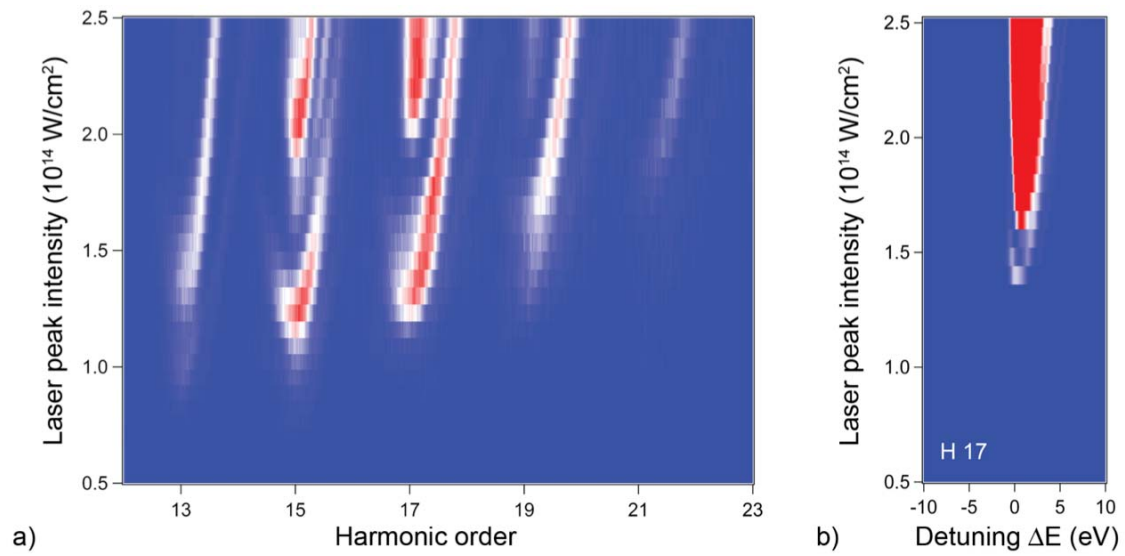
Figure 3.10: QPI in xenon. a) Measured harmonic spectra generated in xenon versus laser peak intensity. b) Simulated spectrum for harmonic order 17. (Simulations by T. Auguste)
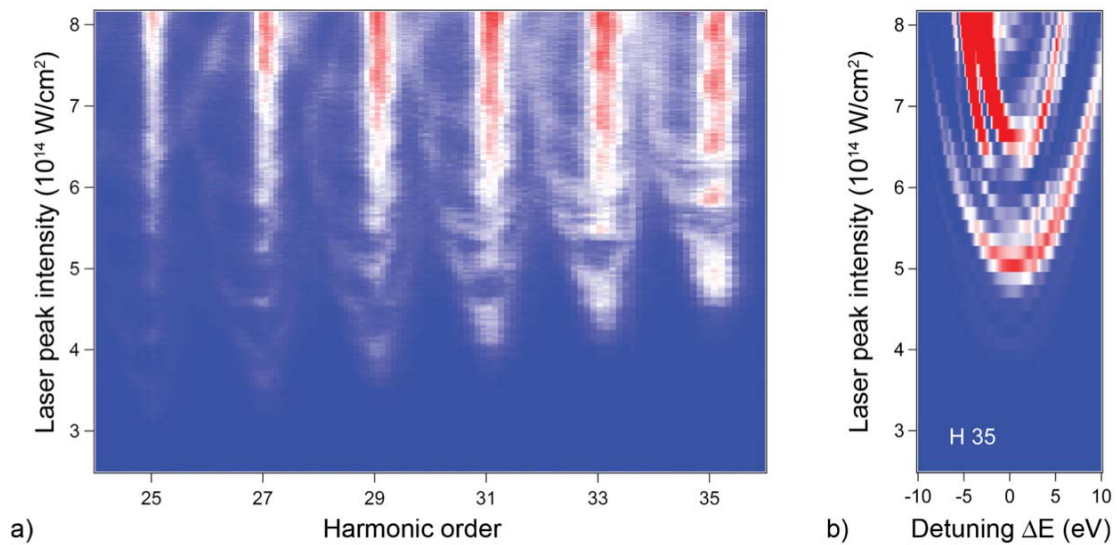
Figure 3.11: QPI in neon. a) Experimental harmonic spectra generated in neon with respect to the laser peak intensity: over the full range of accessible intensities located below ionization threshold neither a blue shift nor a saturation of the harmonic signal at the harmonic central frequency is observed. b) Simulated spectrum for harmonic order 35. (Simulations by T. Auguste)

In the case of neon, the high ionization potential of 21.6 eV leads to a saturation intensity, which is approximately one order of magnitude higher than in the case of xenon. Therefore it is possible to generate high harmonics efficiently well below the

saturation intensity, opening the way to study the QPI over a wide range of intensities without being limited by ionization. As expected, the data displayed in Figure 3.11 shows no sign of blue shift. Within the range of covered intensities, we are able to clearly identify about five modulation periods of the harmonic yield with an average periodicity of $\sim 8 \cdot 10^{13} \, \text{W/cm}^2$.

3.2.2   Conclusion

The presented data show that experimental and theoretical conditions can be found allowing for the observation of quantum-path interferences in high-harmonic generation independent of the harmonic generating medium. This is made possible through proper spectral and spatial filtering. The filtering prevents spatial and temporal variations of the interference conditions from smearing out the fringes. We discussed the influence of the generation medium, and more specifically ionization effects, on the observed interference structures. The comparison of measurements taken in different gases allowed us to study the behavior of QPI with laser intensities above, around and below the ionization threshold. Depending on this regime, the plateau harmonics exhibit intensity-dependent features such as saturation of the harmonic yield, spectral blue shift, and trajectory dependent spectral broadening. The measurements are well supported through simulations. Our method provides the possibility of investigating this behavior in more complex systems such as molecules or clusters. Recent experiments have shown that in small molecules, such as CO_2, N_2, H_2, D_2, the continuum dynamics of the electron wavepacket (which is at the origin of QPI) is similar to that of atoms, at least for the short trajectories [14, 158]. One can thus expect that QPI will be observable in these systems and that its interferometric sensitivity will reveal differences between the molecular and the atomic continua. Our method is a general, robust tool to collect information directly in the spectral domain of the harmonic generation process including its temporal dynamics under varying experimental conditions.

3.3   Spatial fingerprint of quantum-path interferences

In Section 3.1, we reported the first observation of the intensity dependence of the QPI by properly selecting phase matching and spatial filtering conditions [135]. In follow-up experiments performed in different gases and discussed in Section 3.2, we investigated

the influence of ionization effects on the observed interference patterns and could identify the signatures of microscopic and macroscopic processes [136]. Here, we extend our studies to the spatial domain and report the first observation of spatially and spectrally resolved QPI as a function of intensity. Our experimental setup gives both, spectral resolution along one transverse axis of the harmonic beam and spatial resolution along the orthogonal transverse direction. We therefore gain access to both, the spatial fingerprint of the QPI and the intensity-dependent spectral QPI structures studied in our previous experiments. A theoretical model based on the strong-field approximation (SFA) and including propagation reproduces the experimental data very well and aids its interpretation [25, 143].

Theoretical and experimental analysis show that the two shortest electron quantum paths give the main contributions to the harmonic emission, referred to as "short" and "long" trajectories according to their excursion time. This is the result of both, the three-step process occurring on a single-atom level and the macroscopic effect of phase matching [133, 134, 151]. Both trajectories contribute macroscopically when the generation medium is placed before the laser focus. The emission resulting from the short trajectory presents a small beam divergence while the contribution of the long trajectory, mainly emitted off-axis, exhibits a larger divergence. Because the relative phase between the interfering high harmonic contributions depends on intensity, we expect a spatial structure for the QPI resulting from the beam profile of the driving laser. With spatially resolved HHG we have fully resolved this spatial interference structure, and followed its alteration as a function of the laser peak intensity.

3.3.1   Theory

In the following, we briefly summarize the QPI theory with respect to their spatial properties. A more detailed discussion of QPI theory can be found Section 3.1 and in References [135] and [137].

The occurrence of an interference pattern between contributions of different quantum paths can be explained as follows: The phase $\phi_q^{(j)}$ of the quantum path j contributing to harmonic order q is approximately proportional to the ponderomotive potential U_p times the electron excursion time $\tau_q^{(j)}$,

$$\phi_q^{(j)}\left(r,t\right) \approx -U_p\tau_q^{(j)} \approx -\alpha_q^{(j)}(I(r,t))\cdot I(r,t) \approx -\alpha_q^{(j)}(I)I_0\exp\frac{-2r^2}{w^2}\exp\frac{-2t^2}{\tau^2}\,, \tag{3.5}$$

where the laser beam has a peak intensity of I_0, a spatial size of w and a temporal width of τ.

In the plateau region, $\alpha_q^{(j)}$ is a slowly varying function of the laser intensity I [134]. Since $\alpha_q^{(2)} > \alpha_q^{(1)} > 0$, the phase associated to the long path (characterized by a long excursion time, $j=2$) varies much more rapidly than that of the short path (characterized by a short electron excursion time, $j=1$). This leads to a complicated interference pattern in space and time during the HHG process. However, it is possible to understand the qualitative signature of QPI in space and time by disentangling the two dimensions as follows.

In the spatial domain, the radial variation of the laser intensity leads to a spatial dependence of the harmonic phase difference $\Delta\phi_q\left(r\right) = \phi_q^{(1)} - \phi_q^{(2)} \approx \Delta\alpha_q I(r)$, which results in modulations of the harmonic yield along the spatial coordinate through interference. Another way of looking at this is to consider that Equation (3.5) results in a phase front curvature of the harmonic beam that depends on the trajectory:

$$\phi_q^{(j)}(r) \approx -\alpha_q^{(j)}I_0 + \frac{2\alpha_q^{(j)}I_0}{w^2}r^2 \tag{3.6}$$

for the central part of the beam where $r < w$. The interference of these two different phase fronts in the far field results in an annular fringe pattern. This pattern obviously changes with time as the laser intensity varies in the laser pulse.

In the temporal domain, Equation (3.5) results in a phase modulation – a chirp – of the harmonic emission, which is the stronger the longer the trajectory is:

$$\Delta\omega(t) = -\frac{\partial\phi_q^{(j)}(t)}{\partial t} = \frac{\partial\alpha_q^{(j)}(I(t))}{\partial I}\frac{\partial I(t)}{\partial t}\cdot I(t) + \alpha_q^{(j)}(I(t))\cdot\frac{\partial I(t)}{\partial t} \approx \alpha_q^{(j)}\cdot\frac{\partial I(t)}{\partial t} \approx -\frac{4\alpha_q^{(j)}I_0}{\tau^2}t. \tag{3.7}$$

This harmonic chirp maps the time to a frequency shift in the harmonic spectrum. The emission generated by the leading or trailing edge of the pulse is thereby mapped to higher or lower energy respectively. At the temporal peak of the laser pulse, the exact harmonic frequency is created because $\frac{\partial I(t)}{\partial t} = 0$ (Equation (3.7)).

In addition, spatio-temporal effects appear. Since the contributions from the temporal wings are generated with lower spatial peak intensity, they should appear with a smaller divergence in the recorded far-field pattern (see Equation (3.6)). One thus expects that the spatial extent of the harmonic beam will be largest at the central harmonic frequency and will decrease on both spectral sides.

By spatially and spectrally resolving the harmonic emission, it should be possible to observe the QPI in the two dimensions.

3.3.2   Experimental setup

In our experiments (Figure 3.12), near infrared laser pulses centered at 800 nm wavelength with a duration of 30 fs and a pulse repetition rate of 1 kHz have been focused into an argon gas jet by a spherical mirror (ROC = 500 mm).
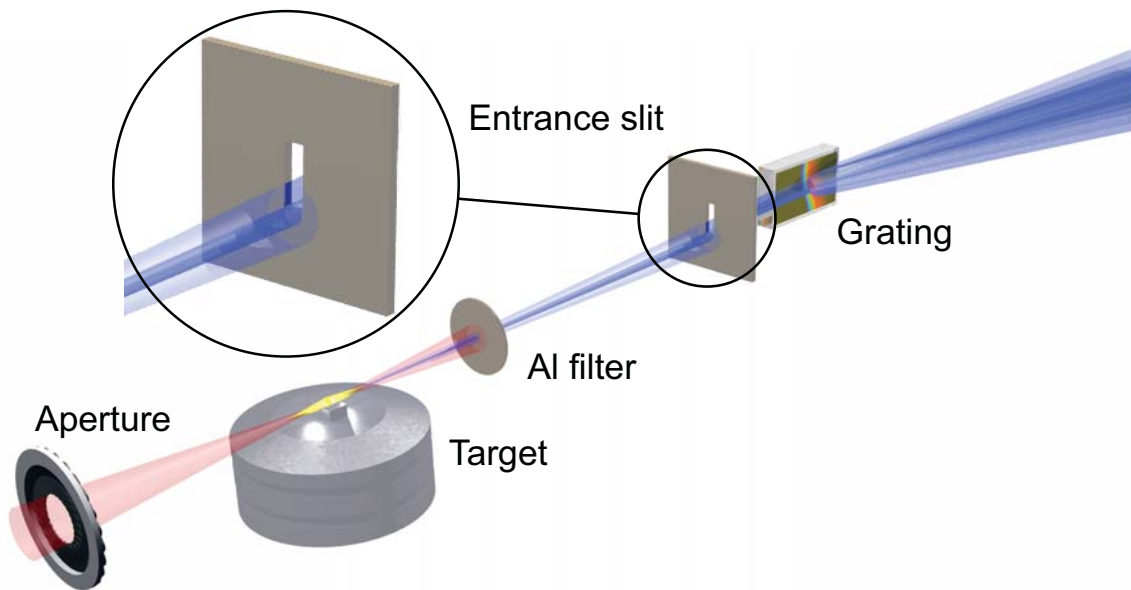
Figure 3.12: Experimental setup. The incoming laser beam passes through an aperture and is focused into a pulsed argon jet. The harmonics propagate through an Al foil that filters out the intense generating laser beam. The strong center part of the harmonic emission is cut by the entrance slit of the spectrometer.

The laser peak intensity was changed from $6.0 \cdot 10^{13}$ W/cm^2 to $3.3 \cdot 10^{14}$ W/cm^2 by using a variable attenuator (half-wave plate and polarizer). To find proper phase matching conditions, we adjusted both, the input beam aperture and the position of the

gas jet along the propagation direction of the laser. In all our measurements, the gas jet was placed before the laser focus. Once an optimal configuration was found, it was left unchanged for all intensities. The emitted harmonic radiation hit the vertical 1-cm high slit of a XUV spectrometer (McPherson 248/310G) placed 1 m behind the jet. Spatial resolution was obtained with a 2-dimensional CCD detector. We adjusted the weight of the different quantum path contributions by moving the incoming beam in the vertical direction (corresponding to the slit direction) and therefore controlling the portion of the beam entering the spectrometer. Blocking the intense central part of the harmonic beam resulted in an increased visibility of the weaker parts with high divergence.

3.3.3   Results

Spatially and spectrally resolved harmonics have been measured for different laser intensities. To clarify the general behavior, we first discuss a spectrum recorded at fixed laser intensity. The spatially resolved spectrum shown in Figure 3.13a) was recorded at a fixed peak intensity of $3.3 \cdot 10^{14}$ W/cm^2 in argon. Each spectral component plotted along the horizontal axis is spatially resolved along the vertical axis. We have observed spatial and spectral modulations of the harmonic yield. The areas with constructive interference create a parabolic structure: Moving from the blue side of the harmonics to the exact harmonic frequency to the red side, these areas first increase in divergence, reach their maximum and decrease again. Applying the time-to-frequency mapping of the harmonic chirp, one sees that these areas increase in divergence on the leading edge of the pulse until the temporal peak of the pulse is reached, and then decrease in divergence on the trailing edge. Since the harmonic phase difference $\Delta\phi_q(t) \approx \Delta\alpha_q \cdot I(t)$ is proportional to $I(t)$, the parabolic shape is to be expected close to the maximum of the laser envelope where the harmonics are emitted.
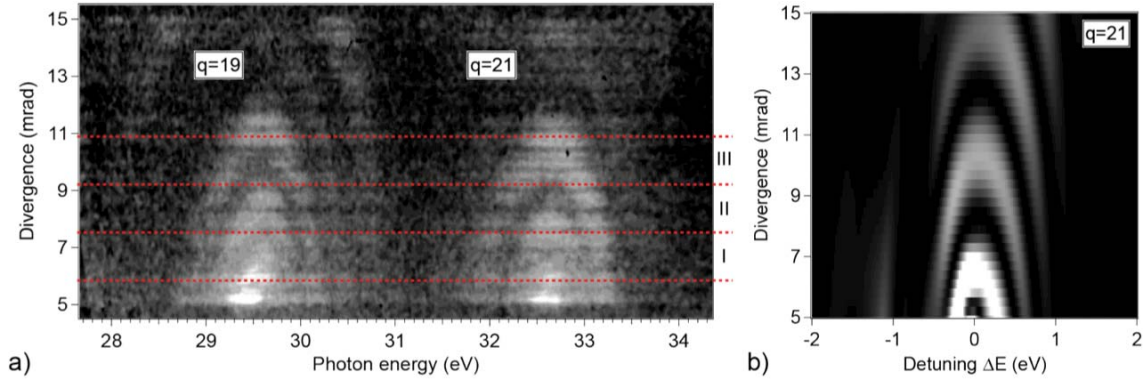
Figure 3.13: Spatially resolved harmonic spectrum. a) Measured and b) simulated result. The measured data shows harmonic orders 19 and 21 at a fixed intensity of $3.3 \cdot 10^{14}$ W/cm^2. The simulations were done for harmonic 21 at a peak intensity of $2.5 \cdot 10^{14}$ W/cm^2.

The interference structure disappears for a jet positioned after the laser focus where the short quantum path dominates the emission. The latter holds true also for the center part of the beam, which is orders of magnitude more intense even for a jet positioned before the laser focus. It was therefore crucial to suppress this part of the beam. However, the very low signal makes it very difficult to measure the spatial fringe pattern. Our experimental results are reproduced by SFA calculations and consecutive propagation of the electric fields. In Figure 3.13b) a calculated spatially resolved harmonic spectrum is shown for a fixed laser peak intensity of $2.5 \cdot 10^{14}$ W/cm^2. A fringe pattern very similar to the measured one is obtained. To our knowledge, this is the first time that QPI is observed inside the harmonic beam, and not as a variation of the beam properties. Indeed, when the laser intensity is varied, the fringe pattern is altered: the rings move outwards as the intensity increases (Figure 3.14a). In the previous experiments (Section 3.1 and 3.2), the harmonic beam was integrated within an off-axis spatial filter window, and we measured the modulations of the harmonic yield with laser intensity as the rings of the QPI interference pattern were moving across the spatial filter [159]. We were thus measuring the variation of the pattern, not the pattern itself. This is a significant step towards a full characterization of the harmonic emission. Note that QPI leads to an annular interference pattern that is very different from the fringe pattern resulting from two spatially separated sources. The latter exhibits vertical stripes in the beam profile and was used in, e.g., [160, 161] to get information on the phase of the quantum paths through the interference of contributions from the same quantum path (short or long) from the two separate sources. However, no interference of contri-

butions from the short trajectory with contributions from the long trajectory was reported.
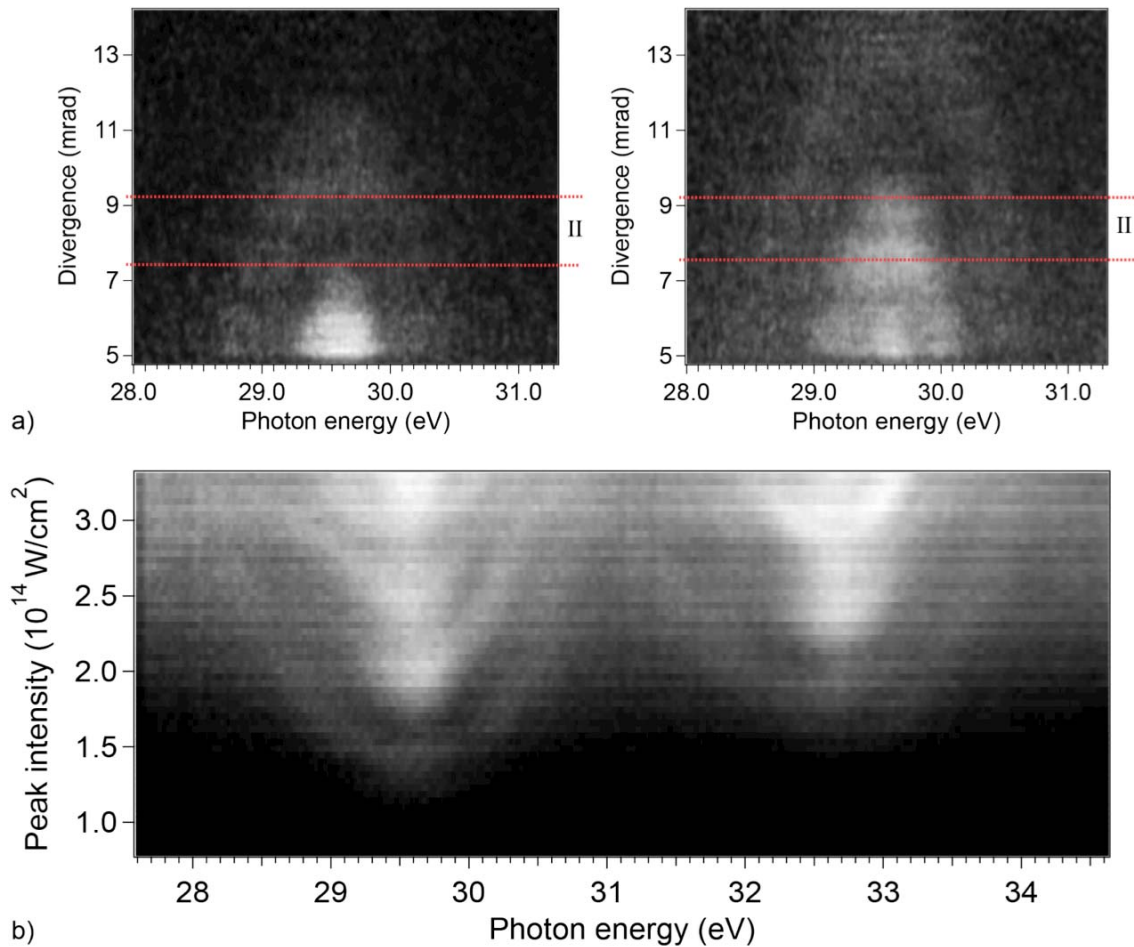
Figure 3.14: a) Spatially resolved spectrum of harmonic 21 for a laser peak intensity of $1.6 \cdot 10^{14}$ W/cm^2 (left) and $2.0 \cdot 10^{14}$ W/cm^2 (right). b) Harmonic signal integrated from 7.5 to 9.2 mrad (area II in a) and in Figure 3.13a) along the spatial coordinate.

By recording spatially resolved spectra for different laser peak intensities and then performing a numerical integration over an interval in the spatial direction, we can reproduce the previous results from Section 3.1 and 3.2 as shown in Figure 3.14b). Please note that in the current experiment our spatially resolving spectrometer has less dynamic range since is uses a MCP with phosphor screen, which is then imaged to a CCD sensitive in the visible instead of direct detection by an XUV CCD. The spatial window used for the integration is indicated by the red lines in Figure 3.13a). A corre-

sponding line-cut at the exact harmonic frequency then shows modulations of the harmonic yield with laser intensity.
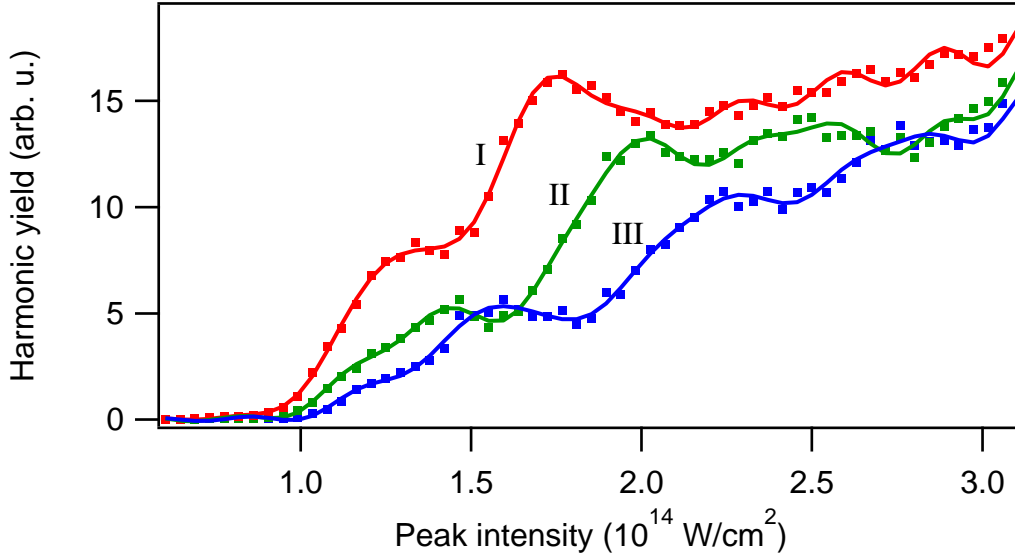
Figure 3.15: Harmonic yield versus laser intensity for three different spatial integration windows (marked in Figure 3.13a) for harmonic order 21 (measured data shown as dots, solid lines show data smoothed by Fourier low-pass filtering).

In Figure 3.15, three non-overlapping integration windows for harmonic 21 (areas marked in Figure 3.13a) by I, II, III) were chosen. Moving the integration area to higher divergence (from region I to III) shifts the modulations to higher intensities and the modulation period increases. A possible interpretation is that the harmonic emission in the outer part of the beam (high divergence) was created with a lower effective intensity. This is the case if the curvature of the harmonic phase front is that large at the exit of the generating medium that the spatial pattern is directly projected into the far field. As a consequence, the contributions in the observed far-field spatial regions are generated at a position in the spatial wings of the laser pulse $r^{(1)} = r^{(2)} \neq 0$ where the intensity is lower than the peak intensity. One then expects that the resulting QPI modulations will be shifted to higher peak intensity (and their period will be increased) as compared to the modulations in the inner part of the harmonic beam generated at r closer to 0. If the phase front curvatures of contributions from the short and the long quantum path are sufficiently different, one may even consider that they originate from two different positions $r^{(1)} \neq r^{(2)}$ within the medium such that $\Delta\alpha = \Delta\alpha_q\left(I(r^{(1)}, t), I(r^{(2)}, t)\right)$.

When the harmonic dipole is restricted to the short ($\tau_q^{(1)} \approx T/2$, $\alpha_q^{(1)} \approx 1-5\cdot10^{-14}$ rad cm^2/W) and the long ($\tau_q^{(2)} \approx T$, $\alpha_q^{(2)} \approx 20-25\cdot10^{-14}$ rad cm^2/W) trajectory (T being the oscillation period of the laser field), the theoretically expected interference period of the two first quantum paths is $2\pi/\Delta\alpha \approx 3-4\cdot10^{13}$ W/cm^2 . This is in excellent agreement with our experimental observations for a spatial integration window close to the center of the beam. The measured periodicity for a spatial integration window marked with I in Figure 3.13a) is $4\cdot10^{13}$ W/cm^2. This periodicity increases to $7\cdot10^{13}$ W/cm^2 for the integration window marked with III. For higher harmonic orders in the cutoff region, modulations are not observed because only one trajectory contributes to the emission (data not shown). We can thus conclude that the behavior observed in the numerically integrated spatially resolved data is consistent with our results in Sections 3.1 and 3.2 and previously published in References [135] and [136].

In addition to our confirmed previous observations, spatial resolution of the QPI spectra should give us access to faster oscillation periods resulting from higher order electron trajectories that could be averaged out by the spatial integration. Fourier analysis of our data however did not clearly reveal such signatures. A possible reason for the absence of higher order modulations in the Fourier transform of the QPI data could be the relatively low signal-to-noise ratio of our data that prevents us from detecting the theoretically predicted weak contribution of higher order trajectories. Indeed, the quantum diffusion during their long excursion time results in a much lower recombination probability compared to the two shortest trajectories.

Another benefit of spatially resolved measurements is that they provide a means to identify a possible contribution to intensity-dependent modulations of the harmonic yield, which is not due to QPI. Slow spectral modulations appear when the single-atom response is calculated with SFA using only the shortest trajectory [137]. These modulations cannot be attributed to QPI, but are a direct consequence of the harmonic phase modulation. All frequencies apart from the exact harmonic frequency can be generated at two different instants of time within the laser pulse envelope leading to a possible interference between these contributions. However, this is simply a spectral redistribution of the frequency components and does not affect the spectrally integrated signal. Therefore, the spatially resolved emission gives us an accurate tool to distinguish between QPI and interference due to phase modulations: the latter should disappear when spectrally integrating the spatially-resolved signal, while QPI modulations should

persist (with a decreased contrast due to the temporal averaging over the envelope of the laser pulse).
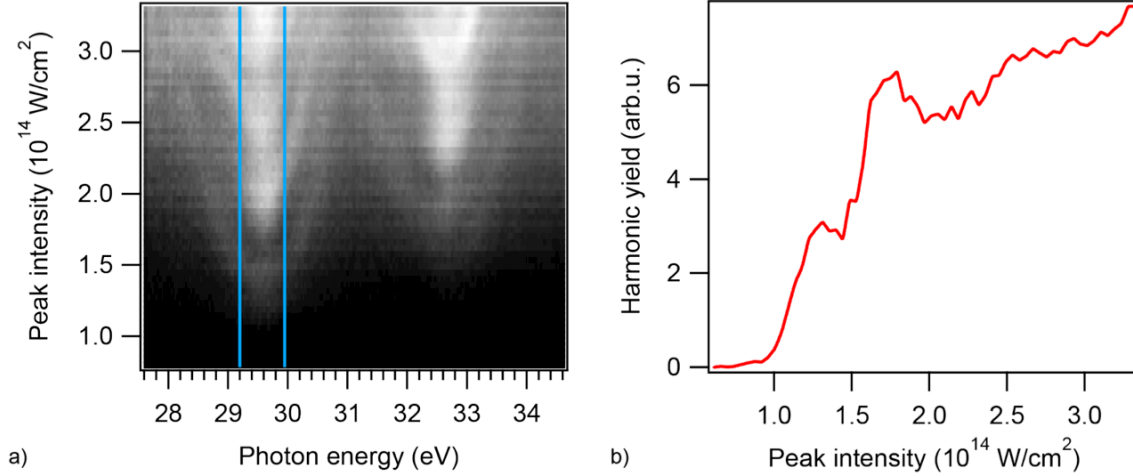
Figure 3.16: a) Spatially integrated (5.80 – 5.88 mrad) yield for harmonic 19 and 21. b) Spectral integration over area indicated in a). The spectrally integrated yield is still modulated with a periodicity of ~$4 \cdot 10^{13}$ W/cm^2, which is a clear indication for QPI.

In Figure 3.16a) spatially integrated spectrum with an integration window of 5.80 to 5.88 mrad is shown. This small spatial integration was performed just to increase the signal to noise ratio. When spectrally integrating harmonic 19, the harmonic signal is still modulated with a periodicity of ~$4 \cdot 10^{13}$ W/cm^2, as can be seen in Figure 3.16b). As a result, phase modulation can be excluded as the origin for the appearance of an interference structure.

3.3.4   Conclusion

By recording spatially resolved spectra of high order harmonics generated in argon, we found fingerprints of quantum path interference between the two shortest quantum paths. Our measurements represent the first observation of QPI inside the harmonic beam. The parabolic structure of the spatially and spectrally resolved emission can be explained by the intensity dependence of the harmonic phase of the two trajectories and the corresponding time-to-frequency mapping. Our experimental results underline the necessity of spatial filtering and blocking of the central part of the beam to observe the QPI and are fully supported by simulations including SFA-calculation of the single-atom response and propagation of the electric fields in the macroscopic medium.

When performing a – partial – spatial integration of the signal, we find that the modulation period of the QPI increases when moving the integration window to higher divergence. We attribute this behavior in the outer region of the harmonic beam to the generation of the signal at a position in the spatial wings of the laser beam (or even at two different positions) with lower effective intensity than the peak intensity. Furthermore, we can reproduce our previously reported measurements (Section 3.1 and 3.2, [135, 136]) when integrating the spatially resolved signal over the same window.

By spectrally integrating the harmonic yield, we rule out the phase modulation as the origin for the occurrence of interference fringes. With improved signal-to-noise levels, our method has the potential to be a sensitive detector for QPI contributions from higher order electron trajectories and may thus yield first direct experimental evidence for such higher order contributions to high-order harmonic generation.

3.4 Alternative explanation for observed HHG yield modulations

In the previous Sections, we have discussed the properties of high-harmonic yield modulations resulting from the interference of the emission from different electron trajectories in the HHG process. These quantum-path interferences (QPI) are intrinsically a single-atom phenomenon. We have explained in detail under what conditions this single-atom response can be observed macroscopically. In essence, one needs a short generation medium, a spatial filter, and a spectral filter (equivalent to a temporal filter) to avoid macroscopic averaging over many modulation periods and thereby removing the signatures of QPI.

Throughout this discussion, we also made clear that phase modulation as an alternative source for intensity-dependent photon yield modulations in harmonic spectra can be ruled out as the origin of the observed fringes. Since phase modulation only results in a spectral redistribution of the photons, harmonic yield modulations resulting from this process do not survive spectral integration (see, e.g., Figure 3.16).

Very recently, Heyl et al. [162] brought up yet another possible explanation for the observed structures. They experimentally and theoretically investigated transient

phase-matching in HHG. They attribute the observed modulations to the well-known Maker fringes from conventional nonlinear optics [163].

In a simplified one-dimensional and homogeneous nonlinear optical medium, the photon yield S from the nonlinear interaction scales as

$$S \propto L^2 \mathrm{sinc}^2\left(\frac{\Delta k L}{2\pi}\right), \tag{3.8}$$

where L is the nonlinear medium length and Δk is the wavevector mismatch (or wavenumber mismatch in the one-dimensional case). The Maker fringes originate from the oscillatory behavior of the sinc^2 function upon variation of Δk. In a practical HHG scenario, Δk depends on a variety of parameters [131]. The wavevector mismatch depends in particular on instantaneous laser intensity and thereby intrinsically becomes space and time dependent. As a result, local harmonic yield maxima may occur in time and space.

Heyl et al. [162] now found that the local HHG yield maxima in space as well as the temporal maxima mapped into frequency domain through the harmonic chirp may result in fringe patterns that closely resemble those observed in our experiments. These fringe patterns would thus result from a macroscopic effect (phase matching) rather than from a single-atom process as in the case of QPI. Furthermore, since the fringes are not a result of the interference of the emission from different electron trajectories, they can be observed when only one quantum path (the long one) is phase matched.

In the following we give arguments why we think that we observed QPI and not just Maker fringes. It needs to be stressed, however, that this does not rule out that at least parts of the observed modulations can be attributed to pure phase matching effects.

a) The modulations observed in our experiments always vanish towards the harmonic cut-off. This is expected in the QPI picture since the two quantum paths are degenerate for the cut-off harmonics (i.e., only one dominant trajectory exists). There is no similarly strong argument why the Maker fringes should disappear towards the cut-off. It needs to be noted, however,

that the time-to-frequency mapping on which the observation of the Maker fringes relies scales with the reciprocal intensity $\alpha_q^{(j)}$. For the long trajectory, this parameter becomes smaller as one approaches the cut-off. It thus becomes more difficult to observe the Maker fringes.

b) Experimentally, we find that the proper regime for observing the harmonic yield modulations is not trivial to find and needs a careful selection by an off-axis spatial filter. There is no intrinsic reason why this should be the case with the Maker fringes. Furthermore, Heyl et al. [162] report that they observe their modulations in an on-axis section of their harmonic beam (± 11 mrad horizontal and ± 5 mrad vertical spatial filter). In contrast, we observe only spectrally narrow and unmodulated harmonics on-axis (see, e.g., Figure 3.6).

c) We find experimentally and theoretically that the locations of modulation maxima and minima for small detuning from the exact harmonic frequency are robust against pressure changes (see, e.g., Figure 3.8). This is indicative for a microscopic origin of the modulations and is not expected for Maker fringes since the wavevector mismatch Δk directly depends on particle density. However, we also confirmed (Subsection 3.2.1) that the fringe pattern for larger detuning from the exact harmonic frequency does sensitively depend on macroscopic parameters. It can therefore not be ruled out or is even expected that a Maker fringe like process contributes to the pattern in these spectral regions.

d) The modulation periods that we observe are consistent with those expected from single-atom theory. Error bars are however relatively large and this could be just by coincidence. Nevertheless, this circumstance provides further evidence for the correctness of the QPI interpretation.

To summarize, we think our experiments and the theoretical analysis provide sufficient evidence to proof that we indeed observed QPI in HHG. It is, however, also likely that QPI is not the sole contributor to the measured modulation structures. This applies in particular to fringes at larger detuning from the exact harmonic frequencies. In these spectral regions, overlap between spectral content from the short and the long trajectories becomes smaller and we observe an increased sensitivity towards phase

matching effects. We expect that the concept of Maker fringes as introduced by Heyl et al. [162] plays a role in this context.

This discussion shows that the process of high-order harmonic generation that underlies many applications in strong-field and attosecond science is almost 25 years after its discovery [20, 21] still not fully understood.

Chapter 4

Attosecond beamline

In this Chapter, we will give a brief overview of the experimental setup for attosecond science that was constructed at ETH from the end of 2006 to early 2008. While all results presented in Chapter 3 have been recorded on an earlier high-harmonic setup, it was found that this implementation lacks the mechanical stability and the flexibility required for true attosecond time-resolved experiments. The poor mechanical stability was not an issue for the observation of quantum path interferences as they occur "intra-pulse" on a single-atom level.

4.1 Design goals and implementation

The design goals for our new attosecond beamline were mostly driven by the shortcomings of the old setup and the desired flexibility demanded by potential future directions. We decided that the new experimental apparatus would sit on an optical table for increased total mass/inertia and resulting stability. The entire optical path required for the pump-probe delay line, attosecond pulse generation, and possible processing of the infrared beam (e.g., frequency conversion or beam shaping) shall fit on a single common platform kept under vacuum. The common platform was designed to be rigidly connected to the supporting optical table at multiple points.

Another shortcoming of our hold high-harmonics setup was that it employed a back-focusing geometry in its target chamber. That way, the XUV beam was required to pass the target area twice. Since the XUV photon energies induce single-photon absorp-

tion in essentially every medium, this resulted in many stray electrons created by the unfocused harmonics beam on its way to the focusing mirror. To avoid this double-pass of the XUV beam, we decided to design our beamline for a front focusing geometry. At the same time care was taken to maintain the flexibility to convert the setup into a back-focusing geometry at a later stage if a particular experiment requires this.

Furthermore, the efficiency of collection and redirection of the XUV photons passing the target chamber into the XUV spectrometer was aimed to be as high as possible. And decoupling from external vibration sources was a prime objective.
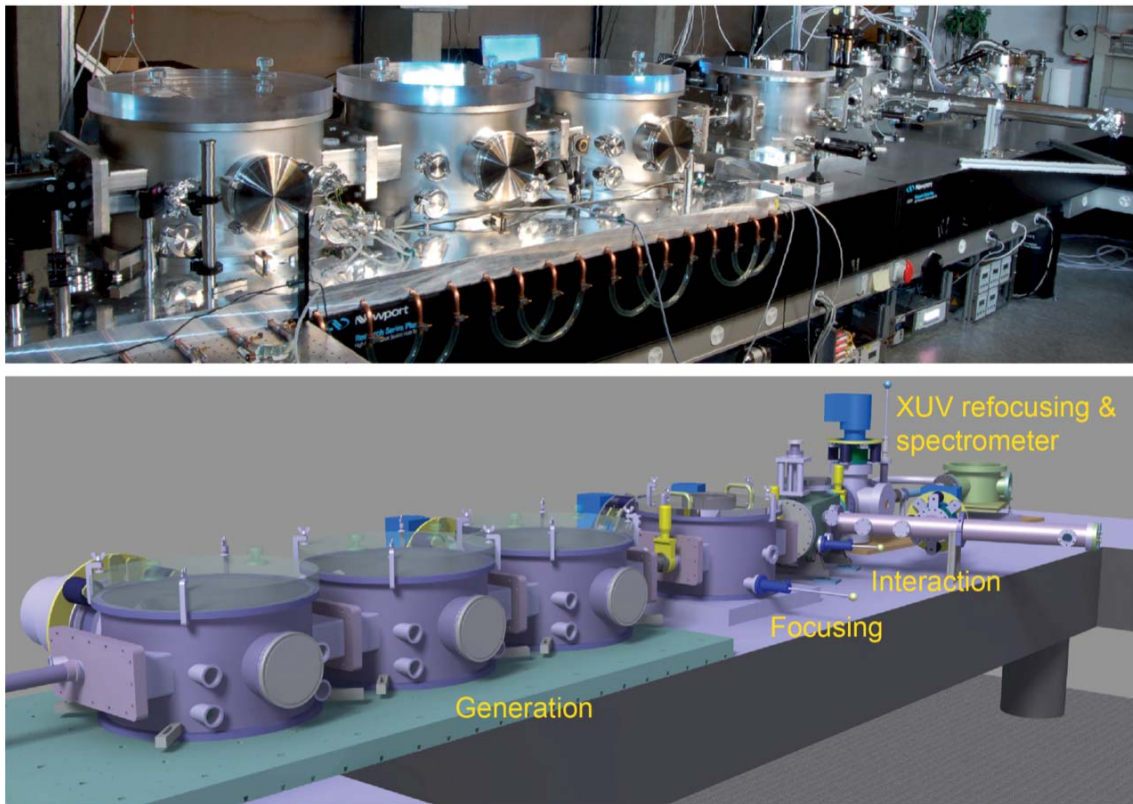
Figure 4.1: Attosecond beamline design (bottom) and implementation (top).

Figure 4.1 shows the final design of the beamline and a picture of the operational setup. The infrared laser beam enters from the left through an evacuated tube. A small chamber (not shown) before the actual beamline contains a beamsplitter that picks up a small fraction of the beam. This reflection is used for active pointing stabilization of the laser beam into the attosecond beamline. This is needed because the laser system

is located in another laboratory several meters from the experimental chamber on its own optical table.
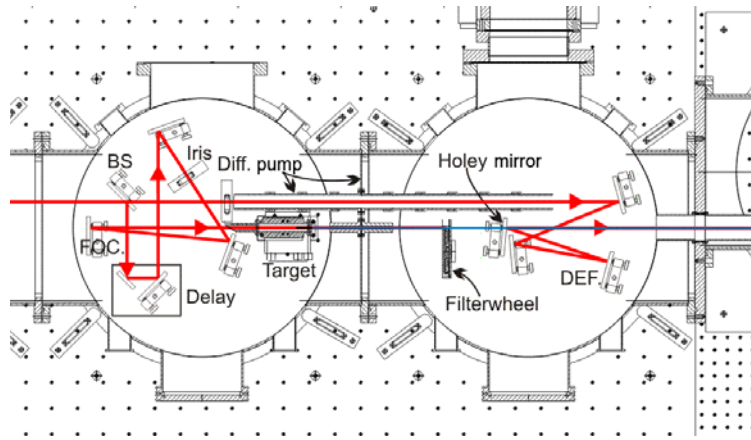
Figure 4.2: Example of optical layout in generation chambers (for this particular setup only two of the three chambers are used). The shown setup could for example be used for RABBITT characterization of the generated attosecond pulses [125, 164].

After the small chamber used for pointing stabilization, the infrared beam enters the generation part of the beamline. The generation section is rather large and consists of three separate chambers. This design choice was driven by the maximum chamber size that can be manufactured in-house. The three generation chambers sit on a common 60 mm thick aluminum base plate. Aluminum was chosen because of its considerably lower weight and cost compared to steel. The plate is temperature stabilized to prevent flexing under changing temperatures resulting from the material mismatch to the optical table and vacuum system. In addition, the plate is rigidly bolted to the optical table from outside of the vacuum as well as from the inside of the vacuum (with O-ring sealed screws). The generation chambers are directly clamped to this bottom plate and O-ring sealed for vacuum tightness. The three generation chambers are interconnected by large rectangular and reconfigurable flanges. The flanges can serve as differential pump stages. The high-harmonic generation target is typically located in the center chamber. All the rest of the optics needed for beam focusing, shaping and pump-probe delay are distributed throughout the generation section. After a thin aluminum filter suppressing the remaining infrared, the XUV beam passes through a center hole of a silver mirror. There, it is recombined collinearly with an additional delayed infrared beam for pump-probe type of measurements. An example of an optical setup in the generation section of the beamline is shown in Figure 4.2.
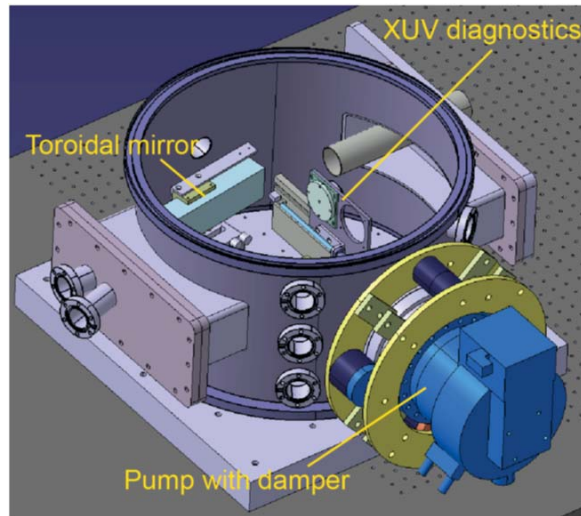
Figure 4.3: Focusing chamber with toroidal mirror and XUV beam diagnostics (view from opposite side compared to Figure 4.1; i.e., beam enters from the right).

After the generation section, the beam is directed through another differential pump section into the focusing chamber (Figure 4.3). Its dimensions are identical to the three generation chambers. The focusing chamber hosts the gold coated toroidal mirror that focuses the combined XUV and IR beams into the interaction chamber. It performs a 1:1 imaging from the high-harmonic generation focus into the interaction focus. The mirror can be removed from the beam path if one plans to perform an experiment in a back-focusing geometry. The chamber also contains a calibrated photo-diode for absolute XUV flux measurements and an XUV beam profiler. Figure 4.3 also gives a nice view of the turbo-molecular pump fitted with our own design of vibration dampers. They consist of two rings welded to a flexible bellow and connected through rubber dampers. This design yields about 25 dB of damping while reducing pumping capacity by merely 8%.

The interaction chamber was not changed compared to the old setup and is therefore not described in detail. It is a rectangular chamber that contains the gas target for our experiments. We use a home-built electron time-of-flight spectrometer to record spectra of the generated photo-electrons. The transmitted XUV beam is directed to a gold coated spherical mirror under 10° grazing angle. This mirror focuses the XUV beam as a highly astigmatic line focus onto the entrance slit of a commercial XUV spectrometer (McPherson model 251). The spectrometer is equipped with a XUV-sensitive CCD camera.
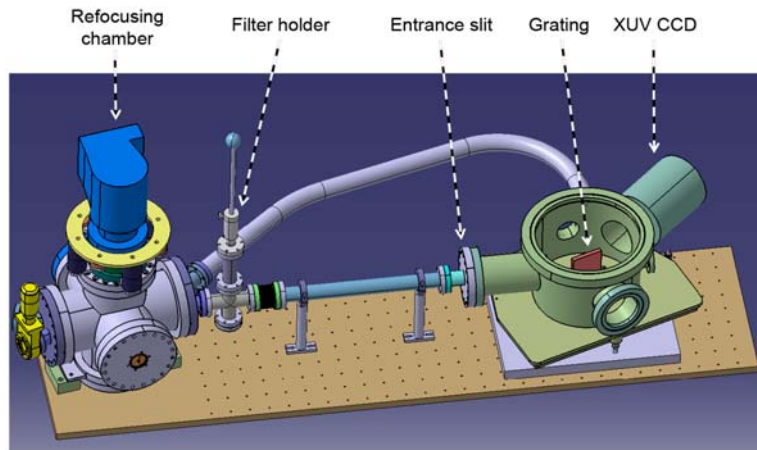
Figure 4.4: XUV detection consisting of a refocusing mirror and an XUV spectrometer.

4.2   Attosecond pulse train characterization

The first experiment that we performed on the new attosecond beamline served the characterization of the generated attosecond pulse trains. We characterized their structure in time using reconstruction of attosecond harmonic beating by interference of two-photon transitions (RABBITT, [125, 164]).

An early data set of a RABBITT characterization of an attosecond pulse train generated in argon is shown in Figure 4.5. The full data matrix took 30 h to record. The delay range depicted in Figure 4.5 corresponds to about 12 h of measurement time. The regular and smooth modulations demonstrate not only the stability of our laser system during that time but also the mechanical stability of our experimental setup.

Figure 4.6 shows the data obtained from the RABBITT characterization. The reconstructed average pulse duration for the pulses in the attosecond pulse train is 450 as. The pulses could be compressed closer to their transform limit of 160 as by changing the thickness of the aluminum filter used to separate the pulse train from its driving infrared laser pulse [165]. For our case, we obtain an optimum thickness of 500 nm for the aluminum filter.

The photon flux of the attosecond pulse train was measured with the calibrated photo-diode located in the focusing chamber. We determined a total XUV pulse energy

of 1.4 nJ, corresponding to $2.4 \cdot 10^8$ photons per shot. The total infrared to XUV conversion efficiency was $2.8 \cdot 10^{-6}$.
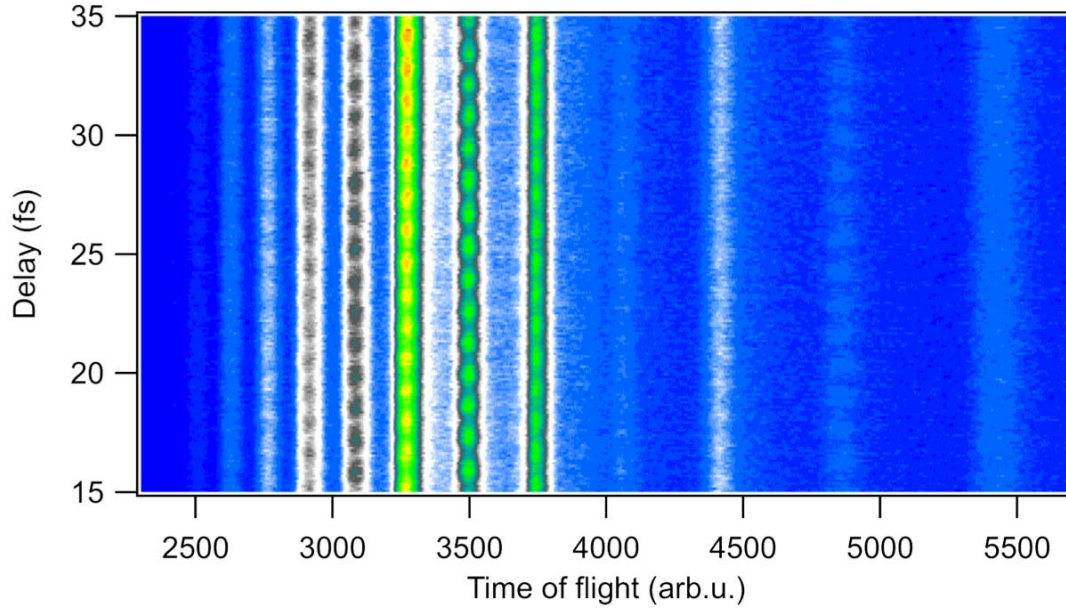
Figure 4.5: Data set from RABBITT scan. The bottom axis represents the raw electron time-of-flight bins. The raw data is shown with no post-processing applied.
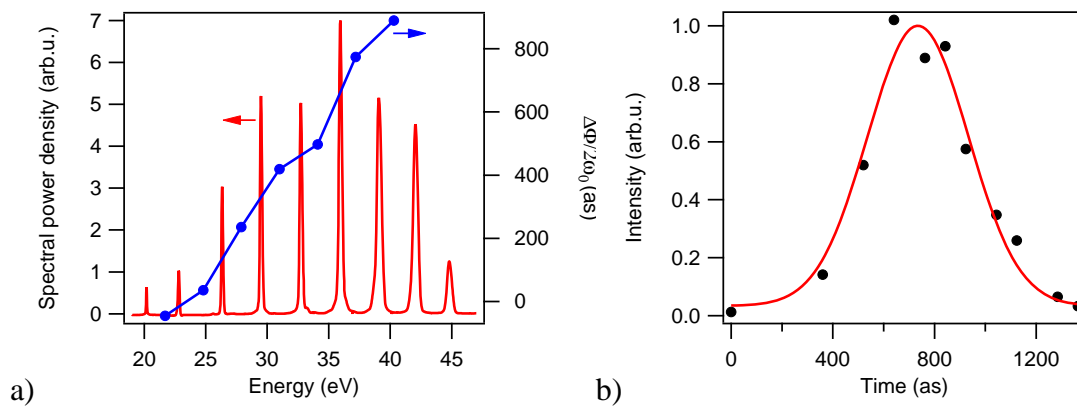
Figure 4.6: Pulse reconstructed from RABBITT. a) Corresponding harmonic spectrum (red) and phase (blue). b) The temporal pulse profile has a full width at half maximum of 450 as. The transform limit of the spectrum is 160 as. The actual reconstructed data is represented by the black dots. The red line corresponds to a fitted curve.

4.3 Future directions

We plan to expand the attosecond beamline towards the capability of delivering attosecond pulses to two experimental chambers. This way it should become possible to change relatively quickly from one experiment to another. For this purpose, we will replace the current refocusing chamber located between the interaction chamber and the XUV spectrometer. In its place, we will insert a new beam routing chamber that will allow switching between the present spherical refocusing mirror and a second toroidal mirror. The toroidal mirror deflects the beam into the opposite direction compared to the spherical mirror and reimages the focal area of the interaction chamber into a second interaction region. The first interaction chamber will continue to be devoted to gas phase experiments, whereas the second interaction zone will be used to accommodate experimental chambers from external collaborators. First experiments on surface physical systems are planned for the end of 2011.

Chapter 5

Attosecond transient absorption

Traditionally, photo-electron or photo-ion spectra or momentum distributions are recorded in attosecond time-resolved experiments. Most of the experiments use the streaking of electrons by a strong infrared laser field and the energy-resolved detection of these particles as the fundamental measurement principle (see, e.g., [3, 5-8, 10, 11]). The principle of streaking is that the free electrons are near-instantaneously created through ionization of the target, e.g. by an isolated attosecond pulse, and then accelerated in the strong oscillating infrared laser field [126]. The detected electron momentum distribution experiences a shift that depends on the relative timing between the ionization event and laser pulse. If recorded over a range of delays, one thus essentially measures a crosscorrelation between the created electron wavepacket and the electric field of the laser. As this measurement depends on the electric field of the pulse rather than its envelope one attains sub-femtosecond resolution despite crosscorrelating with a multifemtosecond pulse. Under suitable conditions one can then extract information about the dynamics of the system under study from this crosscorrelation data.

The streaking methods are by far the most successful and most versatile approaches to attosecond time-resolved spectroscopy demonstrated so far. Similar concepts were also used with attosecond pulse trains [12] – with additional information contained in the inteference between successive attosecond pulses. While the streaking techniques are very successful and difficult to replace for certain applications, they share in common a number of shortcomings:

- The intrinsically required strong laser field distorts the system under test

- Charged particles are detected, which limits measurement speed (space-charge effects) and signal-to-noise

- It is questionable whether the current streaking approaches can be transferred to systems exhibiting complex dynamics

The streaking field can generate a significant background signal through above-threshold ionization. It is often very challenging to find proper operation parameters that allow extracting the actual streaking signal from such a background. This is usually the more difficult the smaller the energy of the electrons one wishes to detect and the lower the ionization threshold of the target. Given these difficulties, which come in addition to the already major challenge of generating isolated attosecond pulses in the first place, it is not surprising that most of the streaking studies performed so far have been done on simple model systems where the outcome of the experiment could be guessed beforehand. They thus were rather a test of the methods than of the system being studied.

A new measurement method that was recently reported by three different research groups holds promise to address some of the major shortcomings of the streaking techniques. This new and purely optical method is called attosecond transient absorption [26-28]. We were the first to demonstrate this new technique with trains of attosecond pulses and reported the so far only transient absorption experiment observing true sub-cycle dynamics [28]. In transient absorption spectroscopy, there is no intrinsic need for the presence of a strong laser field and it relies on the detection of photons. Photons do not suffer from space-charge effects and can be detected very efficiently, sensitively, and with high dynamic range using existing CCD technology. We have shown that for comparable experimental parameters we gain about two orders of magnitude in measurement time (6 min vs. 10 h) for a full pump-probe scan when using transient absorption rather than conventional electron detection using a time-of-flight spectrometer (see, e.g., Section 4.2). Such a speed-up in measurement time is a prerequisite for certain experiments, e.g., in surface science, where surfaces may contaminate/oxidize in tens of minutes even under vacuum. Transient absorption does also not suffer from the above-threshold-ionization background problem of streaking and allows selective probing of

transitions and resonances. Furthermore, transient absorption is capable of directly probing bound-bound transitions, which is intrinsically impossible with photo-electron/photo-ion detection. Due to its high sensitivity it is expected to be a promising route towards true attosecond pump – attosecond probe experiments, a holy grail currently out of reach for existing attosecond technology. The combination of transient absorption with spectral interferometry may lead to phase sensitive measurement schemes. It also needs to be stated that transient absorption does probe a fundamentally different physical observable in a time-dependent system than the traditional schemes based on ionization and may thus provide additional, otherwise inaccessible information [28].

In Section 5.1 we will report on an experiment using transient absorption spectroscopy for the detection of transiently bound electron wavepackets in helium. These experiments also yielded additional observations that are not yet fully understood. We will show this data in Section 5.2.

Results in this Chapter have been published in Ref. [28].

5.1   Attosecond electron wavepacket interference observed by transient absorption

The availability of light pulses in the extreme ultraviolet (XUV) and with attosecond duration [125, 126] enables the direct observation of the dynamics of electrons on their natural time scale. Isolated attosecond pulses [126] are usually preferred for traditional pump-probe measurement schemes. For example, they have been used for studying the dynamics of various ionization processes in atoms [6-8] and on the surface of solids [3]. Attosecond pulse trains (APT, [125]) on the other hand allow for probing the interference of electron wavepackets initiated by the individual pulses in the train [12, 13, 166]. The interference of subsequent wavepackets enhances the sensitivity of the method and enables the extraction of phase information.

Recently, the ionization probability of helium atoms with APT photon energies below the ionization threshold in presence of a time-delayed infrared (IR) field was studied [166]. It was found that the ion yield is modulated with twice the IR driving laser frequency. The result was explained by the interference of transiently bound electron

wavepackets (EWP). We investigated this physical system with the all-optical approach of attosecond time-resolved transient absorption spectroscopy. Instead of detecting ions or electrons, we spectrally resolve the transmitted harmonic radiation in the presence of a time-delayed IR field. Our experiment probes a different physical observable than electron or ion detection and reveals more insight into the time-dependent perturbation of the atom by the IR field including contributions from bound-bound transitions. While transient absorption is a well-known measurement technique in the femtosecond domain (see, e.g., [167] for transient absorption with high-order harmonic sources), it was only recently extended into the attosecond regime using isolated attosecond pulses [26]. The different aspects probed by our optical technique compared to the experiment by Johnsson et al. [166] allows us to verify the plausibility of the previously introduced intuitive theoretical model and to demonstrate attosecond control of the relative absorption of the individual spectral constituents of an APT. This rapid absorption modulation represents the fastest dynamics resolved by all-optical methods so far.

5.1.1   Experiment and previous findings

Figure 5.1 shows the experimental configuration (a) and the spectral location (b) of the APT with respect to the energetic structure of helium. The APT is generated by high-order harmonic generation (HHG) in a xenon target with 30-fs pulses from a Ti:sapphire laser centered at 800 nm wavelength. The plasma induced spectral blue-shift in the xenon target results in an apparent driving wavelength of 785 nm. The remaining IR radiation is removed after the HHG source by passing the beam through a thin aluminum filter. A small part of the original Ti:sapphire laser beam is sent over a second independent optical path of the setup that can be time-delayed with respect to the APT. This relatively weak IR beam is recombined collinearly with the APT on a mirror with a center hole and then focused into a dense helium target (particle density $\sim 5\cdot 10^{17}$ cm^{-3}). The harmonic photons transmitted through the target are collected and sent into a XUV spectrometer equipped with a CCD camera. It is important to note that the infrared intensity chosen in the helium target (in the range from $0.7\cdot 10^{13}$ W/cm^2 to $1.7\cdot 10^{13}$ W/cm^2) alone is not sufficient to induce strong-field processes in ground-state helium. Furthermore, our APT consists mainly of harmonic orders 13 and 15, which are energetically located below the field-free ionization potential (IP) of helium and harmonic 17, which is above the IP (see Figure 5.1b). As a result, harmonic 13 and 15 are not absorbed in the absence of the infrared field unless they overlap with internal reso-

nances of helium. The latter is the case only for the weak spectral wings of harmonic 15, which can populate the *1s4p* and the *1s5p* from the helium ground state by single-photon absorption. The helium pressure is set such that about 50% of the photons at harmonic 17 are absorbed in the field-free case. The pulses in the APT were characterized with the RABITT technique (reconstruction of attosecond beating by interference of two-photon transitions, [125, 164]) to assure that the individual harmonics form indeed an APT. The average pulse duration in the train was found to be ~380 as. The full width at half maximum of the pulse train envelope can be estimated to be on the order of 10-12 fs, which would contain 8-10 attosecond pulses.
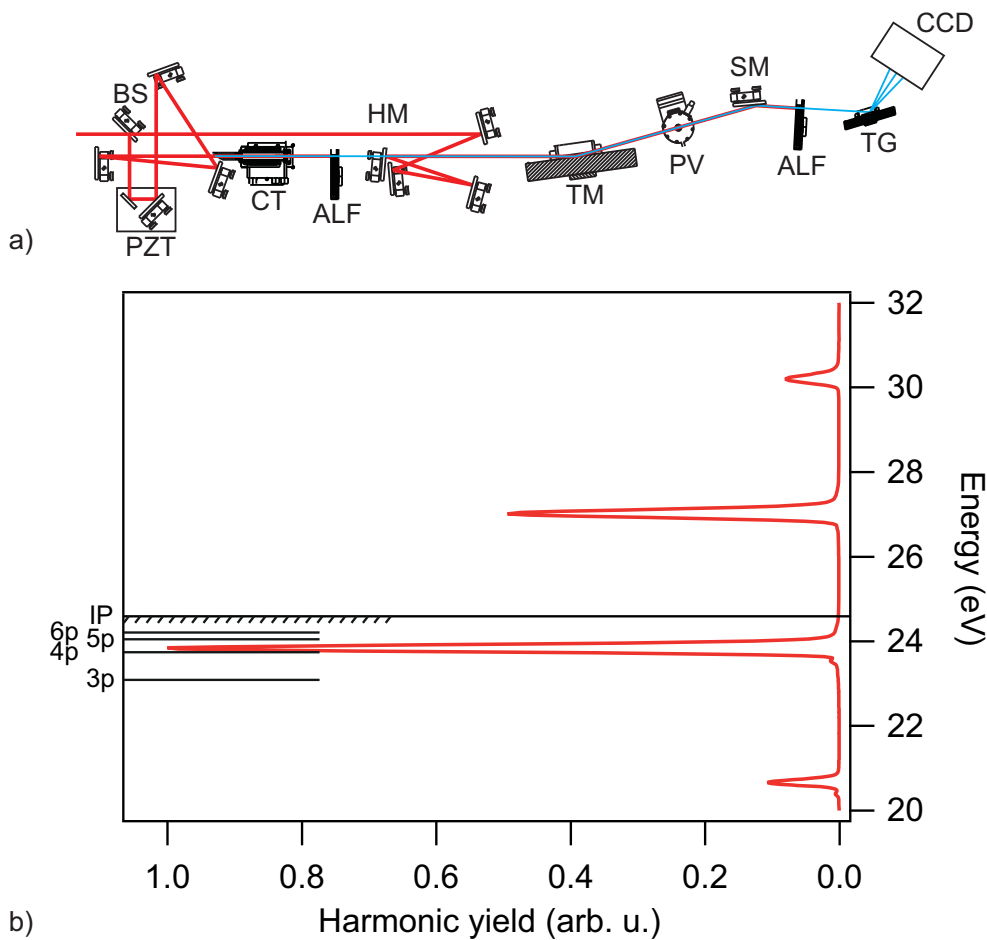
Figure 5.1: Experimental configuration. a) Setup for attosecond transient absorption. BS, beam splitter; PZT, piezo translation stage; CT, capillary target; ALF, Al-filter; HM, mirror with center hole; TM, toroidal mirror; PV, pulsed valve; SM, spherical mirror; TG, toroidal grating; CCD, XUV-CCD. b) Optical spectrum of the APT in relation to the energetic structure of helium. Only the field-free p-levels and first ionization potential are shown.

Figure 5.2: Schematic of the electron wavepacket dynamics generated by an APT in the presence of an additional IR-field. A pulse in the APT creates a transiently bound EWP in the potential modified by the IR-field. This EWP interferes with the EWP created by a subsequent pulse in the APT, rendering the process sensitive to the phase accumulated in the IR-field.

With an experimental setup and parameters similar to ours, Johnsson et al. observe periodic modulations of the He^+ ion yield as they change the relative delay between the APT and the IR field [166]. The modulation period corresponds to twice the fundamental frequency of the IR pulse. If they replace the helium target gas by argon, the modulations are absent. Johnsson et al. explain their observation by two effects. First, the oscillating IR field distorts the atomic potential and thereby modifies the absorption probability for the APT photons depending on the relative delay between the two fields. Second, transiently bound EWP initiated by the bursts forming the APT are accelerated by the IR field and have returned with a certain probability back into the vicinity of the ion when a subsequent attosecond pulse excites a next wavepacket. These processes are repeated with a half-cycle periodicity due to the symmetry of the system. The EWP are only transiently bound because the potential barrier may be sufficiently lowered for proper delay between the infrared and the APT such that the wavepackets can escape into the continuum. The interference between wavepackets excited by subsequent attosecond pulses significantly alters the ionization probabilities with delay. It is found that the second effect dominates the first one by an order of magnitude. This theoretical model is schematically pictured in Figure 5.2. In this study, Johnsson et al. also found theoretically that only 60-70% of the population transferred out of the

ground state by the XUV is ionized in the presence of an IR field, whereas roughly 30-40% of the population promoted by the XUV remains in an excited state. The probabilities of absorbing a photon, generating a continuum electron, or promoting the electron into a bound excited state furthermore exhibit a phase shift with respect to the pump-probe delay. Since the detection of He^+ ions is only sensitive to processes leading to the ionization of an atom, no complete information on the relative phases and amplitudes of the absorption of photons can be derived from such a measurement. Rivière et al. introduce a minimal analytical model for the total photon absorption probabilities based on the strong-field approximation [168]. They find that the replicated EWP can be factorized into two terms: A term that depends on the number of IR-cycles the APT spans (which is a comb-function and acts as a momentum filter) and a term that depends on the number of attosecond pulses per laser cycle. In their model, the modulation of the absorption probability is assigned exclusively to the interference of electron wavepackets. An alternative theoretical description based on Floquet theory arrives at similar conclusions [169]. It directly addresses the differences in the behavior with argon and helium target gas and compares single attosecond pulse to APT excitation.

Two main observations in the ion yield experiment were considered indicative for the transiently bound wavepacket interference model. First, the modulation contrast was considerably higher than that expected for a single attosecond excitation pulse. Calculations showed that the interferences enhance this contrast by an order of magnitude for an APT with a 10 fs FWHM envelope and bring it to the level observed experimentally. Second, the strongly directional emission seen in the two-dimensional photoelectron momentum distribution along the direction of the IR field polarization was found to be consistent with the fact that the electrons are ejected preferentially along the directions where the potential barrier is lowered by the IR field. For electrons ionized well above the ionization potential, such directionality is not observed as can be verified by replacing the helium target gas with argon.

5.1.2   Results and discussion
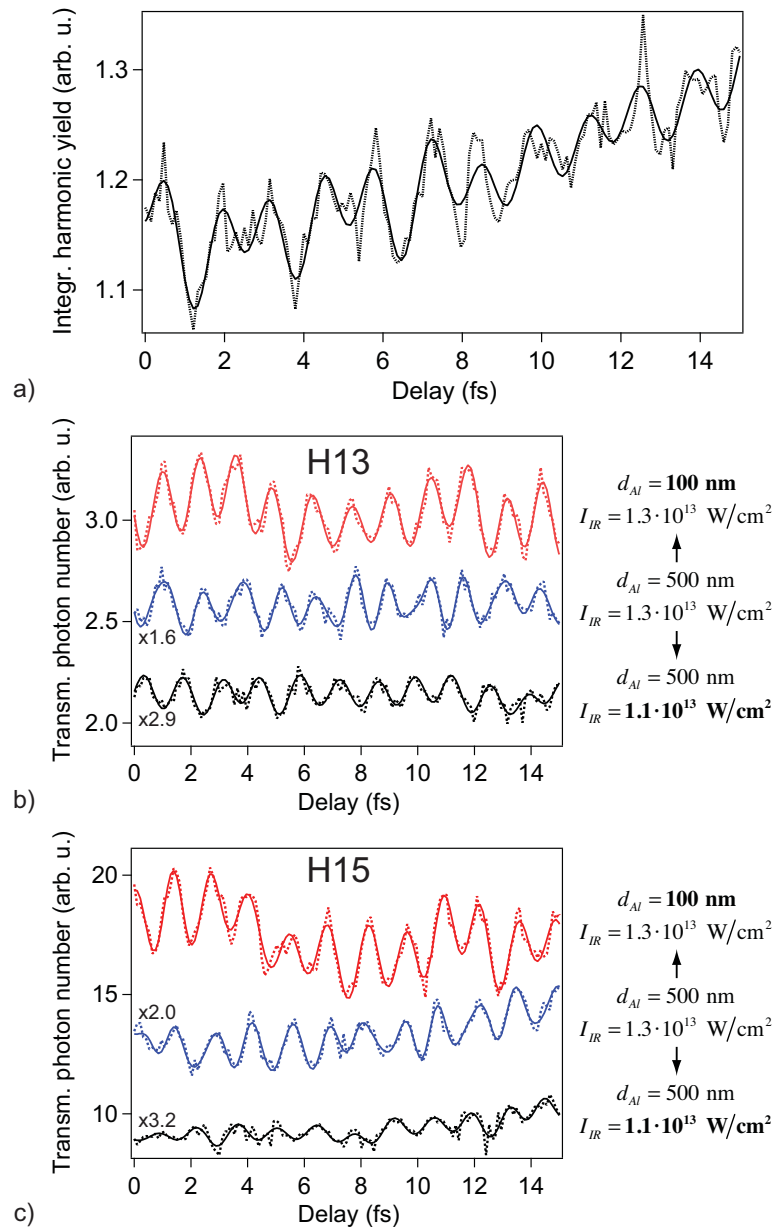
Figure 5.3: Transmitted harmonic photon yields with respect to APT-IR-pump-probe delay. All harmonics are modulated at twice the fundamental laser frequency. These modulations are robust against spectral integration (a), which is expected from the He^{+} yield measurements by Johnsson et al. [166]. In the spectrally resolved data, it can be seen that the phase of the modulations on individual harmonics remains unchanged for different thicknesses of the Al-filter used (b, harmonic 13; c, harmonic 15). The phase, however, sensitively reacts to a change in the IR intensity. The dotted lines correspond to the measured data, the solid lines to a signal smoothed by Fourier low-pass filtering. The black and blue traces in b) and c) have been rescaled for easier visual comparison as indicated next to the corresponding trace.

With transient absorption we can now examine the impact of the IR-field on the absorption probability of the XUV photons and thus the influence of a time-dependence in the transition operator much more completely. Transient absorption allows us to see which photon energies get absorbed to what extent and at which APT-IR delays. Figure 5.3 shows the transmitted HHG photons as a function of delay. It can be clearly seen that the transmission (or absorption) of the harmonics is modulated at twice the infrared fundamental frequency. This modulation survives spectral integration (see Figure 5.3a) even though the individual modulations exhibit a phase shift with respect to each other. This must be the case because the total absorption is directly related to the ion yield detected in the experiment by Johnsson et al.. However, the relative phases seen in the spectrally resolved case yield additional information allowing the verification of the proposed theoretical models. Figure 5.3b) and c) show the modulations on the individual harmonics 13 and 15, respectively. The plotted values were each detected by a single CCD column located on the respective harmonic spectral peak. The pixel columns cover approximately 20 meV photon energy in width. From the simple picture shown in Figure 5.2 (as well as the analytical model and the Floquet-theory based approach), we can derive the following predictions for the interference of subsequent wavepackets: The temporal phase of each pulse in the APT directly maps onto the EWP upon its birth. The so-called "atto-chirp" [140] describes phase contributions that are identical for all pulses in the train. The interference of wavepackets generated by subsequent attosecond pulses should thus not depend on the atto-chirp. On the other hand, the dominant influence on the interference of a previous wavepacket with a newly created one should come from the phase accumulated on its excursion into the continuum. The phase picked up by the EWP during the acceleration in the electric field of the infrared pulse depends sensitively on the laser intensity [142]. Any change in the interference conditions between EWP from subsequent attosecond pulses should manifest itself in a change in the observed absorption modulation pattern.

In order to test the first prediction, we varied the thickness of our aluminum filters used to separate the APT from its generating infrared field. Varying the filter thickness by hundreds of nanometers is known to change in good approximation only the spectral phase difference between neighboring harmonics [165]. In the time domain, this harmonic-to-harmonic phase variation corresponds to the atto-chirp. Larger amounts of dispersion that would lead to non-negligible pulse-to-pulse phase variation were not investigated in our experiments. Figure 5.3b) and c) compare the transmitted

photon yield for harmonics 13 and 15 as a function of APT-to-IR delay for aluminum filter thicknesses of 500 nm and 100 nm. Both data sets were recorded at identical infrared intensity of with a step size of 107 as over 1400 steps and an exposure time of 50 ms and 10 ms per spectrum, respectively. For the 500 nm case, harmonics 13 and 17 are oscillating in phase (phase difference 0.1 rad), whereas harmonics 13 and 15 are shifted by 2.5 rad with respect to each other. If the filter is replaced by the 100 nm version, then the relative phase between harmonics 13 and 17 amounts to 0.2 rad, while a phase shift of 2.2 rad is observed between harmonics 13 and 15. The differences between these two cases are within experimental uncertainty as was verified by repeating the measurement with the 500 nm filter after the 100 nm filter run. The phase values have been extracted from the measured data by Fourier analysis and were found to be reproducible within 0.5 rad. For comparison, the linear dispersion of Al changes the spectral phase difference between harmonics 13 and 15 of the incoming APT by 1.3 rad and between harmonics 13 and 17 by 1.74 rad. The observation of negligible phase change in the absorption modulations for significant filter thickness change is consistent with the theoretical pictures outlined above.

In order to verify the predicted sensitivity of the modulations towards IR intensity changes, we performed one measurement run with the 500 nm aluminum filter but at a lower intensity of $1.1 \cdot 10^{13}$ W/cm^2 (black lines in Figure 5.3b) and c)). This time, even with the intensity being lowered by merely 15%, the relative phase between the transmitted photon yield modulations changes considerably by an amount well beyond experimental uncertainty. The relative phase between harmonics 13 and 17 is now determined to be 1.6 rad, while the modulations on harmonic 13 and 15 are shifted by 3.0 rad with respect to each other. As expected qualitatively from the theoretical models and the schematic picture in Figure 5.2, the infrared laser intensity has a strong effect on the electron wavepacket interference conditions. This is due to the fact that the interference occurs between an EWP having accumulated phase during acceleration in the IR field and an EWP having just been excited from the ground state by the following attosecond pulse. The relative phase is thus always being governed by the contribution from the IR driven EWP excursion. The atto-chirp phase contribution, on the other hand, is identical for each EWP and thus cancels upon interference.

Our experiment thus provides strong evidence for the transiently bound wavepacket interference picture and is in agreement with all three theoretical descrip-

tions developed so far. This makes this experiment the first all-optical observation of attosecond wavepacket interferences. Transient absorption offers a valuable alternative view of the physical system as compared to photo-ion or photo-electron detection. In addition, we find that the sensitive optical detectors allow for rapid data acquisition with good signal-to noise ratio. The insensitivity towards space charge effects enables us to work with higher target gas densities for an additional boost in signal levels. It needs to be noted, however, that the theoretical frameworks needed for the calculation of transmitted photon spectra in strong-field laser-matter interactions do not yet exist – in particularly not in a regime close to the ionization threshold where many traditional approximations break down.

5.1.3   Conclusion

We have used attosecond transient absorption of an APT in the presence of a moderately strong infrared field in a dense helium target to investigate the interference of transiently bound electron wavepackets. Our measurements provide more complete insight into the influence of the ultrafast perturbation of XUV transitions in an atom irradiated by an IR-field. We find that the relative phases between the rapid modulations of the transmitted photon yield at harmonics 13, 15, and 17 sensitively depend on the infrared intensity but remain unchanged within experimental uncertainty for changing atto-chirp of the APT. By changing the IR-APT delay and the IR intensity, the relative absorption of the individual harmonics can be controlled with high precision. This can be considered a form of absorptive pulse shaping of the original APT. Furthermore, our experiment demonstrates that transient absorption can provide more physical insight into the attosecond dynamics of suitable systems compared to the more traditional electron or ion detection. With improved theoretical approaches for the modeling of the optical response of physical systems on this time scale, it will become possible to extract even more information from such data and to obtain a better quantitative understanding of the processes under investigation.

5.2   Femtosecond emission structures and outlook

The rapid modulations discussed in Section 5.1 represent only one aspect of the rich dynamics observed in our transient absorption data taken in an optically dense helium

target. While the interpretation of all these features is still a work in progress we briefly present and discuss some of the phenomena seen in our experiments below.
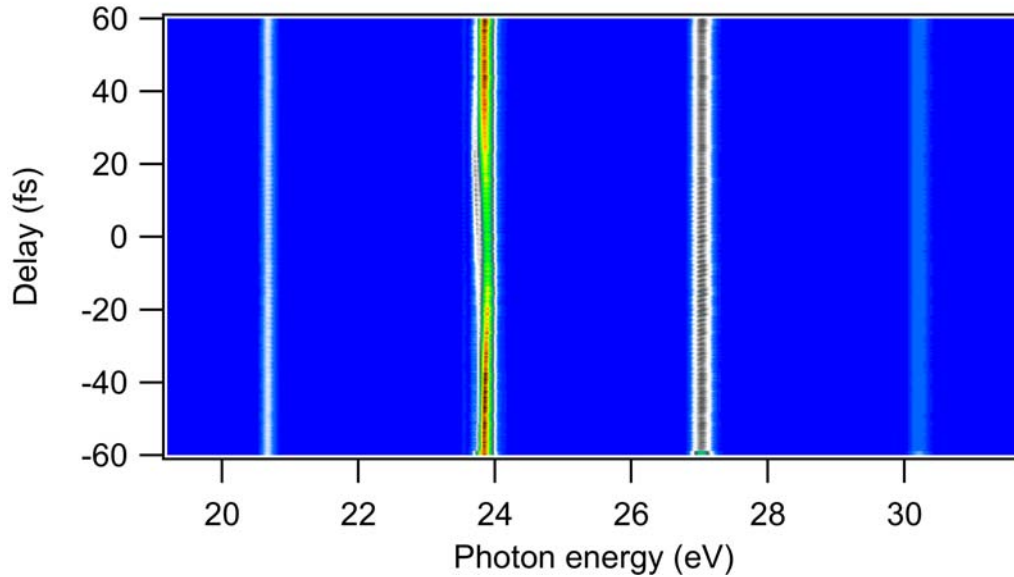
Figure 5.4: Transmitted XUV spectra as a function of APT-IR delay. The Figure shows harmonic orders 13, 15, 17, and 19.

Figure 5.4 shows the transmitted APT harmonics as a function of delay with respect to the IR pulse. The rapid modulations discussed in Section 5.1 can be seen as horizontal stripes. Upon closer inspection, one sees that these stripes are slightly tilted and that the tilt has an opposite sign above or below the static ionization threshold of helium located at 24.6 eV (best seen when comparing harmonics 13 and 17). The origin of this tilt is unknown. It might be attributed to the slight detuning between the APT periodicity and the IR oscillation period due to the spectral blue-shift experienced by the driving laser during APT generation in xenon.

The structure of the transmitted harmonic 15 also shows a clear asymmetry with respect to pump probe delay and with respect to the harmonic center frequency. In the following, we will make use of the high spectral resolution of our experiment and have a closer look at this particular harmonic.

5.2.1   Zooming in on harmonic 15

Harmonic 15 is located the closest to the ionization threshold of helium, less than one infrared photon energy away. It is also the only constituent of the APT that overlaps in its spectral wings with internal states of helium.
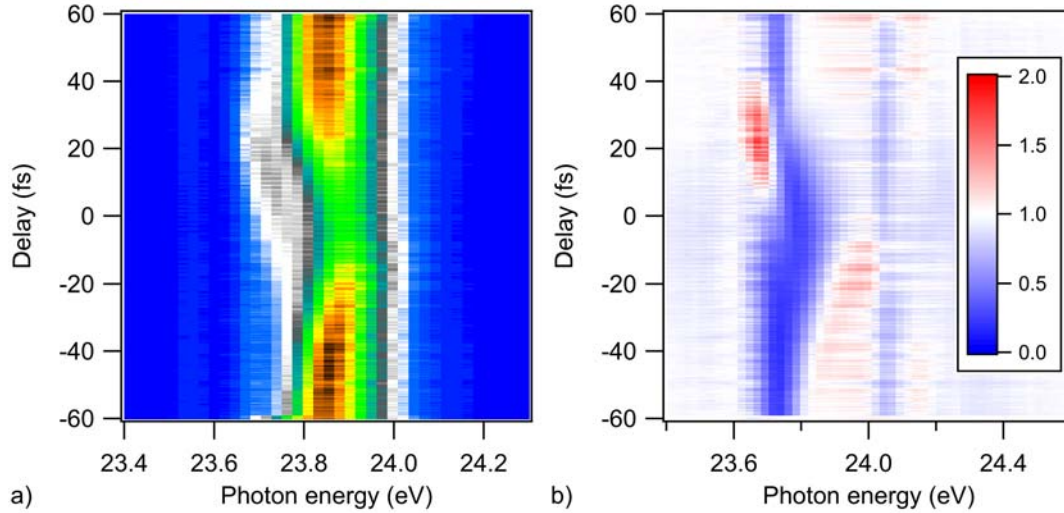
Figure 5.5: Transmitted XUV spectrum of harmonic 15 as a function of delay. Positive delays correspond to the XUV pulse arriving before the IR pulse. a) The recorded signal is asymmetric with respect to delay and center frequency (linear color scale). b) Signal with helium divided by signal without helium. The *1s4p* and the *1s5p* levels located in the spectral wings of harmonic 15 can be identified as the vertical blue lines. At a delay of about 20 fs, a net emission of photons is observed below the *1s4p* resonance.

A close-up of the recorded XUV spectra around harmonic 15 is shown in Figure 5.5. The *1s4p* and the *1s5p* levels are energetically located in the spectral wings on both sides of harmonic 15. While they cannot be easily identified in the direct signal shown in Figure 5.5a), they become apparent once we divide the recorded signal by a reference signal taken without helium (Figure 5.5b)). They manifest themselves as the vertical blue lines in this figure. We concentrate our discussion on the *1s4p* level since this spectral section of the data exhibits a better signal-to-noise ratio than the section around the *1s5p* level. In the region of overlap between the IR pulse and the APT, one clearly sees how the IR radiation induces a level shift and broadening of the resonance.

When the APT arrives ~20 fs before the IR pulse, a significant emission of photons occurs directly below the field-free *1s4p* level. In a narrow frequency band we

observe twice as many photons exiting from the helium target than were initially sent in. The origin of this emission feature is still unknown. The simplest possible explanation is that it is a result from spectral redistribution due to cross-phase modulation between the XUV und the IR. In the proximity of the resonance, the nonlinear coupling between the interacting waves could potentially be rather high. Further investigation is needed to explore the plausibility of this idea. Less pronounced emission also seems to occur at negative delays between 23.8 eV and 24 eV.

We know, however, the origin of the asymmetry along the delay axis from the solution of the time-dependent Schroedinger equation (performed by P. Rivière at MPIPKS Dresden). If the helium atom is in its ground state, the IR is too weak to induce any strong-field or even multi-photon processes. The XUV, on the other hand, is also too weak to induce any nonlinear optical process. As a result, only XUV single-photon transitions from the ground state to *p*-levels of helium will occur. Now, if the APT comes first, the *p*-levels will be populated when the IR pulse arrives. The IR cannot be considered a weak pulse anymore for the excited energy levels close to the ionization threshold. For the excited *p*-levels, the IR can induce multi-photon interactions, transferring population via the continuum into the *f*-levels. This process only occurs for one particular order of the two pulses and thus explains the observed asymmetry with respect to delay.

Clearly more work is needed to fully understand all the features observed in our transient absorption experiments. However, the rich details in our data set demonstrate the strengths of attosecond transient absorption spectroscopy. In a fraction of the time needed for a traditional experiment detecting photo-electrons or ions, we acquired data with excellent signal-to-noise ratio and without compromise on temporal and spectral resolution. Most theoretical tools in attosecond and strong-field science are geared towards computing ionization yields rather than the optical properties of a particular interaction. A significant effort is therefore also needed towards developing the new theoretical frameworks for transient absorption in the attosecond domain.

Chapter 6

Conclusion and outlook

We have presented a new long-wavelength source for strong-field physics in Chapter 2, an investigation of fundamental processes underlying attosecond pulse generation and high-order harmonic generation in general in Chapter 3, and in Chapter 5 we discussed the application of a new attosecond measurement method to time-resolved studies in basic atomic physics. In the following we will put this work into a bigger context and try to predict future trends in these areas.

Ti:sapphire amplifier systems operating at a center wavelength around 800 nm are the traditional workhorse in strong-field and attosecond physics. As strong-field processes are inherently governed by the electric field of the driving laser pulse rather than its intensity profile, the periodicity of the field's oscillations can be an important parameter. For example, it determines the excursion time of a field-ionized electron and its recollision energy if it's on a recolliding trajectory. With moving to longer and longer driving wavelengths, excursion times and thereby the acceleration phase can become long enough for the electron to reach relativistic velocities – provided that the laser intensity is sufficiently high. This is just one aspect that shows that the driving wavelength is of crucial importance for strong-field processes. It is therefore of fundamental interest to explore other wavelength regimes than just the Ti:sapphire spectral region for a better understanding of strong-field physics. A few groups have used parametric sources to investigate, for example, the scaling of above-threshold ionization electron spectra, high-order harmonic generation or – more specifically – the harmonic cut-off [68, 170-173]. The parametric amplifiers used in those experimental studies are all pumped by Ti:sapphire amplifier systems. This immediately implies that these infrared

sources were all limited in repetition rate by the thermal limitations of the primary Ti:sapphire system. And furthermore, such systems are bulky and expensive.

We demonstrated an alternative approach based on commercial solid-state and fiber laser technology in Chapter 2. While our mid-infrared OPCPA cannot yet compete with state-of-the-art OPA pulses from Ti:sapphire based systems in terms of pulse energy and pulse duration (see, e.g., [174, 175] for energetic pulses in the near-IR or [51, 176] for short pulses in the mid-IR) we expect to close the gap further in the future. In particular if we restrict ourselves to femtosecond pulses in the 2.5 to 5 µm spectral region as shown in Figure 2.1 then our pulse energy is already close to the best Ti:sapphire results and the average power sets a new record. We do not yet hit any fundamental limits with our concept, so further scaling of its performance should be possible. The next steps will be to fully exploit the potential offered by the APPLN gain medium. For this, we will have to broaden our seed spectra – e.g., by spectral broadening in PPLN waveguides [116]. We expect a considerable shortening of the output pulses by combining the larger seed bandwidth with fine dispersion control using a spatial light modulator in the seed beam. A bigger challenge will be the implementation of the active CEP-stabilization that is required with the new seed concept. However, no fundamental roadblocks are expected.

Beyond these rather short-term goals and first applications of the system to strong-field physics experiments, what are possible future directions? The engineerability of APPLN may allow for phase and maybe even pulse shaping using the nonlinear medium directly [114]. Furthermore, it should be rather straightforward to transfer our concept to other emission wavelengths. Further scaling of the repetition rate becomes possible with the latest advances in high power thin-disk lasers [84, 85]. In terms of applications, large interest may also come from the field of multi-dimensional molecular spectroscopy. For this application, sub-100-fs pulses with a pulse energy of few µJ in the mid-infrared are needed [120]. It remains to be seen, however, what the optimum pulse repetition rate is, as high average powers may thermally destabilize the molecules under investigation [120]. On the other hand, simpler and more compact laser sources may benefit the commercialization of multi-dimensional molecular spectroscopy.

The development of our OPCPA system addresses the progress and evolution of the primary lasers sources used in high-field and attosecond science. The discussion in Chapter 3 shows on the other hand that also the sources of attosecond pulses and

high-order harmonic radiation in general need further attention. The process of high-order harmonic generation remains a playground for fundamental research even 25 years after its discovery [20, 21]. Fortunately, this lack of understanding of certain basic aspects does not prevent the application of HHG in many different areas. With regard to possible applications of the quantum-path interferences reported in Chapter 3 it remains to be seen whether they can be exploited for the characterization of the full harmonic dipole. Can the phase sensitivity of the interference process be used as a probe? As the short and the long trajectory electrons interact differently with their environment, such difference should show up in the phase encoded in the observed harmonic yield fringes. Our analysis has also shown that we exert very fine control on the electron trajectories (in particular on their relative timing) with our intensity "knob". Can this control be put to use in a strong-field control experiment?

Besides our work on the sources, we also introduced transient absorption with attosecond pulse trains as a new experimental technique in attosecond science [26-28]. We applied the method to a simple atomic species and could report the first all-optical observation of attosecond wave-packet interferences [28]. As we stated in Chapter 5, further work is needed to explain all the rich structures manifesting themselves in our data. In particular, theory needs to catch up with these recent experimental developments. Only little theory has been performed so far on the optical response of systems in strong-field and attosecond science (see, e.g., [168, 177]). Independent of this, we expect attosecond transient absorption spectroscopy to establish itself as an experimental tool in attosecond research with applications to many different systems of varying complexity.

The need for further improvement of sources and techniques for attosecond science is evident. The field will only be able of sustainable growth if the technology can be simplified and be made more robust. Attosecond time-resolved spectroscopy will only have a lasting impact beyond its own community if it can be applied to more general and ultimately more complex systems. It is our hope that the work presented here represents at least a small enabling step into this direction.

References

1.   F. Remacle, and R. D. Levine, "An electronic time scale in chemistry," Proc. Nat. Acad. Science **103**, 6793-6798 (2006).

2.   M. F. Kling, C. Siedschlag, A. J. Verhoef, J. I. Khan, M. Schultze, T. Uphues, Y. Ni, M. Uiberacker, M. Drescher, F. Krausz, and M. J. J. Vrakking, "Control of Electron Localization in Molecular Dissociation," Science **312**, 246-248 (2006).

3.   A. L. Cavalieri, N. Müller, T. Uphues, V. S. Yakovlev, A. Baltuska, B. Horvath, B. Schmidt, L. Blümel, R. Holzwarth, S. Hendel, M. Drescher, U. Kleineberg, P. M. Echenique, R. Kienberger, F. Krausz, and U. Heinzmann, "Attosecond spectroscopy in condensed matter," Nature **449**, 1029-1032 (2007).

4.   S. Roth, D. Leuenberger, J. Osterwalder, J. E. Dahl, R. M. K. Carlson, B. A. Tkachenko, A. A. Fokin, P. R. Schreiner, and M. Hengsberger, "Negative-electron-affinity diamondoid monolayers as high-brilliance source for ultrashort electron pulses " Chem. Phys. Lett. **495**, 102-108 (2010).

5.   E. Goulielmakis, M. Uiberacker, R. Kienberger, A. Baltuska, V. Yakovlev, A. Scrinzi, T. Westerwalbesloh, U. Kleineberg, U. Heinzmann, M. Drescher, and F. Krausz, "Direct Measurement of Light Waves," Science **305**, 1267-1269 (2004).

6.   M. Drescher, M. Hentschel, R. Kienberger, M. Uiberacker, V. Yakovlev, A. Scrinzi, T. Westerwalbesloh, U. Kleineberg, U. Heinzmann, and F. Krausz, "Time-resolved atomic inner-shell spectroscopy," Nature **419**, 803-807 (2002).

7.   M. Uiberacker, T. Uphues, M. Schultze, A. J. Verhoef, V. Yakovlev, M. F. Kling, J. Rauschenberger, N. M. Kabachnik, H. Schröder, M. Lezius, K. L. Kompa, H.-G. Muller, M. J. J. Vrakking, S. Hendel, U. Kleineberg, U. Heinzmann, M. Drescher, and F. Krausz, "Attosecond real-time observation of electron tunnelling in atoms," Nature **446**, 627-632 (2007).

8.   M. Schultze, M. Fiess, N. Karpowicz, J. Gagnon, M. Korbman, M. Hofstetter, S. Neppl, A. L. Cavalieri, Y. Komninos, T. Mercouris, C. A. Nicolaides, R. Pazourek, S. Nagele, J. Feist, J. Burgdorfer, A. M. Azzeer, R. Ernstorfer, R. Kienberger, U. Kleineberg, E. Goulielmakis, F. Krausz, and V. S. Yakovlev, "Delay in Photoemission," Science **328**, 1658-1662 (2010).

9.   K. Klünder, J. M. Dahlström, M. Gisselbrecht, T. Fordell, M. Swoboda, D. Guenot, P. Johnsson, J. Caillat, J. Mauritsson, A. Maquet, R. Taïeb, and A. L'Huillier, "Probing Single-Photon Ionization on the Attosecond Time Scale," Phys. Rev. Lett. **106** (2011).

10.   P. Eckle, M. Smolarski, P. Schlup, J. Biegert, A. Staudte, M. Schöffler, H. G. Muller, R. Dörner, and U. Keller, "Attosecond Angular Streaking," Nat. Phys. **4**, 565-570 (2008).

11.   P. Eckle, A. Pfeiffer, C. Cirelli, A. Staudte, R. Dörner, H. G. Muller, M. Büttiker, and U. Keller, "Attosecond ionization and tunneling delay time measurements in helium," Science **322**, 1525-1529 (2008).

12. T. Remetter, P. Johnsson, J. Mauritsson, K. Varju, Y. Ni, F. Lépine, E. Gustafsson, M. Kling, J. Khan, R. Lopez-Martens, K. J. Schafer, M. J. J. Vrakking, and A. l'Huillier, "Attosecond electron wave packet interferometry," Nature Physics **2**, 323-326 (2006).

13. J. Mauritsson, P. Johnsson, E. Mansten, M. Swoboda, T. Ruchon, A. L'Huillier, and K. J. Schafer, "Coherent Electron Scattering Captured by an Attosecond Quantum Stroboscope," Phys. Rev. Lett. **100**, 073003 (2008).

14. S. Baker, J. S. Robinson, C. A. Haworth, H. Teng, R. A. Smith, C. C. Chirilă, M. Lein, J. W. G. Tisch, and J. P. Marangos, "Probing Proton Dynamics in Molecules on an Attosecond Time Scale," Science **312**, 424-427 (2006).

15. M. Charbonneau-Lefort, B. Afeyan, and M. M. Fejer, "Optical parametric amplifiers using chirped quasi-phase-matching gratings I: practical design formulas," J. Opt. Soc. Am. B **25**, 463-480 (2008).

16. M. Charbonneau-Lefort, B. Afeyan, and M. M. Fejer, "Optical parametric amplifiers using nonuniform quasi-phase-matched gratings. II. Space-time evolution of light pulses," J. Opt. Soc. Am. B **25**, 680-697 (2008).

17. M. Charbonneau-Lefort, B. Afeyan, and M. M. Fejer, "Competing collinear and noncollinear interactions in chirped quasi-phase-matched optical parametric amplifiers," J. Opt. Soc. Am. B **25**, 1402-1413 (2008).

18. C. Heese, C. R. Phillips, L. Gallmann, M. M. Fejer, and U. Keller, "Ultrabroadband, highly flexible amplifier for ultrashort midinfrared laser pulses based on aperiodically poled $Mg:LiNbO_3$," Opt. Lett. **35**, 2340-2342 (2010).

19. C. R. Phillips, and M. M. Fejer, "Efficiency and phase of optical parametric amplification in chirped quasi-phase-matched gratings," Opt. Lett. **35**, 3093-3095 (2010).

20. A. McPherson, G. Gibson, H. Jara, U. Johann, T. S. Luk, I. A. McIntyre, K. Boyer, and C. K. Rhodes, "Studies of multiphoton production of vacuum-ultraviolet radiation in the rare gases," J. Opt. Soc. Am. B **4**, 595-601 (1987).

21. M. Ferray, A. L'Huillier, X. F. Li, L. A. Lompré, G. Mainfray, and C. Manus, "Multiple-harmonic conversion of 1064 nm radiation in rare gases," J. Phys. B: At. Mol. Opt. Phys. **21**, L31-L35 (1988).

22. J. Itatani, J. Levesque, D. Zeidler, H. Niikura, H. Pépin, J. C. Kieffer, P. B. Corkum, and D. M. Villeneuve, "Tomographic imaging of molecular orbitals," Nature **432**, 867-871 (2004).

23. G. Genoud, O. Guilbaud, E. Mengotti, S. G. Petterson, E. Georgiadou, E. Pourtal, C. G. Wahlstrom, and A. L'Huillier, "XUV digital in-line holography using high-order harmonics," Appl. Phys. B **90**, 533-538 (2008).

24. P. B. Corkum, "Plasma Perspective on Strong-Field Multiphoton Ionization," Phys. Rev. Lett. **71**, 1994-1997 (1993).

25.   P. Salières, B. Carré, L. L. Déroff, F. Grasborn, G. G. Paulus, H. Walther, R. Kopold, W. Becker, D. B. Miloſevic, A. Sanpera, and M. Lewenstein, "Feynman's path-integral approach for intense-laser-atom interactions," Science **292 (5)**, 902 (2001).

26.   E. Goulielmakis, Z.-H. Loh, A. Wirth, R. Santra, N. Rohringer, V. S. Yakovlev, S. Zherebtsov, T. Pfeifer, A. M. Azzeer, M. F. Kling, S. R. Leone, and F. Krausz, "Real-time observation of valence electron motion," Nature **466**, 739-743 (2010).

27.   H. Wang, M. Chini, S. Chen, C.-H. Zhang, F. He, Y. Cheng, Y. Wu, U. Thumm, and Z. Chang, "Attosecond Time-Resolved Autoionization of Argon," Phys. Rev. Lett. **105**, 143002 (2010).

28.   M. Holler, F. Schapper, L. Gallmann, and U. Keller, "Attosecond ElectronWave-Packet Interference Observed by Transient Absorption," Phys. Rev. Lett. **106**, 123601 (2011).

29.   A. H. Zewail, "Femtochemistry: atomic-scale dynamics of chemical bond," J. Phys. Chem. A **104**, 5660-5694 (2000).

30.   J. L. Hall, "Nobel Lecture: Defining and measuring optical frequencies," Rev. Mod. Phys. **78**, 1279-1295 (2006).

31.   T. W. Hänsch, "Nobel Lecture: Passion for precision," Rev. Mod. Phys. **78**, 1297-1308 (2006).

32.   J. L. Krause, K. J. Schafer, and K. C. Kulander, "High-order harmonic-generation from atoms and ions in the high-intensity regime," Phys. Rev. Lett. **68**, 3535-3538 (1992).

33.   M. Ghotbi, M. Ebrahim-Zadeh, V. Petrov, P. Tzankov, and F. Noack, "Efficient 1 kHz femtosecond optical parametric amplification in BiB3O6 pumped at 800 nm," Opt. Express **14**, 10621-10626 (2006).

34.   C. J. Fecko, J. J. Loparo, and A. Tokmakoff, "Generation of 45 femtosecond pulses at 3 μm with a KNbO3 optical parametric amplifier," Opt. Commun. **241**, 521-528 (2004).

35.   J.-C. Wang, and J.-K. Wang, "Experimental and theoretical analysis of whitelight seeded, collinear phase-matching, femtosecond optical parametric amplifiers," J. Opt. Soc. Am. B **21**, 45-56 (2004).

36.   H. Maekawa, K. Tominaga, and D. Podenas, "Generation of 55 fs-Mid-Infrared Pulses with a 300 cm−1-Spectral Width and μJ-Pulse Energy," Jpn. J. Appl. Phys. **41**, 329-331 (2002).

37.   T. Witte, D. Zeidler, D. Proch, K. L. Kompa, and M. Motzkus, "Programmable amplitude- and phase-modulated femtosecond laser pulses in the mid-infrared," Opt. Lett. **27**, 131-133 (2002).

38.   R. A. Kaindl, M. Wurm, K. Reimann, P. Hamm, A. M. Weiner, and M. Woerner, "Generation, shaping, and characterization of intense femtosecond pulses tunable from 3 to 20 μm," J. Opt. Soc. Am. B **17**, 2086-2094 (2000).

39.   F. Rotermund, V. Petrov, and F. Noack, "Laser-diode-seeded single and double stage femtosecond optical parametric amplification in the mid-infrared," Opt. Quantum Electron. **32**, 1057-1067 (2000).

40. G. M. Gale, G. Gallot, F. Hache, and R. Sander, "Generation of intense highly coherent femtosecond pulses in the mid infrared," Opt. Lett. **22**, 1253-1255 (1997).

41. U. Emmerichs, S. Woutersen, and H. J. Bakker, "Generation of intense femtosecond optical pulses near 3 µm with a kilohertz repetition rate," J. Opt. Soc. Am. B **14**, 1480-1483 (1997).

42. V. Petrov, and F. Noack, "Mid-infrared femtosecond optical parametric amplification in potassium niobate," Opt. Lett. **21**, 1576-1578 (1996).

43. F. Seifert, V. Petrov, and M. Woerner, "Solid-state laser system for the generation of midinfrared femtosecond pulses tunable from 3.3 to 10 µm," Opt. Lett. **19**, 2009-2011 (1994).

44. B. Golubovic, and M. K. Reed, "All-solid-state generation of 100-kHz tunable mid-infrared 50-fs pulses in type I and type II AgGaS2," Opt. Lett. **23**, 1760-1762 (1998).

45. J. A. Gruetzmacher, and N. F. Scherer, "Few-cycle mid-infrared pulse generation, characterization, and coherent propagation in optically dense media," Rev. Sci. Instrum. **73**, 2227-2236 (2002).

46. G. R. Holtom, R. A. Crowell, and X. S. Xie, "High-repetition-rate femtosecond optical parametric oscillator–amplifier system near 3 µm," J. Opt. Soc. Am. B **12**, 1723-1731 (1995).

47. U. Emmerichs, H. J. Bakker, and H. Kurz, "Generation of high-repetition rate femtosecond pulses tunable in the mid-infrared," Opt. Commun. **111**, 497-501 (1994).

48. D. Strickland, and G. Mourou, "Compression of amplified chirped optical pulses," Optics Communications **56**, 219-221 (1985).

49. T. Fuji, N. Ishii, C. Y. Teisset, X. Gu, T. Metzger, A. Baltuška, N. Forget, D. Kaplan, A. Galvanauskas, and F. Krausz, "Parametric amplification of few-cycle carrier-envelope phase-stable pulses at 2.1 µm," Opt. Lett. **31**, 1103-1105 (2006).

50. C. P. Hauri, R. B. Lopez-Matens, C. I. Blaga, K. D. Schultz, J. Cryan, R. Chirla, P. Colosimo, G. Doumy, A. M. March, C. Roedig, E. Sistrunk, J. Tate, J. Wheeler, and L. F. DiMauro, "Intense self-compressed, self-phase-stabilized few-cycle pulses at 2 µm from an optical filament," Opt. Lett. **32**, 868-870 (2007).

51. D. Brida, C. Manzoni, G. Cirmi, M. Marangoni, S. D. Silvestri, and G. Cerullo, "Generation of broadband mid-infrared pulses from an optical parametric amplifier," Opt. Express **15**, 15035-15040 (2007).

52. J. Rothhardt, S. Hädrich, D. N. Schimpf, J. Limpert, and A. Tünnermann, "High repetition rate fiber amplifier pumped sub-20 fs optical parametric amplifier," Opt. Express **15**, 16729-16736 (2007).

53. A. Steinmann, A. Killi, G. Palmer, T. Binhammer, and U. Morgner, "Generation of few-cycle pulses directly from a MHz-NOPA," Opt. Express **14**, 10627-10630 (2006).

54. M. Marangoni, R. Osellame, R. Ramponi, G. Cerullo, A. Steinmann, and U. Morgner, "Near-infrared optical parametric amplifier at 1 MHz directly pumped by a femtosecond oscillator," Opt. Lett. **32**, 1489-1491 (2007).

55. R. Laenen, K. Simeonidis, and A. Lauberreau, "Parametric generation of synchronized, independently tunable subpicosecond pulses in the midinfrared with adjustable pulse duration," J. Opt. Soc. Am. B **15**, 1213-1217 (1998).

56. A. Dubietis, G. Jonusauskas, and A. Piskarskas, "Powerful femtosecond pulse generation by chirped and strechted pulse parametric amplification in BBO crystal," Opt. Communications **88**, 437-440 (1992).

57. C. Erny, C. Heese, M. Haag, L. Gallmann, and U. Keller, "High-repetition-rate optical parametric chirped-pulse amplifier producing 1-µJ, sub-100-fs pulses in the mid-infrared," Opt. Express **17**, 1340-1345 (2009).

58. C. Erny, L. Gallmann, and U. Keller, "High-Repetition-Rate Femtosecond Optical Parametric Chirped-Pulse Amplifier in the Mid-Infrared," Appl. Phys. B **96**, 257-269 (2009).

59. O. Chalus, P. K. Bates, M. Smolarski, and J. Biegert, "Mid-IR short-pulse OPCPA with micro-Joule energy at 100 kHz," Opt. Express **17**, 3587-3594 (2009).

60. F. Tauser, F. Adler, and A. Leitenstorfer, "Widely tunable sub-30-fs pulses from a compact erbium-doped-fiber source," Opt. Lett. **29**, 516-518 (2004).

61. C. Erny, K. Moutzouris, J. Biegert, D. Kühlke, F. Adler, A. Leitenstorfer, and U. Keller, "Mid-infrared difference-frequency generation of ultrashort pulses tunable between 3.2 and 4.8 µm from a compact fiber source," Opt. Lett. **32**, 1138-1140 (2007).

62. C. Heese, A. E. Oehler, L. Gallmann, and U. Keller, "High-energy picosecond Nd:YVO$_4$ slab amplifier for OPCPA pumping," Appl. Phys. B, DOI 10.1007/s00340-00011-04509-00340 (2011).

63. A. Dubietis, R. Butkus, and A. P. Piskarskas, "Trends in Chirped Pulse Optical Parametric Amplification," IEEE J. Sel. Top. Quantum Electron. **12**, 163-172 (2006).

64. P. Schlup, J. Biegert, C. P. Hauri, G. Arisholm, and U. Keller, "Design of a sub-13-fs, multi-gigawatt optical parametric amplification system," Appl. Phys. B **79**, 285-288 (2004).

65. R. T. Zinkstok, S. Witte, W. Hogervorst, and K. S. E. Eikema, "High-power parametric amplification of 11.8-fs laser pulses with carrier-envelope phase control," Opt. Lett. **30**, 78-80 (2005).

66. N. Ishii, L. Turi, V. S. Yakovlev, T. Fuji, F. Krausz, A. Baltuska, R. Butkus, G. Veitas, V. Smilgevicius, R. Danielius, and A. Piskarskas, "Multimillijoule chirped parametric amplification of few-cycle pulses," Opt. Lett. **30**, 567-569 (2005).

67. S. Witte, R. T. Zinkstok, W. Hogervorst, and K. W. E. Eikema, "Generation of few-cycle terawatt light pulses using optical parametric chirped pulse amplification," Opt. Express **13**, 4903-4908 (2005).

68. P. Colosimo, G. Doumy, C. I. Blaga, J. Wheeler, C. Hauri, F. Catoire, J. Tate, R. Chirla, A. M. March, G. G. Paulus, H. G. Muller, P. Agostini, and L. F. DiMauro, "Scaling strong-field interactions towards the classical limit," Nature Physics **4**, 386-389 (2008).

69. V. Pyragaite, A. Stabinis, R. Butkus, R. Antipenkov, and A. Varanavicius, "Parametric amplification of chirped optical pulses under pump depletion," Opt. Commun. **283**, 1144-1151 (2010).

70. J. Dong, K. Ueda, A. Shirakawa, H. Yagi, and T. Yanagitani, "Composite Yb:YAG/Cr4+:YAG ceramics picosecond microchip lasers," Opt. Express **15** (2007).

71. A. Agnesi, L. Carra, P. Dallocchio, F. Pirzio, G. Reali, A. Tomaselli, D. Scarpa, and C. Vacchi, "210-mu J Picosecond Pulses From a Quasi-CW Nd:YVO4 Grazing-Incidence Two-Stage Slab Amplifier Package," IEEE J. Quantum-Electron. **44** (2008).

72. A. Agnesi, P. Dallocchio, F. Pirzio, and G. Reali, "Sub-nanosecond single-frequency 10-kHz diode-pumped MOPA laser," Appl. Phys. B **98** (2010).

73. D. Mueller, A. Giesen, and H. Huegel, "Picosecond thin-disk regenerative amplifier," Proc. SPIE **5120**, 281 (2003).

74. P. Russbueldt, T. Mans, G. Rotarius, J. Weitenberg, H. D. Hoffmann, and R. Poprawe, "400 W Yb:YAG Innoslab fs-Amplifier," Opt. Express **17**, 12230-12245 (2009).

75. K.-M. Du, N. L. Wu, J. Xu, J. Giesekus, O. Loosen, and R. Proprawe, "Partially end-pumped Nd : YAG slab laser with a hybrid resonator," Opt. Lett. **23**, 370-372 (1998).

76. P. Russbueldt, T. Mans, J. Weitenberg, H. D. Hoffmann, and R. Poprawe, "Compact diode-pumped 1.1 kW Yb:YAG Innoslab femtosecond amplifier," Opt. Lett. **34**, 4169-4171 (2010).

77. M. Höfer, M. Traub, R. Kleindienst, H. Sipma, H.-D. Hoffmann, P. Wessels, and P. Burdack, "Multi ten-watt, ultra-stable, and tuneable Innoslab-based single frequency MOPA," Proc. SPIE **6451**, 64510S-64511 (2007).

78. F. Röser, T. Eidam, J. Rothhardt, O. Schmidt, D. N. Schimpf, J. Limpert, and A. Tünnermann, "Millijoule pulse energy high repetition rate femtosecond fiber chirped-pulse amplification system," Opt. Lett. **32**, 3495-3497 (2007).

79. S. Woutersen, U. Emmerichs, and H. J. Bakker, "Femtosecond mid-IR pump-probe spectroscopy of liquid water: Evidence for a two-component structure," Science **278**, 658-660 (1997).

80. A. W. Omta, M. F. Kropman, S. Woutersen, and H. J. Bakker, "Negligible Effect of Ions on the Hydrogen-Bond Structure in Liquid Water," Science **301**, 347-349 (2003).

81. M. L. Cowan, B. D. Bruner, N. Huse, J. R. Dwyer, B. Chugh, E. T. J. Nibbering, T. Elsaesser, and R. J. D. Miller, "Ultrafast memory loss and energy redistribution in the hydrogen bond network of liquid H2O," Nature **434**, 199-202 (2005).

82. J. Tate, T. Auguste, H. G. Muller, P. Salières, P. Agostini, and L. F. DiMauro, "Scaling of Wave-Packet Dynamics in an Intense Midinfrared Field," Phys. Rev. Lett. **98**, 013901 (2007).

83. F. Adler, K. Moutzouris, A. Leitenstorfer, H. Schnatz, B. Lipphardt, G. Grosche, and F. Tauser, "Phase-locked two-branch erbium-doped fiber laser system for long-term precision measurements of optical frequencies," Opt. Express **12**, 5872-5880 (2004).

84. S. V. Marchese, C. R. E. Baer, A. G. Engqvist, S. Hashimoto, D. J. H. C. Maas, M. Golling, T. Südmeyer, and U. Keller, "Femtosecond thin disk laser oscillator with pulse energy beyond the 10-microjoule level," Opt. Express **16**, 6397-6407 (2008).

85. J. Neuhaus, D. Bauer, J. Zhang, A. Killi, J. Kleinbauer, M. Kumkar, S. Weiler, M. Guina, D. H. Sutter, and T. Dekorsy, "Subpicosecond thin-disk laser oscillator with pulse energies of up to 25.9 microjoules by use of an active multipass geometry," Opt. Express **16**, 20530-20539 (2008).

86. G. Arisholm, "General analysis of group velocity effects in collinear optical parametric amplifiers and generators," Opt. Exp. **15**, 6513-6527 (2007).

87. V. G. Dmitriev, G. G. Gurzadyan, and D. N. Nikogosyan, *Handbook of Nonlinear Optical Crystals* (Springer, 1997).

88. L. E. Myers, R. C. Eckardt, M. M. Fejer, R. L. Byer, and W. R. Bosenberg, "Multigrating quasi-phase-matched optical parametric oscillator in periodically poled LiNbO 3," Opt. Lett. **21**, 591-593 (1996).

89. G. Cerullo, and S. D. Silvestri, "Ultrafast optical parametric amplifiers," Reviews of Scientific Instruments **74**, 1-17 (2003).

90. Y. Furukawa, K. Kitamura, S. Takekawa, K. Niwa, and H. Hatano, "Stoichiometric Mg:LiNbO$_3$ as an effective material for nonlinear optics," Opt. Lett. **23**, 1892-1894 (1998).

91. Y. Furukawa, K. Kitamura, A. Alexandrovski, R. K. Route, M. M. Fejer, and G. Foulon, "Green-induced infrared absorption in MgO doped LiNbO$_3$," Appl. Phys. Lett. **78**, 1970-1972 (2001).

92. U. Siegner, and U. Keller, "Nonlinear optical processes for ultrashort pulse generation," in *Handbook of Optics, Vol. III*, M. Bass, E. W. Stryland, D. R. Williams, and W. L. Wolfe, eds. (McGRAW-HILL, INC., New York, 2000).

93. G. M. Gale, F. Hache, and M. Cavallari, "Broad-bandwidth parametric amplification in the visible: femtosecond experiments and simulations," IEEE J. of Sel. Topics in Quantum Electronics **4**, 224-229 (1998).

94. T. Skauli, P. S. Kuo, K. L. Vodopyanov, T. J. Pinguet, O. Levi, L. A. Eyres, J. S. Harris, M. M. Fejer, B. Gerard, L. Becouarn, and E. Lallier, "Improved dispersion relations for GaAs and applications to nonlinear optics," Journal of Applied Physics **94**, 6447-6455 (2003).

95. G. Arisholm, "General numerical methods for simulating second-order nonlinear interactions in birefringent media," J. Opt. Soc. Am. B **14**, 2543-2549 (1997).

96. C. P. Hauri, P. Schlup, G. Arisholm, J. Biegert, and U. Keller, "Phase-preserving chirped-pulse optical parametric amplification to 17.3 fs directly from a Ti:sapphire oscillator," Opt. Lett. **29**, 1369-1371 (2004).

97. M. J. W. Rodwell, D. M. Bloom, and K. J. Weingarten, "Subpicosecond laser timing stabilization," IEEE J. Quantum Electron. **25**, 817-827 (1989).

98. N. Ishii, C. Y. Teisset, T. Fuji, S. Kohler, K. Schmid, L. Veisz, A. Baltuska, and F. Krausz, "Seeding of an eleven femtosecond optical parametric chirped pulse amplifier and its Nd/sup 3+/ picosecond pump laser from a single broadband Ti:Sapphire oscillator," IEEE J. Sel. Top. Quantum Electron. **12**, 173-180 (2006).

99. H. R. Telle, G. Steinmeyer, A. E. Dunlop, J. Stenger, D. H. Sutter, and U. Keller, "Carrier-envelope offset phase control: A novel concept for absolute optical frequency measurement and ultrashort pulse generation," Appl. Phys. B **69**, 327-332 (1999).

100. I. N. Ross, P. Matousek, G. H. C. New, and K. Osvay, "Analysis and optimization of optical parametric chirped pulse amplification," J. Opt. Soc. Am. B **19**, 2945-2956 (2002).

101. A. Baltuska, T. Fuji, and T. Kobayashi, "Controlling the carrier-envelope phase of ultrashort light pulses with optical parametric amplifiers," Phys. Rev. Lett. **88**, 133901 (2002).

102. Y. Deng, F. Lu, and W. H. Knox, "Fiber-laser-based difference frequency generation scheme for carrier-envelope-offset phase stabilization applications," Opt. Express **13**, 4589 (2005).

103. B. Proctor, and F. Wise, "Quartz prism sequence for reduction of cubic phase in a modelocked Ti:sapphire laser," Opt. Lett. **17**, 1295-1297 (1992).

104. F. J. Duarte, "Generalized multiple-prism dispersion theory for pulse compression in ultrafast dye lasers," Opt. Quantum Electron. **19**, 223-229 (1987).

105. R. L. Fork, O. E. Martinez, and J. P. Gordon, "Negative dispersion using pairs of prisms," Opt. Lett. **9**, 150-152 (1984).

106. R. Trebino, and D. J. Kane, "Using phase retrieval to measure the intensity and phase of ultrashort pulses: frequency-resolved optical gating," J. Opt. Soc. Am. A **10**, 1101-1111 (1993).

107. T. Suhara, and H. Nishihara, "Theoretical analysis of waveguide second-harmonic generation phase matched with uniform and chirped gratings," IEEE J. Quantum Electron. **26**, 1265-1276 (1990).

108. M. A. Arbore, O. Marco, and M. M. Fejer, "Pulse compression during second-harmonic generation in aperiodic quasi-phase-matching gratings," Opt. Lett. **22**, 865-867 (1997).

109. G. Imeshev, A. Galvanauskas, D. Harter, M. A. Arbore, M. Proctor, and M. M. Fejer, "Engineerable femtosecond pulse shaping using second harmonic generation with Fourier synthetic quasi-phasematching gratings," Opt. Lett. **23**, 864-866 (1998).

110. L. Gallmann, G. Steinmeyer, G. Imeshev, J.-P. Meyn, M. M. Fejer, and U. Keller, "Sub-6-fs blue pulses generated by quasi-phase-matching second-harmonic generation pulse compression," Appl. Phys. B **74**, S237-S243 (2002).

111. L. Gallmann, G. Steinmeyer, U. Keller, G. Imeshev, M. M. Fejer, and J.-P. Meyn, "Generation of sub-6-fs blue pulses by frequency doubling with quasi-phase-matching gratings," Opt. Lett. **26**, 614-616 (2001).

112. D. Artigas, D. T. Reid, M. M. Fejer, and L. Torner, "Pulse compression and gain enhancement in a degenerate optical parametric amplifier based on aperiodically poled crystals," Opt. Lett. **27**, 442-444 (2002).

113. D. Artigas, and D. T. Reid, "Efficient femtosecond optical parametric oscillators based on aperiodically poled nonlinear crystals," Opt. Lett. **27**, 851-853 (2002).

114. M. Charbonneau-Lefort, M. M. Fejer, and B. Afeyan, "Tandem chirped quasi-phase-matching grating optical parametric amplifier design for simultaneous group delay and gain control," Optics Letters **30**, 634-636 (2005).

115. A. M. Weiner, "Femtosecond pulse shaping using spatial light modulators," Rev. Sci. Instrum. **71**, 1929-1960 (2000).

116. C. Langrock, M. M. Fejer, I. Hartl, and M. E. Fermann, "Generation of octave-spanning spectra inside reverse-proton-exchanged periodically poled lithium niobate waveguides," Opt. Lett. **32**, 2478-2480 (2007).

117. R. K. Shelton, L.-S. Ma, H. C. Kapteyn, M. M. Murnane, J. L. Hall, and J. Ye, "Phase-coherent optical pulse synthesis from separate femtosecond lasers," Science **293**, 1296-1289 (2001).

118. C. Conti, S. Trillo, P. Di Trapani, J. Kilius, A. Bramati, S. Minardi, W. Chinaglia, and G. Valiulis, "Effective lensing effects in parametric frequency conversion," J. Opt Soc. Am. B **19** (2002).

119. S. Mukamel, Y. Tanimura, and P. Hamm, "Multidimensional Coherent Spectroscopy," Acc. Chem. Res. **42**, 1207-1209 (2009).

120. P. Hamm, Private communication (2011).

121. A. T. J. B. Eppink, and D. H. Parker, "Velocity map imaging of ions and electrons using electrostatic lenses: Application in photoelectron and photofragment ion imaging of molecular oxygen," Rev. Sci. Instrum. **68**, 3477 (1997).

122. B. Walker, B. Sheehy, L. F. DiMauro, P. Agostini, K. J. Schafer, and K. C. Kulander, "Precision Measurement of Strong Field Double Ionization of Helium," Phys. Rev. Lett. **73**, 1227 (1994).

123. L. Arissian, C. Smeenk, F. Turner, C. Trallero, A. V. Sokolov, D. M. Villeneuve, A. Staudte, and P. B. Corkum, "Direct Test of Laser Tunneling with Electron Momentum Imaging," Phys. Rev. Lett. **105** (2010).

124. H. R. Reiss, "Novel Phenomena in Very-Low-Frequency Strong Fields," Phys. Rev. Lett. **102**, 143003 (2009).

125. P. M. Paul, E. S. Toma, P. Breger, G. Mullot, F. Augé, P. Balcou, H. G. Muller, and P. Agostini, "Observation of a Train of Attosecond Pulses from High Harmonic Generation," Science **292**, 1689-1692 (2001).

126. M. Hentschel, R. Kienberger, C. Spielmann, G. A. Reider, N. Milosevic, T. Brabec, P. Corkum, U. Heinzmann, M. Drescher, and F. Krausz, "Attosecond metrology," Nature **414**, 509-513 (2001).

127. G. Sansone, E. Benedetti, F. Calegari, C. Vozzi, L. Avaldi, R. Flammini, L. Poletto, P. Villoresi, C. Altucci, R. Velotta, S. Stagira, S. De Silvestri, and M. Nisoli, "Isolated single-cycle attosecond pulses," Science **314**, 443-446 (2006).

128. M. J. Abel, T. Pfeifer, P. M. Nagel, W. Boutu, M. J. Bell, C. P. Steiner, D. M. Neumark, and S. R. Leone, "Isolated attosecond pulses from ionization gating of high-harmonic emission," Chem. Phys. **366**, 9-14 (2009).

129. I. Thomann, A. Bahabad, X. Liu, R. Trebino, M. M. Murnane, and H. C. Kapteyn, "Characterizing isolated attosecond pulses from hollow-core waveguides using multi-cycle driving pulses," Opt. Express **17**, 4611-4633 (2009).

130. S. Gilbertson, S. D. Khan, Y. Wu, M. Chini, and Z. Chang, "Isolated Attosecond Pulse Generation without the Need to Stabilize the Carrier-Envelope Phase of Driving Lasers," Phys. Rev. Lett. **105**, 093902 (2010).

131. M. B. Gaarde, J. L. Tate, and K. J. Schafer, "Macroscopic aspects of attosecond pulse generation," J. Phys. B: At. Mol. Opt. Phys. **41**, 132001 (2008).

132. P. Salières, A. L'Huillier, and M. Lewenstein, "Coherence Control of High-Order Harmonics," Phys. Rev. Lett. **74**, 3776-3779 (1995).

133. P. Balcou, P. Salières, A. L'Huillier, and M. Lewenstein, "Generalized phase-matching conditions for high harmonics: The role of field-gradient forces," Phys. Rev. A **55**, 3204-3210 (1997).

134. P. Balcou, A. S. Dederichs, M. B. Gaarde, and A. L'Huillier, "Quantum-path analysis and phase matching of high-order harmonic generation and high-order frequency mixing processes in strong laser fields," J. Phys. B: At. Mol. Opt. Phys. **32**, 2973-2989 (1999).

135. A. Zaïr, M. Holler, A. Guandalini, F. Schapper, J. Biegert, L. Gallmann, U. Keller, A. S. Wyatt, A. Monmayrant, I. A. Walmsley, E. Cormier, T. Auguste, J. P. Caumes, and P. Salières, "Quantum Path Interferences in High-order Harmonic Generation," Phys. Rev. Lett. **100**, 143902 (2008).

136. M. Holler, A. Zaïr, F. Schapper, T. Auguste, E. Cormier, A. Wyatt, A. Monmayrant, I. A. Walmsley, L. Gallmann, P. Salières, and U. Keller, "Ionization effects on spectral signatures of quantum-path interferences in high-harmonic generation," Opt. Express **17**, 5716-5722 (2009).

137. T. Auguste, P. Salières, A. S. Wyatt, A. Monmayrant, I. A. Walmsley, E. Cormier, A. Zaïr, M. Holler, A. Guandalini, F. Schapper, J. Biegert, L. Gallmann, and U. Keller, "Theoretical and experimental analysis of quantum path interferences in high-order harmonic generation," Phys. Rev. A **80**, 033817 (2009).

138. F. Schapper, M. Holler, T. Auguste, A. Zair, M. Weger, J. P. Caumes, P. Salieres, L. Gallmann, and U. Keller, "Spatial fingerprint of quantum path interferences in high order harmonic generation," Optics Express **18**, 2987-2994 (2010).

139. P. Agostini, and L. F. DiMauro, "The physics of attosecond light pulses," Rep. Prog. Phys. **67**, 813-855 (2004).

140. Y. Mairesse, A. de Bohan, L. J. Frasinski, H. Merdji, L. C. Dinu, P. Monchicourt, P. Breger, M. Kovačev, R. Taïeb, B. Carré, H. G. Muller, P. Agostini, and P. Salières, "Attosecond Synchronization of High-Harmonic Soft X-rays," Science **302**, 1540-1543 (2003).

141. K. J. Schafer, B. Yang, L. F. DiMauro, and K. C. Kulander, "Above threshold ionization beyond the high harmonic cutoff," Phys. Rev. Lett. **70**, 1599-1602 (1993).

142. M. Lewenstein, P. Balcou, M. Y. Ivanov, A. L'Huillier, and P. B. Corkum, "Theory of high-harmonic generation by low-frequency laser fields," Phys. Rev. A **49**, 2117-2132 (1994).

143. M. Lewenstein, P. Salières, and A. L'Huillier, "Phase of the atomic polarization in high-order harmonic generation," Phys. Rev. A **52**, 4747-4754 (1995).

144. J. J. Macklin, J. D. Kmetec, and C. L. G. III, "High-Order Harmonic generation Using Intense Femtosecond Pulses," Phys. Rev. Lett. **70**, 766-769 (1993).

145. C.-G. Wahlström, J. Larsson, A. Persson, T. Starczewski, S. Svanberg, P. Salières, P. Balcou, and A. L'Huillier, "High-order harmonic generation in rare gases with an intense short-pulse laser," Phys. Rev. A **48**, 4709-4720 (1993).

146. J. Mauritsson, P. Johnsson, R. Lopez-Martens, K. Varju, W. Kornelis, J. Biegert, U. Keller, M. B. Gaarde, K. J. Schafer, and A. L.'Huillier, "Measurement and control of the frequency chirp rate of high-order harmonic pulses," Phys. Rev. A **70**, 021801(R) (2004).

147. G. Sansone, E. Benedetti, J.-P. Caumes, S. Stagira, C. Vozzi, S. De Silvestri, and M. Nisoli, "Control of long electron quantum paths in high-order harmonic generation by phase-stabilized light pulses," Phys. Rev. A **73**, 053408 (2006).

148. E. Benedetti, J.-P. Caumes, G. Sansone, S. Stagira, C. Vozzi, and M. Nisoli, "Frequency chirp of long electron quantum paths in high-order harmonic generation," Opt. Express **14**, 2242-2249 (2006).

149. H. Merdji, M. Kovacev, W. Boutu, P. Salières, F. Vernay, and B. Carré, "Macroscopic control of high-order harmonics quantum-path components for the generation of attosecond pulses," Phys. Rev. A **74**, 043804 (2006).

150. Z. Chang, A. Rundquist, H. Wang, I. Christov, H. C. Kapteyn, and M. M. Murnane, "Temporal phase control of soft-x-ray harmonic emission," Phys. Rev. A **58**, R30-R33 (1998).

151. M. B. Gaarde, F. Salin, E. Constant, P. Balcou, K. J. Schafer, K. C. Kulander, and A. L'Huillier, "Spatiotemporal separation of high harmonic radiation into two quantum path components," Phys. Rev. A **59**, 1367-1373 (1999).

152. P. Salières, A. L'Huillier, P. Antoine, and M. Lewenstein, "Study of the Spatial and Temporal Coherence of High-Order Harmonics," Adv. At. Mol. Opt. Phys. **41**, 83-142 (1999).

153. E. Cormier, and P. Lambropoulos, "Effect of the initial phase of the field in ionization by ultrashort laser pulses," Eur. Phys. J. D **2**, 15-20 (1998).

154. C. Lynga, M. B. Gaarde, C. Delfin, M. Bellini, T. W. Hänsch, A. L'Huillier, and C.-G. Wahlström, "Temporal coherence of high-order harmonics," Phys. Rev. A **60**, 4823-4830 (1999).

155. D. J. Jones, S. A. Diddams, J. K. Ranka, A. Stentz, R. S. Windeler, J. L. Hall, and S. T. Cundiff, "Carrier-envelope phase control of femtosecond mode-locked lasers and direct optical frequency synthesis," Science **288**, 635-639 (2000).

156. A. Apolonski, A. Poppe, G. Tempea, C. Spielmann, T. Udem, R. Holzwarth, T. W. Hänsch, and F. Krausz, "Controlling the Phase Evolution of Few-Cycle Light Pulses," Phys. Rev. Lett. **85**, 740-743 (2000).

157. M. B. Gaarde, and K. J. Schafer, "Quantum path distributions for high-order harmonics in rare gas atoms," Phys. Rev. A **65**, 031406(R) (2006).

158. W. Boutu, S. Haessler, H. Merdji, P. Breger, G. Waters, M. Stankiewicz, L. J. Frasinski, R. Taieb, J. Caillat, A. Maquet, P. Monchicourt, B. Carre, and P. Salières, "Coherent control of attosecond emission from aligned molecules," Nature Physics **4**, 545-549 (2008).

159. A. Zaïr, A. Guandalini, F. Schapper, M. Holler, J. Biegert, L. Gallmann, A. Couairon, M. Franco, A. Mysyrowicz, and U. Keller, "Spatio-temporal characterization of few-cycle pulses obtained by filamentation," Opt. Express **15**, 5394-5404 (2007).

160. M. Bellini, C. Lynga, A. Tozzi, M. B. Gaarde, T. W. Hänsch, A. L'Huillier, and C. G. Wahlström, "Temporal coherence of ultrashort high-order harmonic pulses," Phys. Rev. Lett. **81**, 297 (1998).

161. C. Corsi, A. Pirri, E. Sali, A. Tortora, and M. Bellini, "Direct interferometric measurement of the atomic dipole phase in high-order harmonic generation," Phys. Rev. Lett. **97**, 023901 (2006).

162. C. M. Heyl, J. Güdde, U. Höfer, and A. L'Huillier, "Spectrally-resolved Maker fringes in high-order harmonic generation," unpublished (2011).

163. P. D. Maker, R. W. Terhune, M. Nisenoff, and C. M. Savage, "Effects of dispersion and focusing on the production of optical harmonics," Phys. Rev. Lett. **8**, 21-23 (1962).

164. H. G. Muller, "Reconstruction of attosecond harmonic beating by interference of two-photon transitions," Appl. Phys. B **74**, S17-S21 (2002).

165. R. Lopez-Martens, K. Varju, P. Johnsson, J. Mauritsson, Y. Mairesse, P. Salieres, M. B. Gaarde, K. J. Schafer, A. Persson, S. Svanberg, C.-G. Wahlstrom, and A. L'Huillier, "Amplitude and Phase Control of Attosecond Light Pulses," Phys. Rev. Lett. **94**, 033001 (2005).

166. P. Johnsson, J. Mauritsson, T. Remetter, A. L'Huillier, and K. J. Schafer, "Attosecond Control of Ionization by Wave-Packet Interference," Phys. Rev. Lett. **99**, 233001 (2007).

167. Z.-H. Loh, M. Khalil, R. E. Correa, R. Santra, C. Buth, and S. R. Leone, "Quantum State-Resolved Probing of Strong-Field-Ionized Xenon Atoms Using Femtosecond High-Order Harmonic Transient Absorption Spectroscopy," Phys. Rev. Lett. **98**, 143601 (2007).

168. P. Rivière, O. Uhden, U. Saalmann, and J. M. Rost, "Strong field dynamics with ultrashort electron wave packet replicas," New J. Phys. **11**, 053011 (2009).

169. X. M. Tong, P. Ranitovic, C. L. Cocke, and N. Toshima, "Mechanisms of infrared-laser-assisted atomic ionization by attosecond pules," Phys. Rev. A **81**, 021404 (2010).

170. C. Vozzi, F. Calegari, F. Frassetto, L. Poletto, G. Sansone, P. Villoresi, M. Nisoli, S. D. Silvestri, and S. Stagira, "Coherent continuum generation above 100 eV driven by an ir parametric source in a two-color scheme," Phys. Rev. A **79**, 033842 (2009).

171. G. Doumy, J. Wheeler, C. Roedig, R. Chirla, P. Agostini, and L. F. DiMauro, "Attosecond Synchronization of High-Order Harmonics from Midinfrared Drivers," Phys. Rev. Lett. **102**, 093002 (2009).

172. A. D. Shiner, C. Trallero-Herrero, N. Kajumba, H.-C. Bandulet, D. Comtois, F. Légaré, M. Giguère, J.-C. Kieffer, P. B. Corkum, and D. M. Villeneuve, "Wavelength Scaling of High Harmonic Generation Efficiency," Phys. Rev. Lett. **103**, 073902 (2009).

173. W. Quan, Z. Lin, M. Wu, H. Kang, H. Liu, X. Liu, J. Chen, J. Liu, X. T. He, S. G. Chen, H. Xiong, L. Guo, H. Xu, Y. Fu, Y. Cheng, and Z. Z. Xu, "Classical Aspects in Above-Threshold Ionization with a Midinfrared Strong Laser Field," Phys. Rev. Lett. **103** (2009).

174. C. Vozzi, F. Calegari, E. Benedetti, S. Gasilov, G. Sansone, G. Cerullo, M. Nisoli, S. De Silvestri, and S. Stagira, "Millijoule-level phase-stabilized few-optical-cycle infrared parametric source," Opt. Lett. **32**, 2957-2959 (2007).

175. C. Vozzi, C. Manzoni, F. Calegari, E. Benedetti, G. Sansone, G. Cerullo, M. Nisoli, S. De Silvestri, and S. Stagira, "Characterization of a high-energy self-phasestabilized near-infrared parametric source," J. Opt. Soc. Am. B **25**, B112-B117 (2008).

176. D. Brida, M. Marangoni, C. Manzoni, S. De Silvestri, and G. Cerullo, "Two-optical-cycle pulses in the mid-infrared from an optical parametric amplifier," Opt Lett **33**, 2901-2903 (2008).

177. R. Santra, V. S. Yakovlev, T. Pfeifer, and Z.-H. Loh, "Theory of attosecond transient absorption spectroscopy of strong-field-generated ions," Phys. Rev. A **83**, 033405 (2011).

Acknowledgments

There are a number of dedicated people behind the results presented in the above Chapters. Some have contributed directly by patiently spending many hours in the laboratory or by interpreting the data. Others, equally important, have contributed indirectly by creating an environment that made this work possible or by having an open ear for discussion. Many people contributed in one way or another. Here, I would like to thank all of them and sincerely hope that I left none of them unmentioned.

First, I would like to thank Prof. Dr. Ursula Keller for believing in me and offering me this position. You gave me considerable scientific freedom and I never had to worry too much about funding and resources.

I'm also deeply indebted to the graduate students and postdocs in the attosecond and high-field part of the group for their patience and persistence in the laboratory that made this work possible. The mid-infrared OPCPA one-man business was first successfully run by Christian Erny and then Clemens Heese. The quantum path interferences in HHG were discovered and investigated by Dr. Amelle Zaïr, Mirko Holler, and Florian Schapper. The latter two were also the driving forces behind the attosecond beamline and the transient absorption measurements. With the velocity-map imaging spectrometer of Matthias Weger we will hopefully soon perform our first high-field experiments using our OPCPA source. I would like to thank Dr. Thomas Remetter for initiating our WPRC tradition and all the younger students who bravely took over some of the projects and who are in the process of exploring new realms in attosecond science: Reto Locher, Jens Herrmann, and Mazyar Sabbar. I also enjoyed interacting with the attoclock team: Dr. Claudio Cirelli, Dr. Mathias Smolarski, Adrian Pfeiffer, Petrissa Eckle, and Robert Boge.

Of course, I also would like to thank all the other present and former members of the Ultrafast Laser Physics group. I had pleasant conversations with many of you. Keep up the good group spirit!

It was a pleasure to work with Sandra Schmid who provides always friendly and efficient administrative support. I want to express my appreciation towards all the ETH staff providing various essential services that facilitate our lives every day. In particular, I'd like to thank the people from the department's mechanical engineering office and the physics machine shop for their indispensable contributions.

I enjoyed collaborating with many people of our scientific community throughout the last years. I'm grateful for your essential contributions to this work. Thank you to all our present and past collaborators from Stanford, Saclay, Lund, Bordeaux, Oxford, and Dresden.

I would like to thank my wife Birgit for her love and for supporting (and enduring?) my career with all its side-effects on private life since a decade now! My final thank-you goes to her and our children Mark and Lara for brightening up my after-work life.

Zürich, April 2011

L. Gallman